

Copyright  
by  
Gregory Thomas Jackson  
2010

The Thesis committee for Gregory Thomas Jackson  
Certifies that this is the approved version of the following  
thesis:

**CFD- Based Representation Of Non-Newtonian Polymer Injectivity For  
A Horizontal Well With Coupled Formation-Wellbore Hydraulics**

**Approved by**

**Supervising Committee:**

---

**Matthew Balhoff, Supervisor**

---

**Chun Huh**

**CFD-Based Representation Of Non-Newtonian Polymer Injectivity For  
A Horizontal Well With Coupled Formation-Wellbore Hydraulics**

**by**

**Gregory Thomas Jackson, B.S.M.E.**

**Thesis**

Presented to the Faculty of the Graduate School of

The University of Texas at Austin

in Partial Fulfillment

of the Requirements

for the Degree of

**Master of Science in Engineering**

**The University of Texas at Austin**

**December 2010**

## **Dedication**

To my wife, Jenn, for enduring the hours with me

## **Acknowledgements**

To all the people who helped me, thank you. The University of Texas at Austin Department of Petroleum and Geosystems Engineering granted me the space, time, and support needed to accomplish this research. The support staff provided invaluable help and made my time in Austin some of the best of my life. Thank you to the financial donors that assisted in this research including the CEOR group, BP/Questar Fellowship, George J. Heuer Endowed Graduate Fellowship, and the Jack L. Thurber Memorial Endowed Presidential Scholarship that enabled me to focus on my research.

Dr. Matthew Balhoff, your patience, guidance, and support aided me in countless ways allowing me to complete this work. I appreciate Dr. Mojdeh Delshad's UTCHEM help, without her I would never have been able to piece my way through the code. My fellow graduate students, Ali Afsharpour, Ali Farhadinia, Yashar Mehmani, Robert Peterson, Abhinav Sharma, and Tie Sun provided numerous answers to my countless questions and I thank you for friendship. The other faculty and staff including Dr. Chun Huh, Dr. David DiCarlo, and Roger Terzian were vital as well with their open door policy and eagerness to share their wisdom.

Lastly, my wife provided me with encouragement, support, and confidence. Your belief in me helped sustain me through these two years. I never could have accomplished it without you.

## **Abstract**

# **CFD-Based Representation Of Non-Newtonian Polymer Injectivity For A Horizontal Well With Coupled Formation-Wellbore Hydraulics**

Gregory Thomas Jackson, M.S.E.

The University of Texas at Austin, 2010

Supervisor: Matthew Balhoff

During injection of a high-viscosity, non-Newtonian polymer into a long horizontal well, a significant pressure drop occurs along the well length. Computational Fluid Dynamics (CFD) modeling of the shear-thinning flow of polymer in the wellbore, coupled with the viscoelastic flow in composite gravel-pack/near-well formation zone, was carried out to develop convenient correlations for axial pressure values of both Newtonian and non-Newtonian fluids along the well length, for use in chemical EOR simulations.

The detailed CFD modeling of the non-Newtonian flow behavior of polymer within the horizontal wellbore, completion zone and the near-well formation, not only allows accurate accounting of pressure distribution along the long horizontal well, but also can be employed for screening diagnosis for possible injectivity inefficiencies resulting from non-uniform pressure values.

At both high and low injection rates, CFD modeling predicts non-uniform pressure distributions for highly viscous fluids. The inclusive pressure correlation was

implemented into UTCHEM, a University of Texas at Austin research simulator, to determine the importance of including pressure drop in polymer injections. Early times (i.e., less than 100 days) yielded a significant oil recovery deviation from a uniform pressure wellbore. However, at later times the recovery loss generated by the pressure decrease was deemed negligible; therefore, the traditional assumption regarding uniform pressure in horizontal wellbores was still reasonable for highly viscous non-Newtonian flow.

This CFD study is the first mechanistic investigation of the polymer injectivity with detailed description of the wellbore, completion zone and near-well formation, and with full accounting of the shear-thinning rheology for pipe flow and the viscoelastic rheology of polymer in porous media. With increased use of very high molecular-weight polymers for chemical EOR processes for mobility control, the latter mechanism is known to be critical.

## Table of Contents

LIST OF TABLES .....	x
LIST OF FIGURES .....	xi
Chapter 1: INTRODUCTION.....	1
1.1 Current Oilfield Assumptions.....	1
1.2 Other Scientific Applications with Permeable Walls .....	3
Chapter 2: MODEL DESCRIPTION.....	9
2.1 Reservoir Size Optimization.....	15
2.2 Mesh Optimization.....	17
2.3 COMSOL Example.....	18
Chapter 3: RESULTS AND DISCUSSION .....	20
3.1 Newtonian Examination.....	20
3.2 Shear-Thinning .....	31
3.3 Shear-Thickening.....	39
3.4 Relevant Axial Pressure Drops .....	44
3.5 Inclusive Pressure Equation (IPE).....	46
Chapter 4: IMPLEMENTATION IN UTCHEM.....	48
4.1 Implementation .....	48
4.2 Model Creation and Testing Plan .....	51
4.3 Homogeneous Reservoirs .....	53
4.4 Heterogeneous Reservoirs .....	61
Chapter 5: COMPLETIONS.....	67
5.1 Gravel Packs .....	67
5.2 Perforations.....	72
Chapter 6: CONCLUSIONS AND RECOMMENDATIONS .....	76
Recommendations and Future Work .....	77



Appendix A: MODEL BUILDING INSTRUCTIONS .....	79
Appendix B: NEWTONIAN CASES .....	94
Appendix C: NON-NEWTONIAN CASES .....	103
C.1 Shear-thinning .....	103
C.2 Shear-thickening.....	107
Appendix D: UTCHEM.....	109
D.1 Analysis.....	109
D.2 Code .....	113
Appendix E: COMPLETIONS .....	117
E.1 Gravel packs .....	117
E.2 Perforations.....	119
NOMENCLATURE/ABBREVIATIONS .....	123
REFERENCES .....	129
VITA.....	135

## LIST OF TABLES

Table 2.1:	Well and reservoir properties used to determine reservoir size optimization. .....	15
Table 3.1:	Model properties used in the examination for the Newtonian fluid of Marshall and Trowbridge (1974). .....	20
Table 3.2:	Shear-thinning and shear-thickening properties of the 3000 ppm HPAM depicted in Figure 1 of Lee et al. (2009). .....	34
Table 4.1:	Reservoir, well, and grid properties for the UTCHEM model illustrated in Figure 4.1. .....	52
Table 4.2:	List of the percent recovery loss in oil recovery at 10 days, 100 days, and 1000 days for the nine homogeneous tests given in Table D.1. .....	59
Table B.1:	List of 48 full-length wells and the corresponding total axial pressure drop to determine the limitations of Marshall and Trowbridge (1974). .....	95
Table C.1:	Shear-thinning and shear-thickening test plan to determine the accuracy of the apparent viscosity evaluation at $r = R_w$ . .....	103
Table D.1:	List of the 14 tests conducted to determine the importance of pressure drop in polymer injections. .....	110
Table E.1:	List of well and reservoir properties are given below. .....	117

## LIST OF FIGURES

Figure 2.1:	A horizontal well with the green lines representing the segment that is being modeled (Signal Oil and Gas).....	10
Figure 2.2:	COMSOL model with the corresponding physics and boundary conditions. ....	11
Figure 2.3:	An open-ended toe with spherical flow (top) versus a closed toe with radial flow the entire length of the well (bottom). ....	13
Figure 2.4:	Reservoir thickness optimization to account for viscosity variation. ....	16
Figure 2.5:	Radial velocity convergence as a function of mesh refinement. ....	17
Figure 3.1:	Marshall and Trowbridge solution, M-T, and the COMSOL solution showing near perfect agreement along the well.....	21
Figure 3.2:	Area difference between one and the ratio of the COMSOL solution and Marshall and Trowbridge (1974).....	23
Figure 3.3:	Area difference convergence for a high leakage rate (16.67 STB/D/m) and a low leakage rate (1.3 STB/D/m). ....	24
Figure 3.4:	A schematic depicting $P_{o\_seg}$ and $p_{T\_seg}$ for a given well segment. ....	25
Figure 3.5:	Marshall and Trowbridge solution using a different $C_L$ value for each well segment, New $C_L$ , and the original Marshall and Trowbridge solution, M-T, compared to the COMSOL solution along the well.....	27
Figure 3.6:	Pressure values for modified Marshall and Trowbridge (New $C_L$ ) and original Marshall and Trowbridge (M-T), compared to COMSOL, for an entire well.....	28
Figure 3.7:	Marshall and Trowbridge solution using a different $C_L$ value for each well segment, New $C_L$ , compared to the COMSOL solution at the heel of the well for four different leakage rates.....	29
Figure 3.8:	Pressure values modified Marshall and Trowbridge (New $C_L$ ) and original Marshall and Trowbridge (M-T) COMSOL compared to Hagen-Poiseuille (Hagen) for an entire well. ....	30
Figure 3.9:	Carreau model for the HPAM that was discussed in Delshad et al. (2008). ....	32

Figure 3.10: Rheological data for the 3000 ppm polymer from Figure 1 of Lee et al. (2009).	35
Figure 3.11: Pressure matches using different apparent viscosity concepts for Test 4 in Table C.1 without the modified $\gamma^*$ .	37
Figure 3.12: Pressure matches using different apparent viscosity concepts for Test 4 in Table C.1 with the modified $\gamma^*$ .	37
Figure 3.13: Axial well pressure comparison of COMSOL to Equation 1.4 (Equation 3.11 being used to calculate $\gamma^*_{\text{new}}$ and $C_{L\_new}$ ) for both the Newtonian and shear-thinning fluids with for the well-reservoir domains listed in Table 3.1.	38
Figure 3.14: Pressure matches using different apparent viscosity concepts of viscoelastic fluids for Test 4 in Table C.1 without the modified $\gamma^*$ .	40
Figure 3.15: Pressure matches using different apparent viscosity concepts of viscoelastic fluids for Test 4 in Table C.1 with the modified $\gamma^*$ .	40
Figure 3.16: Pressure matches using $\gamma^*_{\text{new}}$ when the apparent reservoir viscosity greatly exceeds the apparent well viscosity.	41
Figure 3.17: Axial well pressure using COMSOL for both the viscoelastic (UVM) and shear-thinning (Carreau) fluids compared to the Newtonian case for the well-reservoir domains listed in Table 3.1 and Table 3.2.	42
Figure 3.18: Leakage rates for both the viscoelastic (UVM) and shear-thinning (Carreau) fluids for the well-reservoir domains listed in Table 3.1 and Table 3.2.	43
Figure 3.19: Pressure drop correlation for 10 cp, 100 cp, 200 cp, and 300 cp Newtonian fluids in a 600 meter well as a function of injection rate.	45
Figure 3.20: Pressure drop correlation for 10 cp, 100 cp, 200 cp, and 300 cp Newtonian fluids in a 1,800 meter well as a function of injection rate.	46
Figure 4.1: Physical dimensions and orientation of the UTCHEM model for implementation of the IPE.	52
Figure 4.2: Injection discrepancies at 0.5 days between the IPE and a constant pressure assumption for Test 5 from Table D.1.	53
Figure 4.3: Injection discrepancies at 50 days between the IPE and a constant pressure assumption for Test 5 from Table D.1.	54

Figure 4.4:	Water saturation profiles of Test 5 in Table D.1 for the IPE (top) and the constant pressure assumption (bottom) at 1000 days. ....	55
Figure 4.6:	Cumulative lost recovery as a function of time for Test 5 of Table D.1. ....	56
Figure 4.7:	Percent recovery loss in recovery using Equation 4.4 as a function of time for Test 5 of Table D.1.....	56
Figure 4.5:	Axial well pressure profiles for Test 5 of Table D.1. ....	57
Figure 4.8:	Axial well pressure loss comparison as a function of time for Test 3 and Test 5 of Table D.1. ....	60
Figure 4.9:	Bar graph of percent loss in recovery using Equation 4.4 comparing 1 D tests to 500 md tests. ....	61
Figure 4.10:	Axial pressure profile comparison for Tests 5 and 14. ....	62
Figure 4.11:	Early time axial pressure profiles for Test 14 of Table D.1.....	63
Figure 4.12:	Late time axial pressure profiles for Test 14 of Table D.1. ....	64
Figure 4.13:	Bar graph comparing the percent loss of the homogeneous and heterogeneous cases at 10 days.....	65
Figure 4.14:	Bar graph comparing the percent loss of Tests 5 and 14 at 10 days, 100 days, and 1000 days. ....	66
Figure 5.1:	COMSOL model with the corresponding physics and boundary conditions including the gravel pack subdomain (radial dimensions of the well and gravel pack are highly exaggerated in the schematic).....	68
Figure 5.2:	Non-dimensional axial pressure comparison between Newtonian, shear-thinning, and viscoelastic fluids with a gravel pack for $Q_y/Q_z = 0.01$ . ....	69
Figure 5.3:	Shear-thinning and viscoelastic non-dimensional axial pressure drop with viscosities evaluated at $r = R_w$ and $r = R_{GP}$ for $Q_y/Q_z = 0.01$ .....	70
Figure 5.4:	Axial pressure drop for a Newtonian fluid both with and without a gravel pack for $Q_y/Q_z = 0.1$ .....	71
Figure 5.5:	COMSOL model with the corresponding physics and boundary conditions for a perforated well.....	73

Figure 5.6: Shear-thinning and viscoelastic non-dimensional axial pressure drop with viscosities evaluated at perforation-reservoir interface for $Q_y/Q_z = 0.01$ ....	74
Figure B.1: Marshall and Trowbridge (1974) equation, M-T, compared to the COMSOL solution along the well for 600 meter case. ....	96
Figure B.2: Marshall and Trowbridge (1974) equation, M-T, compared to the COMSOL solution along the well for 1800 meter case. ....	97
Figure B.3: Marshall and Trowbridge (1974) equation, M-T, compared to the COMSOL solution along the well for 3000 meter case. ....	98
Figure B.4: Area difference between the 2 <sup>nd</sup> order polynomial and unity converging to zero as a function of well length. ....	99
Figure B.5: Coefficient of 2 <sup>nd</sup> order term, A, as a function of $Q_y/Q_z$ . ....	100
Figure B.6: Coefficient of 2 <sup>nd</sup> order term, A, as a function of Reynolds Number. ....	101
Figure B.7: Coefficient of 1 <sup>st</sup> order term, B, as a function of Reynolds Number. ....	102
Figure C.1: Test 3 from Table C.1 using the IPE including the viscosity ratio in the conductivity ratio, Equation 3.6, evaluated at $r = R_w$ for a shear-thinning fluid. ....	104
Figure C.2: Test 4 from Table C.1 using the IPE including the viscosity ratio in the conductivity ratio, Equation 3.6, evaluated at $r = R_w$ for a shear-thinning fluid. ....	105
Figure C.3: Test 6 from Table C.1 using the IPE including the viscosity ratio in the conductivity ratio, Equation 3.6, evaluated at $r = R_w$ for a shear-thinning fluid. ....	106
Figure C.4: Full length, 1500 meter well, with the reservoir properties listed in Table 3.1 and shear-thinning properties listed in Table 3.2. ....	107
Figure C.5: Test 4 from Table C.1 using the IPE including the viscosity ratio in the conductivity ratio, Equation 3.6, evaluated at $r = R_w$ for a shear-thickening fluid. ....	108
Figure D.1: Probability distribution for permeability in the reservoir blocks for the heterogeneous tests listed in Table D.1. ....	109

Figure D.2: Recovery loss of the 100 psi production wells plotted as a function of $\gamma^*_{new}$ .	111
Figure D.3: Percent loss of Test 14.	112
Figure D.4: The early time cumulative recovery profile of Test 14 comparing the IPE to a constant pressure horizontal well.	112
Figure E.1: Newtonian, shear-thinning, and shear-thickening non-dimensional axial pressure for a model including a gravel pack.	118
Figure E.2: Shear-thinning and shear-thickening non-dimensional axial pressure match using the IPE for a model including a gravel pack.	119
Figure E.3: COMSOL pressure solution for a shear-thinning fluid in 10 meters of perforations spaced 2 per meter.	120
Figure E.4: Inertial flows in perforations illustrated by the tortuous velocity streamline.	121
Figure E.5: Inertial flow in perforations illustrated by the tortuous velocity streamline.	122

## **Chapter 1: INTRODUCTION**

Horizontal wells have become increasingly popular in the oil industry, especially for thin reservoirs or reservoirs with relatively high vertical/horizontal permeability ratios (Economides et al., 1991). Horizontal wells increase the contact with the pay zone resulting in significantly higher production rates (Joshi, 1986), which is critical to the oil industry because oil discoveries have declined (Lake, 1989). Enhanced oil recovery (EOR) is an alternative to increase production without finding new reservoirs. Current world recovery is approximately 30% of the initial oil in place, while EOR can increase the recovery percentage to over 60%. EOR techniques include CO<sub>2</sub> injection, thermal processes, and polymer floods among other options (Lake, 1989). The EOR processes increasingly employ horizontal wells to improve their performance, and in these combined applications, the proper modeling representation of horizontal wells during the EOR simulations is important.

### **1.1 CURRENT OILFIELD ASSUMPTIONS**

Simulation models generally assume that horizontal wells either leak fluid into the reservoir uniformly or exhibit a uniform pressure profile along the well length, mostly for simplicity, when calculating productivity indexes (PI). Babu and Odeh (1988) created a PI relationship for the uniform flux assumption. Many other PI relationships have been proposed (Chen and Asaad, 2005; Economides et al., 1991; Giger, 1985; Helmy and Wattenbarger, 1998; Joshi, 1986; Lu and Tiab, 2007; Mutalik and Godbole, 1988). A comprehensive review of productivity indexes was created by Choi et al. (2008). Babu and Odeh (1988) have a series of discussions at the end of their paper, where Brigham, Peaceman and others discuss the merits of uniform pressure versus uniform flux.



Goode and Kuchuk (1991) developed a PI relationship for uniform pressure using pressure averaging that is generally recognized as better than uniform flux. The assumption of uniform pressure may lead to significant inaccuracies as a pressure gradient is required for flow through the well. Novy (1995) analyzed horizontal production wells and concluded that if frictional losses were roughly 15% of the pressure drawdown at the toe of the well, frictional losses could create at least a 10% reduction in production. Hill and Zhu (2008) examined the relative importance of pressure decreases in horizontal production wells by using a dimensionless quantity called the Horizontal Well Number that included a reservoir geometric factor. Unlike the previously mentioned studies, Ouyang et al. (1998) developed a pressure correlation that included both production and injection wells. They determined that turbulent flow in injection wells increases frictional pressure losses whereas it decreases frictional pressure losses in production wells. In this model, laminar flow only was assumed because highly viscous polymers dramatically reduce Reynolds Numbers.

High-viscosity fluid injection, such would be the case with EOR processes that employ polymer, leads to a pressure drop that results in an uneven injection profile. The uneven injection profile can result in less oil recovery. While, water is not viscous enough to produce a significant pressure drop in wells, the EOR polymer solutions can be sufficiently viscous. Chapter 4 discusses scenarios in which the viscous pressure drop is relevant.

The objective of this work is to develop a more accurate relationship for pressure in horizontal wells for both Newtonian and non-Newtonian fluids and determine the effect on injectivity patterns. Vicente et al. (2004) developed a fully implicit simulator that couples wellbore hydraulics and reservoir dynamics but it only incorporates

Newtonian fluids. Ozkan et al. (1995) created flux and pressure relationships for flow in a horizontal well but non-Newtonian fluids were not included. Furthermore, their equations were not easily applied to a finite difference simulator. Ozkan et al. (1995) conclude that if the horizontal production well has a small reservoir drawdown, the exclusion of the horizontal pressure drop can lead to erroneous results. In other words, the uniform pressure assumption is only valid for large reservoir drawdowns.

Horizontal wells have different completion types (gravel packs, perforations, etc.), more discussion can be found in Chapter 5, and some studies have been conducted to determine their effect on axial pressure profiles. Ouyang et al. (1998) included completion technology in their model for both injectors and producers. Yalniz and Ozkan (1998) concluded that a perforated well produces less axial pressure drop than an unperforated well unless the influx rate is large compared to the axial volumetric flow rate. Similarly, Yuan et al. (1998) concluded that perforation density along with the influx vs. axial volumetric flow rate ratio dramatically impact the axial pressure drop. Su and Gudmundsson (1994) concluded that 80% of pressure drop in horizontal wells results from friction with 15% from mixing because of perforations.

## **1.2 OTHER SCIENTIFIC APPLICATIONS WITH PERMEABLE WALLS**

The study of flow in tubes with permeable walls has applications outside of the oilfield, for instance, renal tubules. Chaturani and Ranganatha (1990) developed numerical solutions for Newtonian fluids in renal tubules by solving a second order differential equation using the fourth-order Runge-Kutta method. Macey (1963) concluded flow in renal tubules is comparable to Poiseuille flow under many circumstances. Radhakrishnamacharya et al. (1981) examined renal tubules assuming converging and diverging ducts with exponential axial flux reduction. Marshall and

Trowbridge (1974) developed a correlation for Newtonian flow with application to renal tubules. Fluids flow through the renal tubule (which is a cylindrical tube) with seepage occurring across the porous walls through the kidneys. Since this is analogous to the injection of fluids into hydrocarbon reservoirs, and quite relevant to the present research; their work is reviewed below in some detail here.

Marshall and Trowbridge (1974) assumed incompressible flow which is reasonable for a polymer flood considering water is the primary component of the fluid. They also assumed that Reynolds Number is sufficiently small such that inertial terms are negligible. Thus, the equations they derived were based on the Stokes equations (Equation 1.1 and Equation 1.2) along with the continuity equation (Equation 1.3) in cylindrical coordinates.

$$\frac{1}{\mu} \frac{\partial p}{\partial r} = \frac{\partial^2 v_r}{\partial r^2} + \frac{1}{r} \frac{\partial v_r}{\partial r} - \frac{v_r}{r^2} + \frac{\partial^2 v_r}{\partial z^2} \quad (1.1)$$

$$\frac{1}{\mu} \frac{\partial p}{\partial z} = \frac{\partial^2 v_z}{\partial r^2} + \frac{1}{r} \frac{\partial v_z}{\partial r} + \frac{\partial^2 v_z}{\partial z^2} \quad (1.2)$$

$$\frac{\partial(rv_r)}{\partial r} + \frac{\partial(rv_z)}{\partial z} = 0 \quad (1.3)$$

They also assume a constant pressure at the end of the tube ( $z = L$ ). This constant pressure assumption is analogous to approaches used in reservoir simulators where each well is divided into grid blocks and one pressure value is assigned to a single grid block. Two adjoining grid blocks can have different pressures; therefore, the constant pressure boundary is applicable for only one grid block. Consequently, the constant pressure boundary along the whole renal tubule is comparable to a single pressure value for one grid block.

For the purposes of liquid injection in wells, the pressure relationship is given by Equation 1.4.

$$P^* = \frac{p - p_T}{P_o - p_T} = \left\{ 1 + 2\gamma^* - 4\gamma^* \left( \frac{r}{R_w} \right)^2 \right\} \left[ \cosh \left( 4\sqrt{\gamma^*} \frac{z}{R_w} \right) - \frac{1}{C_L} \sinh \left( 4\sqrt{\gamma^*} \frac{z}{R_w} \right) \right] \quad (1.4)$$

where,

$$\gamma^* = \frac{k}{R_w t} \quad (1.5)$$

Equation 1.5 describes a conductivity ratio,  $\gamma^*$ , with the permeability of the porous medium,  $k$ , divided by the well radius,  $R_w$ , multiplied by the reservoir thickness,  $t$ . The equations are from Section 4 of Marshall and Trowbridge (1974), “Pressure and Velocity Solutions for Tubes with Small Wall Permeabilities” because the conductivity ratios,  $\gamma^*$  (Equation 1.5), in oilfield applications could range from approximately 5E-10 ( $k = 5$  D,  $R_w = 0.1$  ft, and  $t = 1$  ft for small grid refinement) to 5E-15 ( $k = 5$  md,  $R_w = 0.5$  ft, and  $t = 20$  ft).

Another dimensionless variable that arises in the above solution is  $C_L$ . Given in Equation 1.6,  $C_L$  includes the pressure drawdown (defined as the entry pressure minus the constant outlet pressure) as well as the viscosity of the fluid, conductivity ratio, well radius and mean inlet velocity,  $V_m^o$ :

$$C_L = \frac{R_w (P_o - p_T) \sqrt{\gamma^*}}{2\mu V_m^o} \quad (1.6)$$

In this work we are concerned with accurately representing the flow of polymer-containing fluids, because polymers have unique properties that make them beneficial and economically viable to be employed in enhanced oil recovery (Lake, 1989; Sorbie, 1991). Polymers used in EOR are typically non-Newtonian (exhibiting shear-thinning and sometimes thickening behavior); this results in some favorable attributes, namely a more favorable mobility ratio (Sorbie, 1991). However, the high viscosity creates an increased pressure drop in the wellbore potentially resulting in an adverse injection

pattern. The coupled representation of the horizontal well and neighboring formation for such non-Newtonian fluid flow, as we attempt here, has not been carried out before.

For shear-thinning and thickening fluids, the wellbore viscosity can be described by a Carreau model (Cannella et al., 1988), Equation 1.7, where the zero shear rate viscosity,  $\mu_o$ , and infinite shear rate viscosity,  $\mu_\infty$ , values are experimentally determined. The two fitting parameters,  $\lambda$  and  $n_1$ , are also experimentally determined while  $\dot{\gamma}$  is the shear rate.

$$\mu_{well} = \mu_\infty + (\mu_o - \mu_\infty) \left( 1 + (\lambda_1 \dot{\gamma})^\alpha \right)^{(n_1-1)/\alpha} \quad (1.7)$$

No thickening occurs in a wellbore for most polymers because, unlike typical porous media which have converging and diverging pore geometry, no elongation of the polymer molecular chains occurs which would increase the inter-chain links (Maerker and Sinton, 1986). However, the apparent viscosity in the reservoir formation is calculated using the Unified Viscosity Model (UVM), proposed by Delshad et al. (2008), Equation 1.8, which accounts for thickening in porous media for viscoelastic fluids. The constants,  $\mu_o$ ,  $\mu_\infty$ ,  $\lambda_1$ ,  $n_1$ ,  $\mu_{max}$ ,  $\tau_r$ ,  $\lambda_2$ , and  $n_2$ , are experimentally determined by a best fit approach using laboratory data. In a reservoir, the polymer traverses a tortuous path through the porous media. Consequently, the polymer chains increase their inter-chain interactions. Without sufficient time to relax to its original shape, the apparent viscosity can increase (Maerker and Sinton, 1984). Therefore, the apparent viscosity is a function of the Deborah number, a ratio of the relaxation constant,  $\tau_r$ , associated with the particular chain and residence time in a pore (Delshad et al., 2008).

$$\mu_{res} = \mu_\infty + (\mu_o - \mu_\infty) \left( 1 + (\lambda_1 \dot{\gamma}_{eff})^\alpha \right)^{(n_1-1)/\alpha} + \mu_{max} \left( 1 - e^{-\{(\tau_r \lambda_2 \dot{\gamma}_{eff})^{n_2-1}\}} \right) \quad (1.8)$$

The shear rate in Equation 1.7 is different than the shear rate in Equation 1.8. The effective shear rate in porous media is calculated by using Equation 1.9 where  $n_1$  is the

shear-thinning index from Equation 1.7,  $k_{rw}$  is the relative permeability to water,  $S_w$  is the water saturation, and  $v_w$  is the Darcy velocity. Wreath et al. (1990) detail the values of  $\kappa$ , an empirical constant that is different for many different cases. For the equation derivation section, we are concerned only with single phase flow, so the relative permeability and saturation are given values of one in Equation 1.9.

$$\dot{\gamma}_{eff} = \kappa \left[ \frac{3n_1 + 1}{4n_1} \right]^{n_1/n_1 - 1} \left[ \frac{v_w}{\sqrt{k k_{rw} S_w \phi}} \right] \quad (1.9)$$

Computational fluid dynamics (CFD) modeling was utilized in this work to develop a new correlation for pressure drop and leakage of viscoelastic polymers in horizontal wells. Although the solution proposed by Marshall and Trowbridge (1974) provides a starting point, their model is invalid for non-Newtonian flow and the relatively high Reynolds Numbers observed in wells. The goal is to create a closed-form model to replace the current uniform pressure assumption in reservoir simulators that better predicts hydrocarbon recovery during a polymer injection process.

Chapter 2 details the model specifications including the governing physics, boundary conditions, and size optimization. Chapter 3 examines the Marshall and Trowbridge (1974) equation and its limitations while presenting non-Newtonian alterations to properly account for varying viscosities. A brief examination into the magnitude of axial pressure drop from highly viscous fluids is presented at the end of the chapter with a final Inclusive Pressure Equation (IPE) that accounts for both Newtonian and non-Newtonian fluids with any well and reservoir properties. Chapter 4 discusses the implementation of the Inclusive Pressure Equation in a reservoir simulator, UTCHEM, and the corresponding ramifications for oil recovery. Chapter 5 applies the IPE to two

different completion types, gravel packs and perforations. Chapter 6 concludes with a final summary of the presented results and some recommendations for future research.

The appendices follow in the same order as the chapters. Appendix A provides a detailed guide to building the model in COMSOL Multiphysics<sup>TM</sup>. Appendix B explores the Newtonian results for the Marshall and Trowbridge (1974) equation with Appendix C providing the non-Newtonian results. Appendix D includes the UTCHEM results and a discussion of the new UTCHEM code. Lastly, Appendix E presents more results for gravel packs and perforations.

## Chapter 2: MODEL DESCRIPTION

The Marshall and Trowbridge (1974) solution for leakage of Newtonian fluids in permeable tubes is insufficient for oil field applications including the injection of non-Newtonian polymers. The partial differential equations given in Equation 1.1, Equation 1.2, and Equation 1.3 are too complicated to analytically solve without making simplifying assumptions such as negligible inertial forces. Also, the viscosity of non-Newtonian polymers is a nonlinear function of shear rate and the solution requires an iterative technique. Hence, CFD modeling was employed to create a solution. COMSOL Multiphysics<sup>TM</sup> software is a finite element simulator that has the capability of combining different physics governed by different differential equations. In this work, the momentum and continuity equations, Equation 2.1 and Equation 2.2 that govern the fluid flow in the wellbore, were coupled with Darcy's law, Equation 2.3 that governs the fluid flow in the neighboring reservoir formation.

$$\rho(\vec{v} \cdot \nabla)\vec{v} = \nabla \cdot \left\{ P + \mu_{app} \left( \nabla \vec{v} + (\nabla \vec{v})^T \right) \right\} \quad (2.1)$$

$$\nabla \cdot \vec{v} = 0 \quad (2.2)$$

$$\vec{v} = -\frac{k}{\mu} \nabla \cdot P \quad (2.3)$$

As a result of the length of horizontal wells, the entire well could not be modeled in COMSOL because of memory and computational limitations. Consequently, each segment of the well was modeled separately then added together to simulate the entire well. Figure 2.1 depicts an entire horizontal well with the green lines demarcating the segment that is simulated.



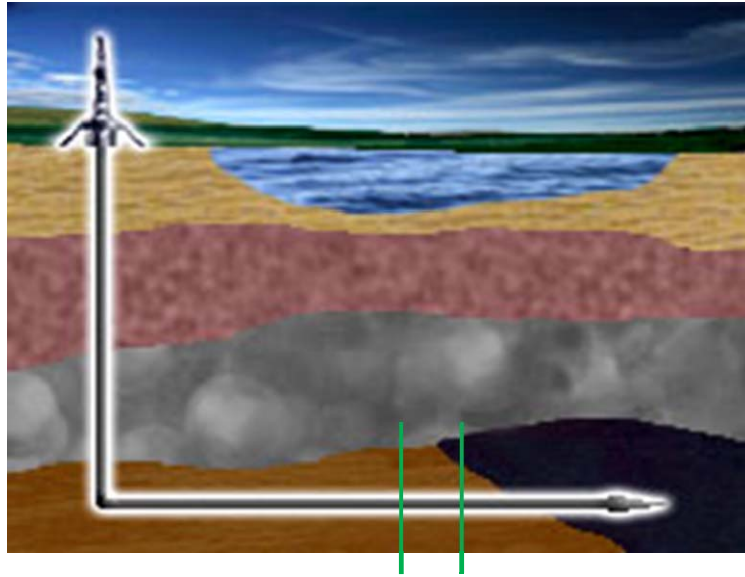


Figure 2.1: A horizontal well with the green lines representing the segment that is being modeled (Signal Oil and Gas).

Figure 2.2 depicts a well segment with the imposed boundary conditions as modeled in COMSOL. The computational domain has radial symmetry. The small rectangular section at the bottom is the wellbore (radial dimension highly exaggerated in the schematic) where the momentum and continuity equations, Equation 2.1 and Equation 2.2, govern the flow of the fluid; meanwhile, the larger rectangle above is the reservoir where Darcy's law, Equation 2.3, governs the flow.

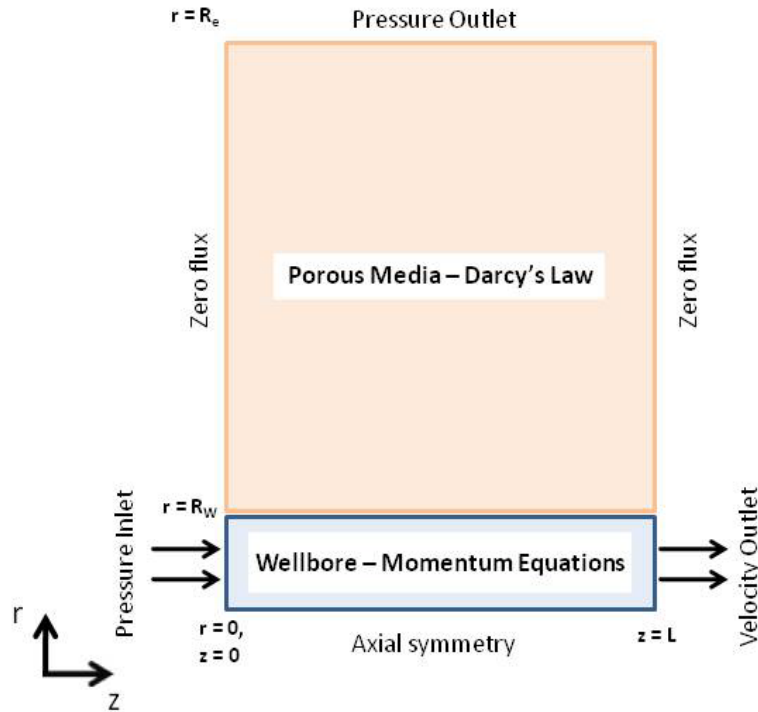


Figure 2.2: COMSOL model with the corresponding physics and boundary conditions.

An axial symmetry boundary was imposed at  $r = 0$  about which the entire model was rotated. The wellbore had a constant pressure inlet (Equation 2.4) corresponding to  $P_o$  as seen in Equation 1.4 and Equation 1.6. The constant pressure inlet is analogous to a pressure constrained well when considering the entire well. Individual well segments were modeled; therefore, the constant pressure inlet becomes the inlet pressure of a given segment. The injection pressure could be obtained from a pressure gauge down hole.

$$P = P_o \quad @ z = 0, 0 \leq r \leq R_w \quad (2.4)$$

$$v = V_o \quad @ z = L, 0 \leq r \leq R_w \quad (2.5)$$

The outlet of the wellbore was modeled with a uniform velocity, Equation 2.5, which was required to simulate part of the well. Since the entire well could not be simulated, each well segment that was simulated was added to the previous segment and

next segment. Therefore, the volumetric fluxes through each segment were continuous. The uniform velocity boundary condition is only an approximation because, of the computational domain only being a well section, the velocity profile in the well is not uniform. A prescribed profile might be preferable but with varying shear rates the profile is not constant (Bird et al., 2007). With the thinning nature of the viscoelastic fluid, however, a more slug-like, almost uniform, profile rather than a parabolic one is usually observed. The uniform velocity was chosen over the parabolic profile because the well inlet did not have a prescribed profile; consequently, matching segments were more readily attained.

The interface between the well and the reservoir requires continuity; the longitudinal distributions of the velocity and pressure in the wellbore must match those in the reservoir. As a result, the outlet boundary of the well at  $r = R_w$  was chosen to be the reservoir velocities. The inlet boundary of the reservoir at  $r = R_w$  was chosen to be the well pressure. The conditions can be reversed (i.e., outlet boundary of the well at  $r = R_w$  could be the reservoir pressure and the inlet boundary of the reservoir at  $r = R_w$  could be the well velocities) but COMSOL appears to solve more easily with this arrangement. Implementation regarding these boundary conditions can be found in Appendix A.

Radial flow was assumed along the entire length of the well because the toe of the well was closed to flow; therefore, no “spherical flow” occurred at the toe. Details regarding flow regimes in horizontal wells can be found in Issaka and Ambastha (1999). Figure 2.3 illustrates the radial flow assumption by depicting an open-end toe with spherical flow (top) and a closed-end toe resulting in radial flow (bottom).

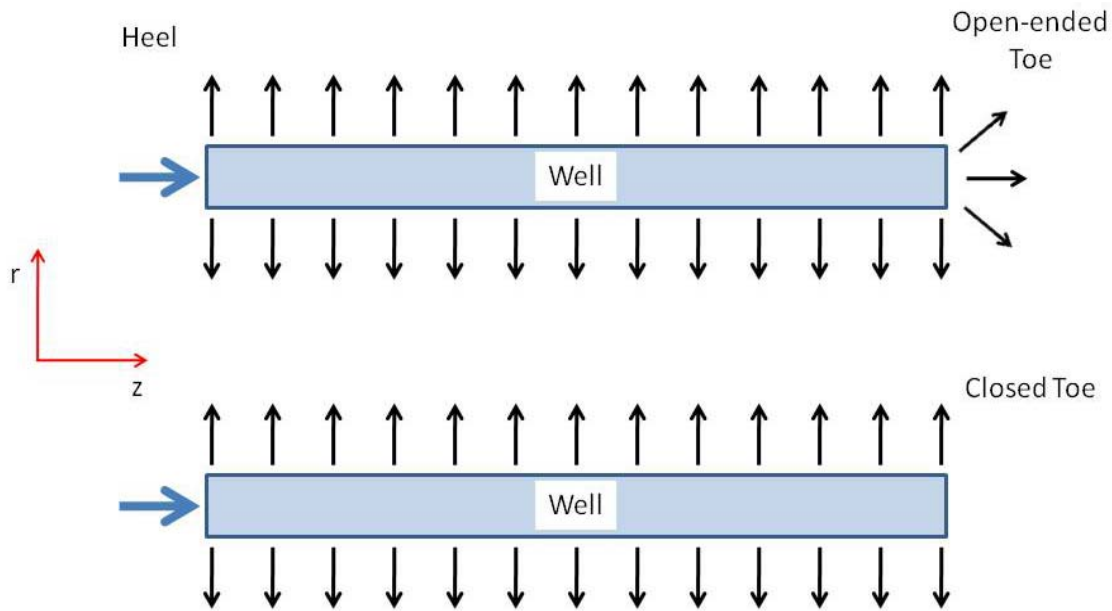


Figure 2.3: An open-ended toe with spherical flow (top) versus a closed toe with radial flow the entire length of the well (bottom).

To generate the radial flow state that is expected for the well-reservoir “section”, the reservoir was prescribed no flux boundaries at  $z = 0$  and  $z = L$ ; no cross-flow was assumed. A pressure gradient exists down the well which results in some flow parallel to the well in the reservoir. However, the no flux assumption was reasonable because the  $z$  velocity (parallel to the well) was orders of magnitude lower than the  $r$  velocity (perpendicular to the well).

The outlet boundary, at  $r = R_e$ , of the reservoir was the constant pressure boundary,  $p_T$ , as given in Equation 1.4 and 1.7. The  $p_T$  value would correspond to the pressure of the gridblock, e.g., next to the well gridblock, in a finite difference simulator. Finite difference simulators create a single property value (e.g. pressure, saturation, etc.) for an entire grid. The well segment in any given block injects fluid based on the constant block pressure. This should be a reasonable assumption provided the well blocks are not

too large (a factor dependent on the pressure drop in a given segment). A detailed description of model formulation in COMSOL can be found in Appendix A.

The uniform well velocity outlet allows different flow rates to be created in the wellbore. As the outlet velocity is increased, the wellbore flow rate increasing and vice versa. The drawdown, the well pressure ( $p$ ) minus the constant pressure outlet ( $p_T$ ), alters the leakage per unit length along the well into the reservoir. A large drawdown creates a large leakage rate. Therefore, the entire well can be simulated by matching inlet and outlet conditions. Entry and exit effects occur in the well because of the non-ideal boundary conditions (i.e., a lack of a velocity profile). The induced error from the wellbore outlet velocity was negligible for Newtonian fluids so the inability to create an inlet velocity profile was assumed negligible as well.

Because of the velocity dependent nature of the non-Newtonian flow problem, a modified Darcy's law, Equation 2.6 including the apparent viscosity in the reservoir ( $\mu_{res}$ ), Equation 1.8, could not be implemented directly in COMSOL because Darcy's law is pressure dependent only.

$$\vec{v} = -\frac{k}{\mu_{res}} \nabla \cdot P \quad (2.6)$$

Therefore, the Brinkman equation, Equation 2.7, which is pressure and velocity dependent as well as available in COMSOL, was used as a numerical tool to include nonlinearities due to non-Newtonian flow.

$$\nabla P = -\frac{\mu}{k} \vec{v} + \mu_{eff} \nabla^2 \vec{v} \quad (2.7)$$

The Brinkman equation is a semi-empirical alteration to Darcy's law to account for inertial effects for high-velocity gas flow in porous media (Brinkman, 1947). In the case of Newtonian, creeping flow, the inertial effects go to zero and the equation reduces

to Darcy's law. Durlofsky and Brady (1987) as well as Khaniaminjan and Goudarzi (2008) performed comparisons for the Brinkman equation and the results indicated Brinkman was a useful correlation for limited applications, typically for flow in low porosity rock. COMSOL employs Equation 2.8 for the effective viscosity,  $\mu_{\text{eff}}$ ; therefore, if the porosity,  $\phi$ , is very large value (i.e., 1E10), the equation reduces to Equation 2.3, Darcy's Law.

$$\left(\frac{1}{\phi}\right)\left[\mu\{\nabla\bar{v} + (\nabla\bar{v})^T\} - \left(\frac{2\mu}{3} - \kappa_{dv}\right)\right] \quad (2.8)$$

$$\bar{v} = -\frac{k}{\mu}\nabla \cdot P \quad (2.3)$$

While, porosity is physically constrained to be between 0 and 1, for this study the large value was assigned mathematically to reduce Brinkman equation to Darcy's Law. The altered Brinkman equation was compared to Darcy's Law resulting in a 1.53% error.

## 2.1 RESERVOIR SIZE OPTIMIZATION

For a non-Newtonian fluid, the apparent viscosity becomes the low-shear limit Newtonian viscosity at some radius away from the well because the shear rate decreases. Three reservoir thicknesses, 1 meter, 10 meters, and 30 meters, were tested with the well and reservoir properties listed in Table 2.1.

Table 2.1: Well and reservoir properties used to determine reservoir size optimization.

<b>Inlet pressure</b>	1500 psi
<b>Well radius</b>	0.35 ft
<b>Segment length</b>	100 m
<b>Reservoir permeability</b>	500 md
<b>Leakage rate</b>	5 STB/D/m

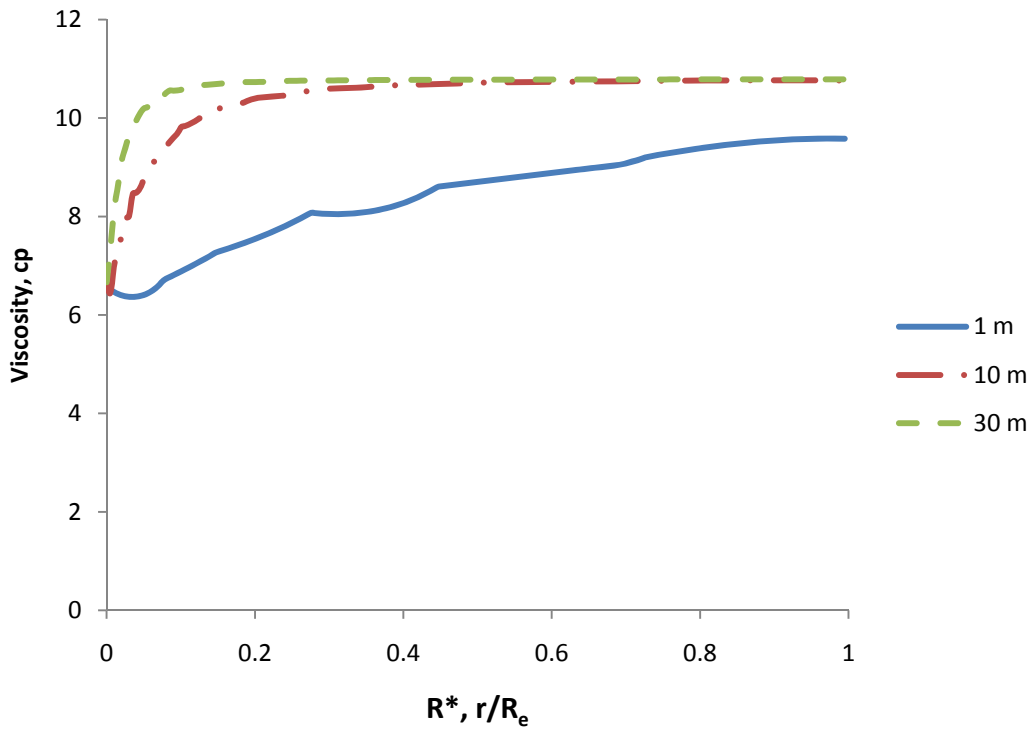


Figure 2.4: Reservoir thickness optimization to account for viscosity variation.

Figure 2.4 depicts the leveling of the reservoir viscosity near 10 meters for the 10 meter case and the 30 meter case (0.33). Clearly, 1 meter is an insufficient thickness to capture all of the viscosity variation. At 10 meters, the shear rate was slightly below the zero viscosity plateau, the different viscosity regions are discussed in Chapter 3, but the slope of the viscosity at 10 meters is almost zero, indicating an asymptote. The reservoir thickness was chosen to be 10 meters for all Newtonian, shear-thinning, and shear-thickening test cases; using a larger reservoir thickness did not affect our numerical results.

## 2.2 MESH OPTIMIZATION

An analysis on the proper mesh size for the finite-element computation was performed to determine the optimum number of elements for each set of model dimensions. Using the model in Figure 2.2, the boundary between the wellbore and the reservoir is where the mesh refinement is required. In finite difference simulators, grid refinement is usually restricted to areas such as wells, faults, and areas of heterogeneity where the solution changes most rapidly (Aziz and Settari, 1979). In our model, the refinement was on both sides of the boundary between the well and reservoir. Figure 2.5 portrays the convergence of the radial velocity by refining the mesh. Appendix A details the construction of the model and step 14 conveys the method of mesh refinement.

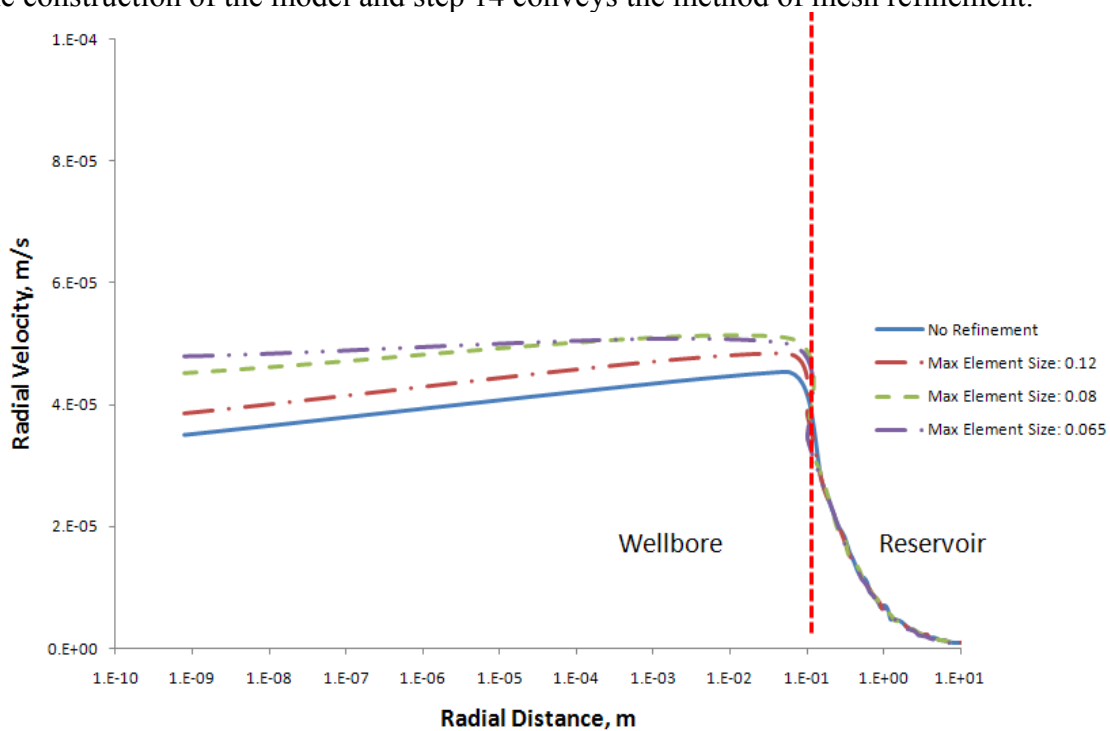


Figure 2.5: Radial velocity convergence as a function of mesh refinement.



Horizontal well lengths and radii can vary as well as many different completion techniques can be employed. In this work, the wells are all assumed to be open hole for the entire lateral length and the vertical and heel sections of the well are ignored. The well lengths varied from 600 meters to 3,000 meters and the well radii vary from 0.25 feet to 0.5 feet.

As the mesh was refined, the wellbore velocity increased while the reservoir velocity remained virtually unchanged. The final two velocity profiles are nearly identical; therefore, convergence has been achieved. A refinement of 0.08 meters as the maximum grid size at  $r = R_w$ ; more explanation of the mesh options can be found in Appendix A and the COMSOL help guide, was determined to provide acceptable accuracy. The axial pressure profiles for each mesh refinement were identical. The radial velocity values and consequently the viscosity values were dependent on mesh refinement; however, axial pressure was not a function of the mesh refinement.

### **2.3 COMSOL EXAMPLE**

Newtonian cases can be solved directly in COMSOL. To account for non-Newtonian effects in the wellbore, COMSOL includes a non-Newtonian option. For flow in porous media, non-Newtonian effects required the addition of the UVM (Equation 1.8). However, the viscosity is velocity dependent; the initial value was given by solving a Newtonian case and using it as the current solution. Figure 2.6 depicts the pressure field for the initial Newtonian solution (top) and a UVM solution (bottom). The solving manager was changed to Current Solution as described in the Appendix A. The viscosity equation in the subdomain settings was changed to the UVM.

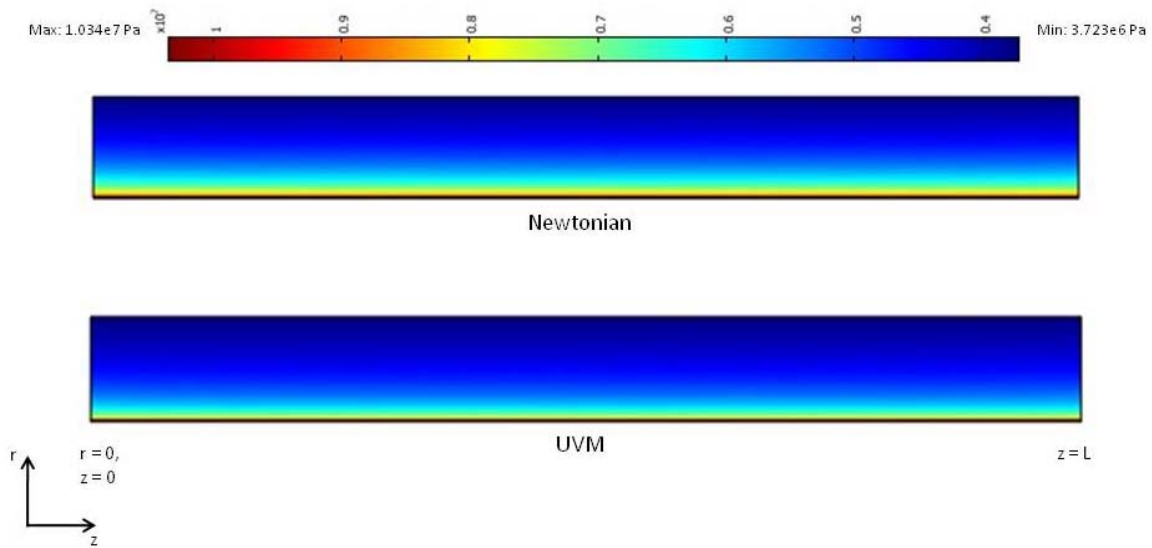


Figure 2.6: Pressure plot for a Newtonian COMSOL example vs. UVM example.

The solution above required no changes to COMSOL. The only required correction was the large porosity value to mathematically reduce Brinkman equations to Darcy's Law. The instructions for building the model can be found in Appendix A.

## Chapter 3: RESULTS AND DISCUSSION

The Marshall and Trowbridge (1974) pressure solution given in Equation 1.4 is only valid for Newtonian fluids and assumes no inertial effects. Tests were performed to verify if the COMSOL numerical solution agrees with the Marshall and Trowbridge (1974) analytical solution. Limitations of the solution when it was applied to oil field settings were examined and a modification was employed to better account for the variety of conditions encountered in the petroleum industry.

### 3.1 NEWTONIAN EXAMINATION

Using a low volumetric flux in the well and a low leakage rate for Newtonian fluids, a test was performed to validate the COMSOL predictions. Table 3.1 lists the constant model properties for all of the Newtonian tests conducted in this chapter with the exception of viscosity where some different values were tested; those values appear in Table B.1.

Table 3.1: Model properties used in the examination for the Newtonian fluid of Marshall and Trowbridge (1974).

---

<b>Inlet pressure</b>	1500 psi
<b>Well radius</b>	0.35 ft
<b>Segment length</b>	100 m
<b>Reservoir permeability</b>	1 D
<b>Reservoir thickness</b>	10 m
<b>Fluid viscosity</b>	128 cp

The COMSOL result shows near perfect agreement with the analytical equation derived by Marshall and Trowbridge (1974) in Figure 3.1. The agreement was expected

because the Reynolds Number in the wellbore was low, 276, the leakage rate was low (1.3 STB/D/m), and the leakage rate divided by the well flow rate was very low, 0.0004. Therefore, the inertial effects should be minimal.

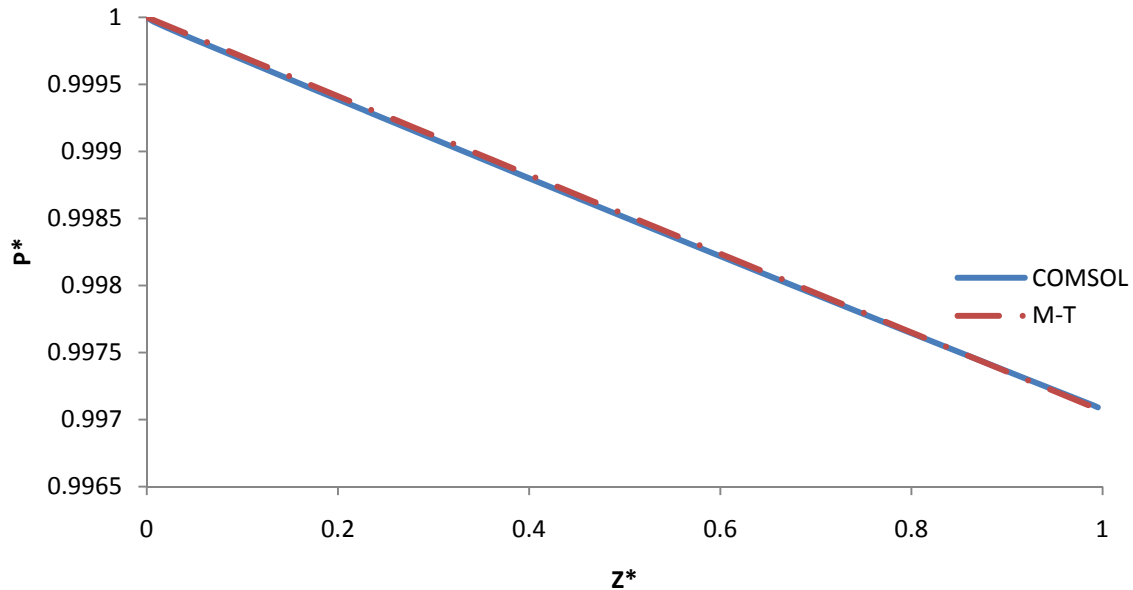


Figure 3.1: Marshall and Trowbridge solution, M-T, and the COMSOL solution showing near perfect agreement along the well.

The pressure drop illustrated in Figure 3.1 is virtually identical to the Hagen-Poiseuille Equation (Bird et al., 2007), Equation 3.1 for pure unidirectional laminar flow in a capillary tube, despite the fact that approximately 4% of the injected fluid was lost to the reservoir.

$$\Delta P = \frac{8Q\mu L}{\pi R_w^4} \quad (3.1)$$

The error was around 1% which is suitable for our applications. The very small non-dimensional pressure drop witnessed on the vertical axis is common throughout the thesis. An examination of the relevant pressure drops is presented in Chapter 4 with a brief discussion later in Chapter 3. At the limiting case approaching laminar flow in a

capillary tube, COMSOL and Marshall and Trowbridge (1974) yield nearly identical and accurate results.

However, when the leakage rate divided by the well flow rate ( $Q_y/Q_z$ ) increased, the COMSOL result deviated from the Marshall and Trowbridge equation (1974). Inertial effects were deemed to have caused the discrepancy. To mathematically demonstrate the increasing error, the COMSOL pressure drop was divided by the analytical solution for each point along the well. The ratio of the two solutions was plotted and a 2<sup>nd</sup> order polynomial, Equation 3.2, appeared to fit the data well for dozens of simulations. A brief expedition into the physical meaning of the coefficients was attempted; however, no conclusion was reached. A more detailed analysis may be beneficial to yield a different pressure correlation. Some of the polynomial plots are shown in Appendix B.

$$\frac{P_{MT}}{P_{COMSOL}} = AZ^{*2} + BZ^{*} + 1 \quad (3.2)$$

If the solutions perfectly match, the ratio would be equal to one at all points thus the polynomial would be equal to one. Therefore, the minimization of the area between the polynomial and the straight line equal to one was considered to obtain the best-fit A and B. To calculate the area difference, the absolute value of the integral of the polynomial evaluated from  $Z^{*} = 0$  to  $Z^{*} = 1$  minus one was taken, Equation 3.3.

$$\Delta Area = \left| 1 - \int_{Z^{*}=0}^{Z^{*}=1} (AZ^{*2} + BZ^{*}) dZ^{*} \right| \quad (3.3)$$

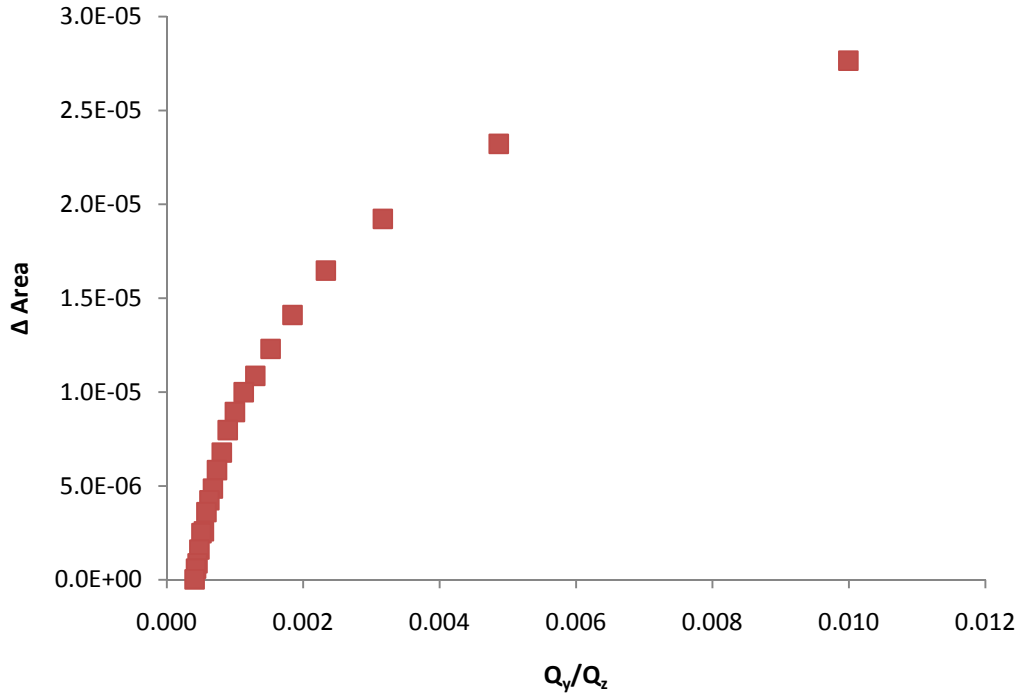


Figure 3.2: Area difference between one and the ratio of the COMSOL solution and Marshall and Trowbridge (1974).

Figure 3.2 is a plot of the error as a function of the ratio between radial and axial flux. At low values of the  $Q_y/Q_z$ , the error is negligible suggesting agreement with the Marshall and Trowbridge (1974) model. Higher values of  $Q_y/Q_z$  suggest deviation from unidirectional flow, which Marshall and Trowbridge (1974) did not rigorously account for in their analytical model. As expected, the figure shows an increase in error with increasing  $Q_y/Q_z$ .

Another limitation of the Marshall and Trowbridge (1974) solution is the injection rate was very low.  $C_L$ , Equation 1.6 shown below, has a strong dependence on the mean inlet velocity,  $V_m^o$ .

$$C_L = \frac{R_w (P_o - p_T) \sqrt{\gamma^*}}{2\mu V_m^o} \quad (1.6)$$

When the inlet velocity (and consequently the Reynolds Number) and leakage rates increase, Marshall and Trowbridge (1974) and COMSOL diverge despite the same  $Q_y/Q_z$  as the low injection rate case. Figure 3.3 illustrates the convergence of the differential area for a high leakage rate (16.67 STB/D/m) and the previously discussed low leakage rate (1.3 STB/D/m).

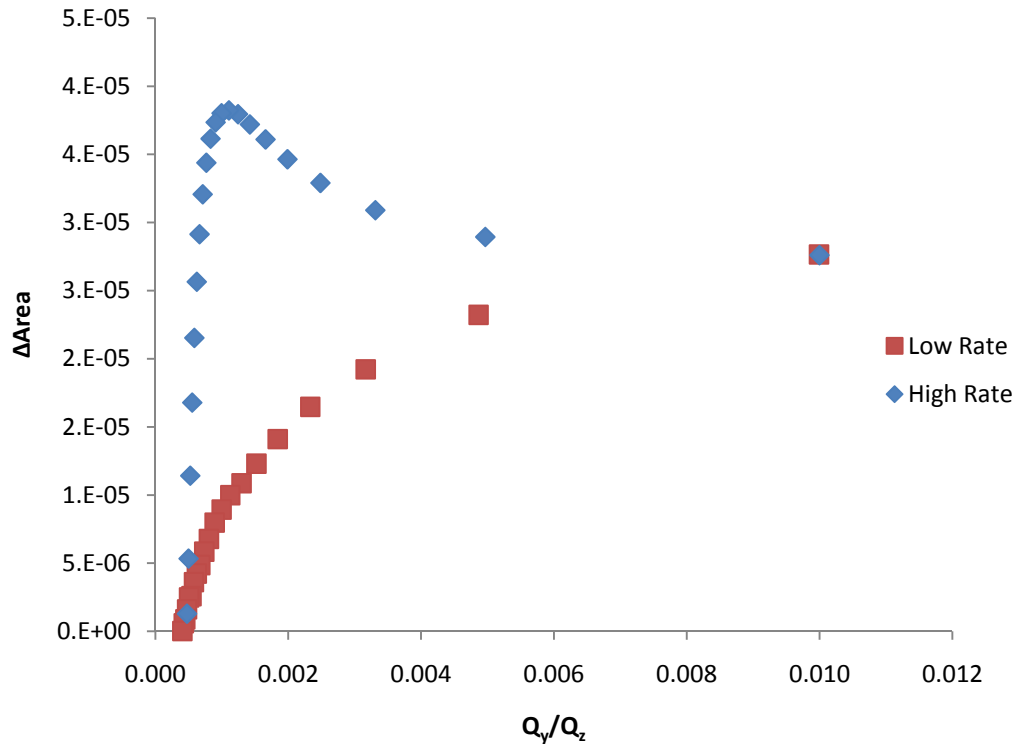


Figure 3.3: Area difference convergence for a high leakage rate (16.67 STB/D/m) and a low leakage rate (1.3 STB/D/m).

Once again, this error was partially attributed to inertial effects but  $V_m^0$  in the high rate case varied from 0.28 ft/s to 5.8 ft/s. Therefore, a correction to better account for the mean velocity variation in the well was examined. Finite difference simulators discretize the reservoir and well into blocks or grids. Instead of a single  $C_L$  value for the entire well as the Marshall and Trowbridge (1974) equation utilizes, one  $C_L$  value per well segment

or grid block is proposed. This modification is a natural result of the boundary conditions discussed in Chapter 2. The constant pressure boundary,  $p_T$ , is valid only for one grid block. Therefore, a new  $C_L$  per grid block would be required simply because the pressure difference varies for each grid block. However,  $p_T$  is not the only variable that changes with axial length, the inlet mean velocity for each grid block can be dramatically different. The altered Marshall and Trowbridge solution is shown in Equation 3.4 and depicted in Figure 3.4 where  $C_{L\_seg}$ ,  $P_{o\_seg}$ , and  $p_{T\_seg}$  are valid only for a given segment.

$$\frac{P - p_{T\_seg}}{P_{o\_seg} - p_{T\_seg}} = \left\{ 1 + 2\gamma * -4\gamma * \left( \frac{r}{R_w} \right)^2 \right\} \left[ \cosh \left( 4\sqrt{\gamma} * \frac{z}{R_w} \right) - \frac{1}{C_{L\_seg}} \sinh \left( 4\sqrt{\gamma} * \frac{z}{R_w} \right) \right] \quad (3.4)$$

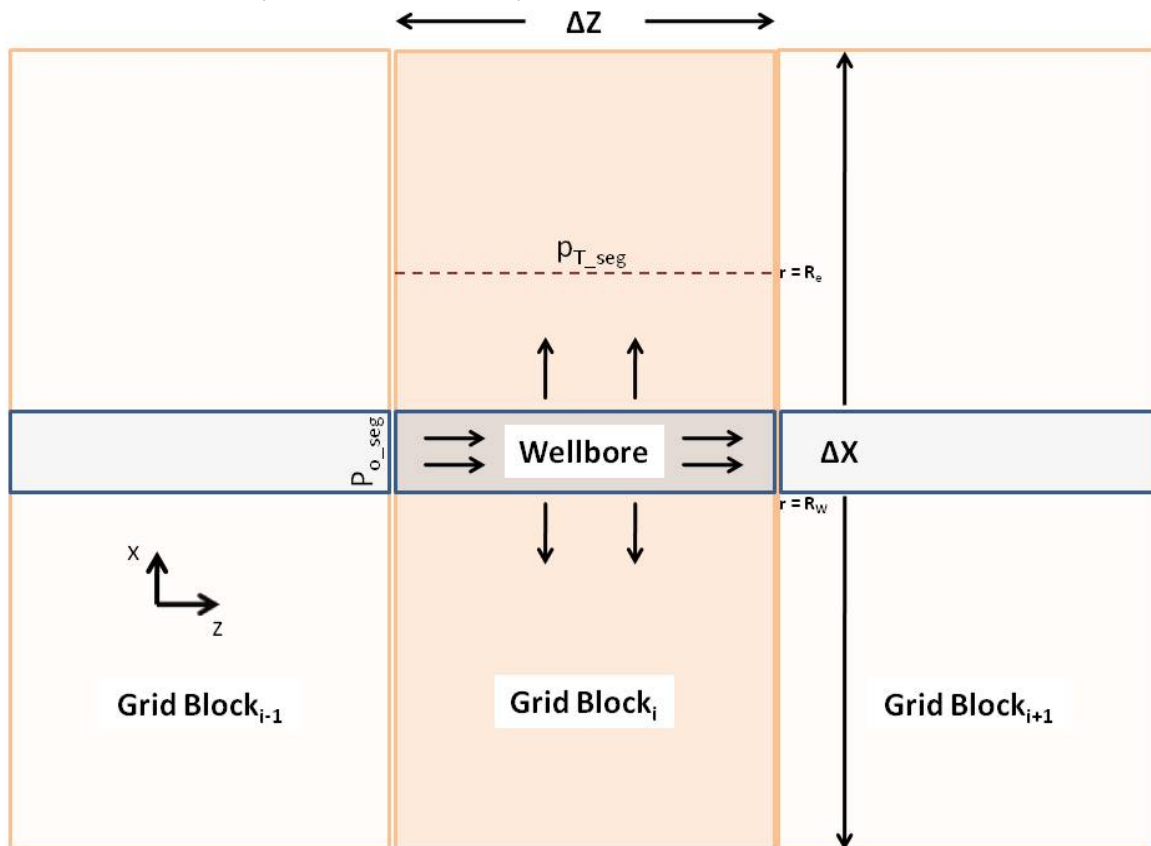


Figure 3.4: A schematic depicting  $P_{o\_seg}$  and  $p_{T\_seg}$  for a given well segment.



A set of 48 tests was performed to determine the accuracy of utilizing one  $C_L$  value per well segment rather than one  $C_L$  for the entire well. Well injection rates varied from 10,000 STB/D to 40,000 STB/D with well lengths of 600 m, 1800 m, and 3000 m. Simulations were also carried out with four different fluid viscosities: 10 cp, 100 cp, 200 cp, and 300 cp. In our paper, COMSOL data series refers to  $P^*$  (the left hand side of Equation 3.4) which is calculated using the COMSOL well axial pressure value. Figure 3.5 is a procession of well segments starting at the heel, 0-100 m, and proceeding to the toe, 500-600 m, for the 600 m, 20,000 STB/D, 300 cp case comparing the COMSOL result to both the Marshall and Trowbridge (1974) solution (M-T) with one  $C_L$  value per well and one  $C_L$  value per well segment labeled New  $C_L$ .

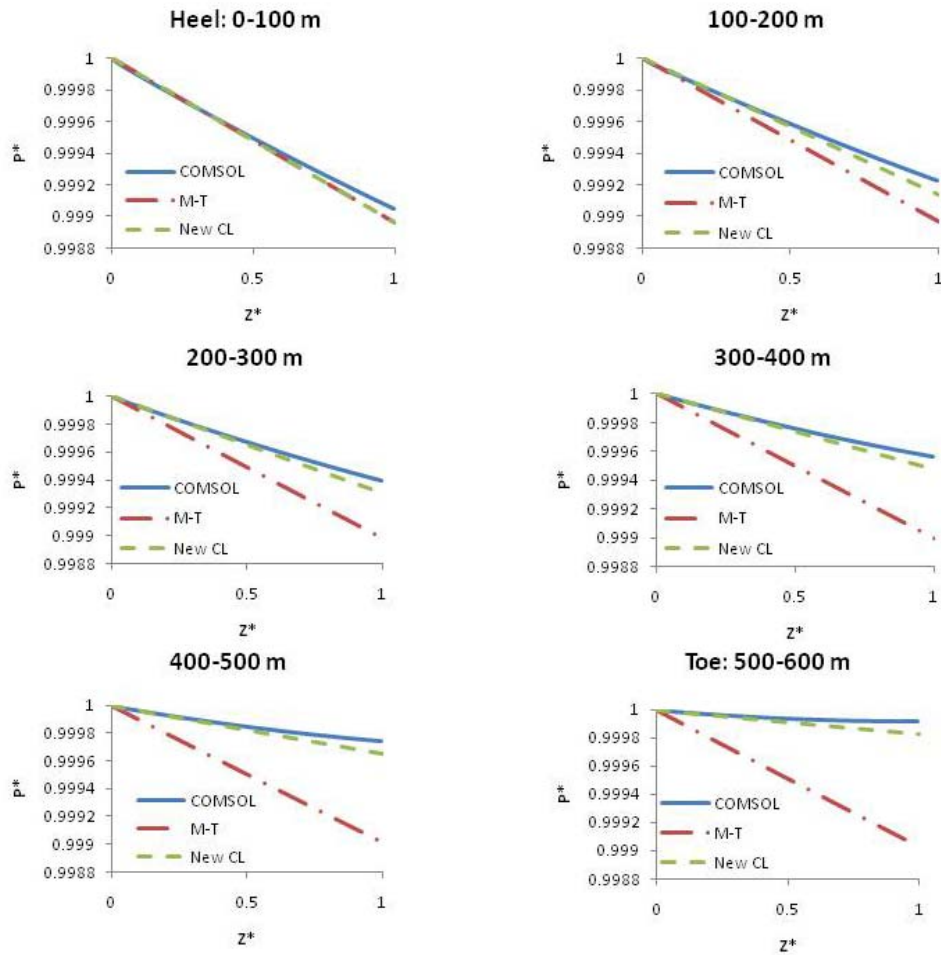


Figure 3.5: Marshall and Trowbridge solution using a different  $C_L$  value for each well segment, New  $C_L$ , and the original Marshall and Trowbridge solution, M-T, compared to the COMSOL solution along the well.

The Marshall and Trowbridge solution appears to become less accurate further down the well. The volumetric fluxes were matched at the inlet and outlet by controlling the constant outlet velocity boundary condition. In other words, the outlet velocity was effectively zero at the toe while the inlet flux was calculated using the boundary integration feature in COMSOL. The constant outlet velocity of the next segment (the segment immediately preceding the toe) was set to create a volumetric flux equal to the

previously modeled segment. In this way, the entire well can be modeled. The solution is identical for the well segment at the heel because  $V_m^0$  is identical in both cases. The better agreement resulting from one  $C_L$  value per segment is apparent.

Another way to quantify the discrepancy between the original Marshall and Trowbridge (1974) equation and the modified equation is to present the pressure value along the entire well. Figure 3.6 presents the same case as that shown in Figure 3.5; however, the vertical axis is pressure rather than dimensionless pressure and the horizontal axis includes all six well segments.

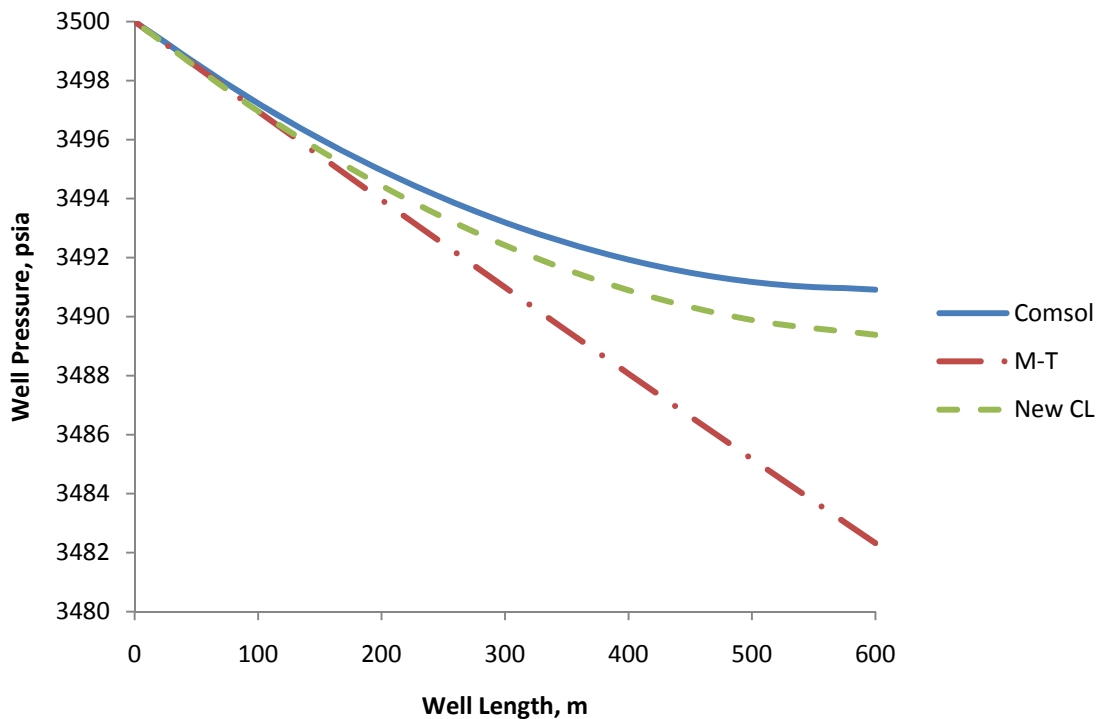


Figure 3.6: Pressure values for modified Marshall and Trowbridge (New  $C_L$ ) and original Marshall and Trowbridge (M-T), compared to COMSOL, for an entire well.

The modified solution demonstrates its effectiveness near the toe of the well (600 m). Instead of dramatically over estimating the pressure drop by using a large  $V_m^0$ , the

corrected  $V_m^o$  approximates the COMSOL solution reasonably well. The Marshall and Trowbridge (1974) equation appears linear because  $C_L$  is small (i.e.  $V_m^o$  is very large) for the entire well. A study could be performed to determine if smaller well segments would yield a better match. Numerical error could occur if the segments were too short.

Despite the improved accuracy from using a single  $C_L$  value for each well segment, leakage rate appears to impact the agreement. Figure 3.7 compares leakage rates of 3.33 STB/D/m, top left, and 10 STB/D/m, top right ( $Q_y/Q_z = 0.000333$ ) and 33.3 STB/D/m, bottom left, and 66.7 STB/D/m, bottom right ( $Q_y/Q_z = 0.00167$ ) for the same parameters given in Table B.1 for the heel of the well.

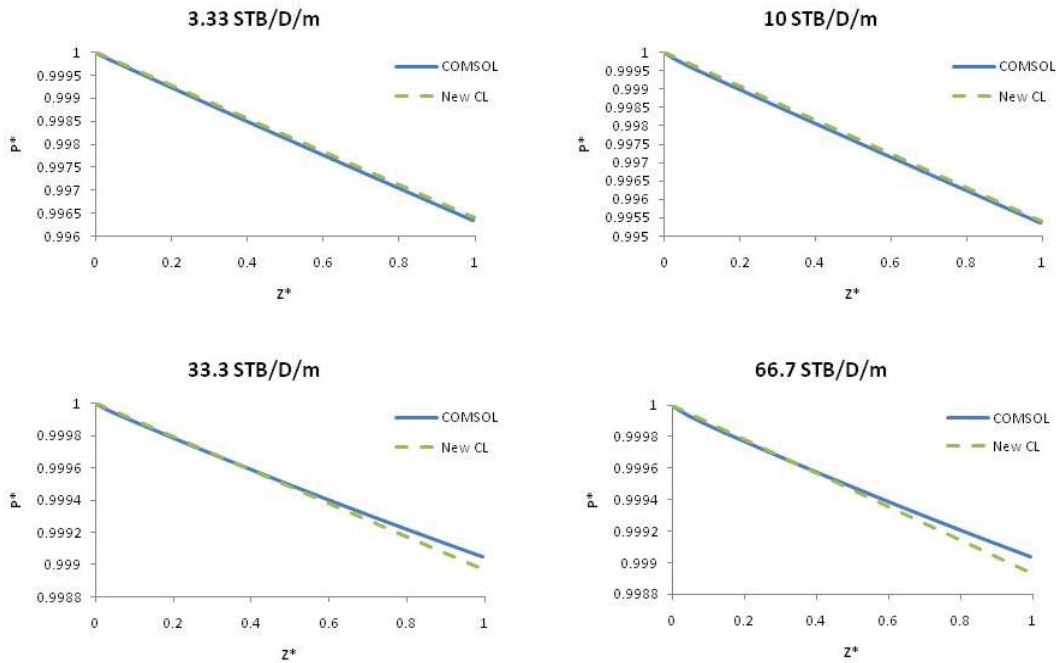


Figure 3.7: Marshall and Trowbridge solution using a different  $C_L$  value for each well segment, New  $C_L$ , compared to the COMSOL solution at the heel of the well for four different leakage rates.

The agreement for the lower leakage rates appears nearly perfect. However, for the higher leakage rates a discrepancy arose toward  $Z^* = 1$ . It appears for lower  $Q_y/Q_z$

values, a single  $C_L$  value for each well segment or grid block should provide sufficient accuracy. More plots can be seen in Appendix B detailing other results from the Newtonian tests.

The results shown in Figure 3.6 were also compared to the Hagen-Poiseuille equation, Equation 3.1. Figure 3.8 includes the Hagen-Poiseuille prediction for Figure 3.6.

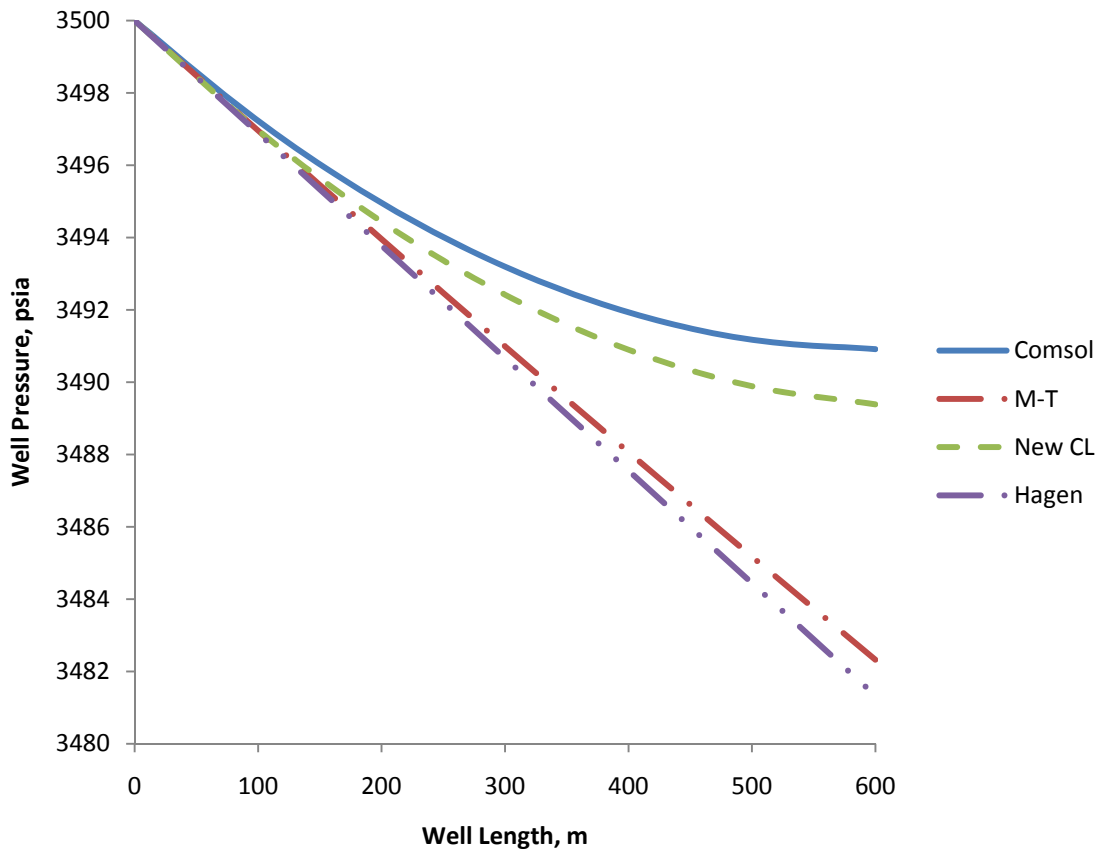


Figure 3.8: Pressure values modified Marshall and Trowbridge (New CL) and original Marshall and Trowbridge (M-T) COMSOL compared to Hagen-Poiseuille (Hagen) for an entire well.

Using the same injection rate of 20,000 STB/D and  $\mu = 300$  cp, Hagen-Poiseuille predicted a pressure drop of 18.7 psi. Marshall and Trowbridge (1974) (Equation 1.4)

predicts 17.7 psi, the modified Marshall and Trowbridge equation (Equation 3.4) predicts 10.6 psi and COMSOL predicts 9.1 psi. Therefore, Hagen-Poiseuille over predicts the pressure drop for a similar reason that the original Marshall and Trowbridge (1974) equation over predicts pressure drop, the axial pressure profile is too dependent on the initial volumetric flux and does not properly account for dramatic changes over the length of the well. Marshall and Trowbridge (1974) account for loss of the fluid; however, their equation appears to be inaccurate for very high volumetric flux differences between the inlet and outlet of a well.

If the Hagen-Poiseuille equation was used for each segment, the predicted total axial pressure drop would be 10.7 psi. A comprehensive comparison of a Hagen-Poiseuille per segment to Marshall and Trowbridge (1974) per segment was not performed.

### 3.2 SHEAR-THINNING

Many fluids, including polymers used in oilfield applications, are non-Newtonian having their viscosity dependent on the shear rate. Multiple equations exist to account for a shear-thinning effect but this work exclusively used the popular Carreau model as given in Equation 1.7 for the apparent well viscosity and shown below.

$$\mu_{well} = \mu_{\infty} + (\mu_o - \mu_{\infty}) \left( 1 + (\lambda_1 \dot{\gamma})^{\alpha} \right)^{(n_1 - 1)/\alpha} \quad (1.7)$$

The apparent reservoir viscosity,  $\mu_{res}$ , was calculated using Equation 3.5 with the shear rate being calculated using Equation 1.9, shown below.

$$\mu_{res} = \mu_{\infty} + (\mu_o - \mu_{\infty}) \left( 1 + (\lambda_1 \dot{\gamma}_{eff})^{\alpha} \right)^{(n_1 - 1)/\alpha} \quad (3.5)$$

$$\dot{\gamma}_{eff} = \kappa \left[ \frac{3n_1 + 1}{4n_1} \right]^{n_1/n_1 - 1} \left[ \frac{v_w}{\sqrt{k k_{rw} S_w \phi}} \right] \quad (1.9)$$

A Carreau fluid has a high and low shear rate plateau with a power-law type relationship between them. Figure 3.9 illustrates the full spectrum of viscosities for a Carreau fluid (Delshad et al. 2008). The viscosity in both the well and reservoir thus now vary with radial distance.

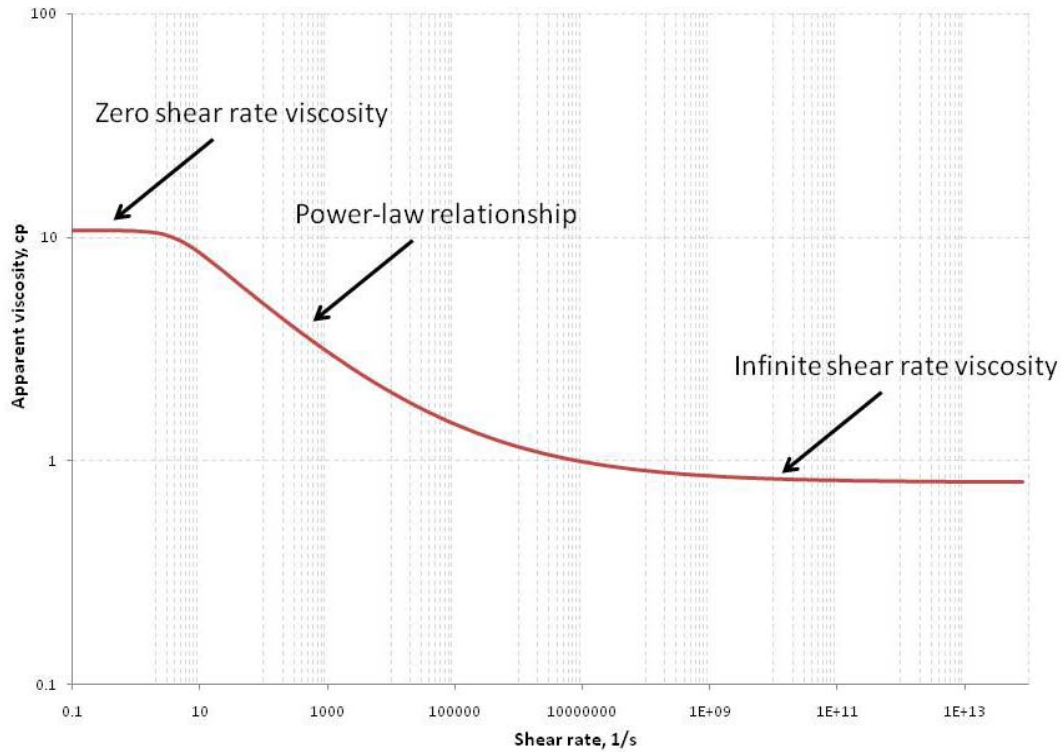


Figure 3.9: Carreau model for the HPAM that was discussed in Delshad et al. (2008).

The greatest shear rates in the wellbore occur at  $r = R_w$ ; therefore, the lowest apparent viscosity in the wellbore occurs at  $r = R_w$ . Likewise, assuming a homogeneous reservoir and radial flow out of the well, the greatest shear rates in the porous media occur at the wall-reservoir interface because the fluid velocities are highest.

The higher shear rates at  $r = R_w$  aid in the injection of the polymer. As a result of the viscosity reduction in both the well and the reservoir, a small pressure drop in the well is expected. To account for the reduced viscosity, the viscosity value in Equation 1.6 was altered to the Carreau relationship of Equation 1.7. With the radial variation of viscosity in the well, the pressure value for the well was calculated at  $r = 0$  but the viscosity at  $r = R_w$  was used to calculate  $C_L$  because it is the viscosity that affects the leakage rate. The viscosity in the reservoir does not appear explicitly in the equations developed by Marshall and Trowbridge (1974). Therefore, a correction to the conductivity ratio, Equation 1.5, was made to emulate the concept of a mobility ratio for two phase flow. Equation 3.6 includes a viscosity ratio added to the conductivity ratio.

$$\gamma^*_{new} = \frac{k}{R_w t} \frac{\mu_w}{\mu_{res}} \quad (3.6)$$

The apparent viscosity in the reservoir was taken to be the viscosity immediately at the well-reservoir interface. Other locations were considered; however, the apparent viscosity at the well-reservoir interface yielded the best results. It follows that the immediate apparent viscosity will impact the well pressure more than a value at some arbitrary distance away. Equation 3.7 is the modification of  $C_L$ , given as Equation 1.6 earlier:

$$C_{L\_new} = \frac{R_w (P_o - p_T) \sqrt{\gamma^*_{new}}}{2 \mu_{well} V_m^o} \quad (3.7)$$

A series of tests were performed to determine the validity of this alteration. At low leakage rates, the shear rates would be low, approximating a Newtonian fluid. Consequently, only high pressure drawdowns (resulting in high axial flux) were tested. Lee et al. (2009) provide data on the shear-thinning rheological behavior of some polymers for different concentrations. Using Figure 1 of Lee et al. (2009), the viscosity



data for 3000 ppm concentration HPAM was digitized (the solid blue line in Figure 3.10) and then shear-thinning parameters (the red points in Figure 3.10) were generated to match the digitized data with very good agreement. The values are listed in Table 3.2. The shear-thickening parameters were arbitrarily created and shown in green in Figure 3.10.

Table 3.2: Shear-thinning and shear-thickening properties of the 3000 ppm HPAM depicted in Figure 1 of Lee et al. (2009).

<b>Shear-thinning</b>		<b>Shear-thickening</b>	
$\mu_0$	128 cp	$\mu_{\max}$	250 cp
$\mu_\infty$	0.8 cp	$\tau_r$	0.023
$\lambda_1$	1 s	$\lambda_2$	0.03 s
$n_1$	0.653	$n_2$	1.5
$\alpha$	2		

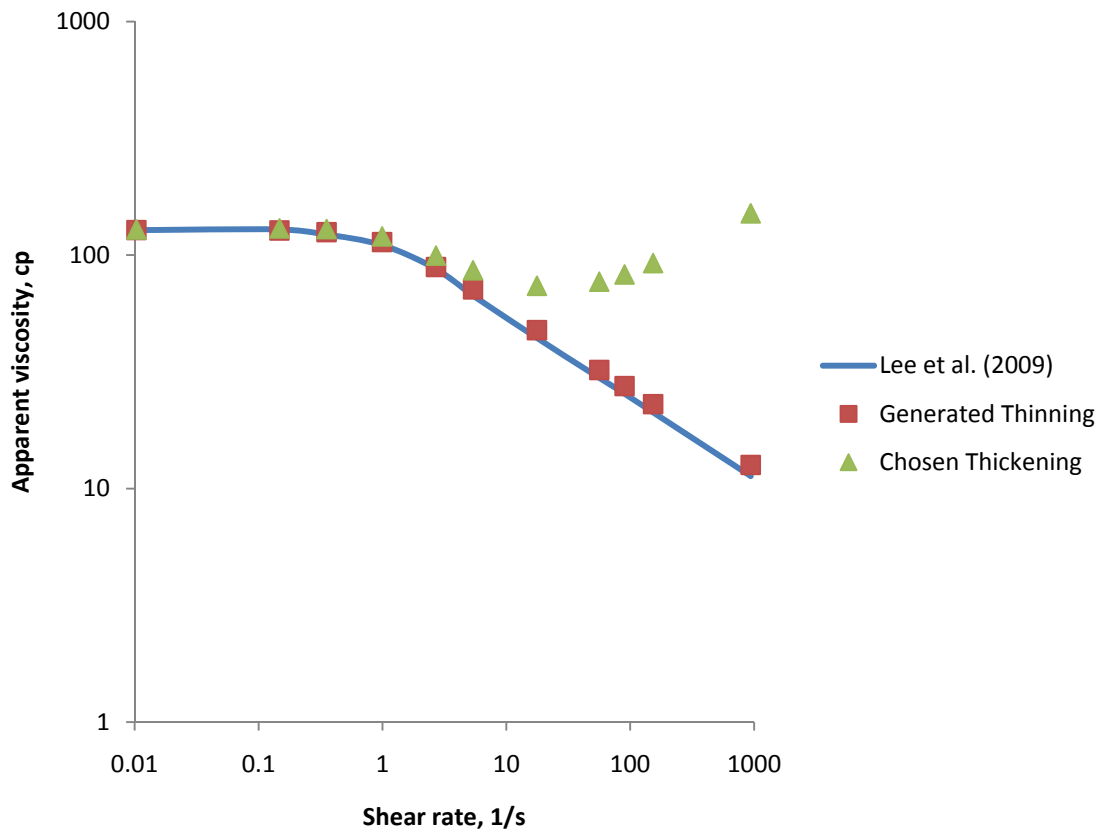


Figure 3.10: Rheological data for the 3000 ppm polymer from Figure 1 of Lee et al. (2009).

Tests of single-well segments were performed to determine appropriate modifications to properly account for non-Newtonian flow. The test plan, designed to test different pressures and reservoir permeabilities, and many of the results can be seen in Appendix C. An entire well was also simulated to determine the total axial pressure drop along a well and will be discussed later.

The apparent viscosity in both the well and the reservoir varies with radial distance because the velocity varies with radial distance. As a result, the best apparent viscosity values for both  $C_{L\_new}$  and the viscosity ratio shown in Equation 3.6 needed to be determined. Three different values were tested: the maximum, minimum and average.

The minimum apparent well and reservoir viscosities occur at  $r = R_w$ . The maximum apparent well viscosity occurs at  $r = 0$ , while the maximum apparent reservoir viscosity occurs at  $r = R_e$  because the lowest velocity in the porous media occurs at the farthest radial distance.

Figure 3.11 and Figure 3.12 illustrate the benefit of including the proposed viscosity ratio in the conductivity equation (Equation 3.6) and the apparent well viscosity in  $C_{L\_new}$  (Equation 3.7) for Test 4 as listed in Table C.1. Figure 3.11 employs Equation 1.5 for  $\gamma^*$ , Equation 3.8 (minimum viscosity), Equation 3.9 (maximum viscosity), and Equation 3.10 (average viscosity) for  $C_{L\_new}$  ( $C_{L\_seg}$  in Equation 3.4 for  $P^*$ ).

$$C_{L\_new} = \frac{R_w(P_o - p_T)\sqrt{\gamma^*}}{2\mu_{well}|_{@R=R_w}V_m^o} \quad (3.8)$$

$$C_{L\_new} = \frac{R_w(P_o - p_T)\sqrt{\gamma^*}}{2\mu_{well}|_{@R=0}V_m^o} \quad (3.9)$$

$$C_{L\_new} = \frac{R_w(P_o - p_T)\sqrt{\gamma^*}}{2\bar{\mu}_{well}V_m^o} \quad (3.10)$$

Figure 3.12 uses Equation 3.6 for  $\gamma^*$  and Equation 3.11 (minimum viscosity), Equation 3.12 (maximum viscosity), and Equation 3.13 (average viscosity).

$$\gamma^*_{new} = \frac{k}{R_w t} \frac{\mu_{well}}{\mu_{res}} \Big|_{@r=R_w}, \quad C_{L\_new} = \frac{R_w(P_o - p_T)\sqrt{\gamma^*_{new}}}{2\mu_{well}|_{@r=R_w}V_m^o} \quad (3.11)$$

$$\gamma^*_{new} = \frac{k}{R_w t} \frac{\mu_{well}|_{@r=0}}{\mu_{res}|_{@r=R_e}}, \quad C_{L\_new} = \frac{R_w(P_o - p_T)\sqrt{\gamma^*_{new}}}{2\mu_{well}|_{@r=0}V_m^o} \quad (3.12)$$

$$\gamma^*_{new} = \frac{k}{R_w t} \frac{\bar{\mu}_{well}}{\bar{\mu}_{res}}, \quad C_{L\_new} = \frac{R_w(P_o - p_T)\sqrt{\gamma^*_{new}}}{2\bar{\mu}_{well}V_m^o} \quad (3.13)$$

The Newtonian value in Figure 3.11 and Figure 3.12 corresponds to the original pressure equation, Equation 1.4, which uses Equation 1.5 for  $\gamma^*$  and Equation 1.6 for  $C_L$  where  $\mu_o$  was a constant 128 cp.

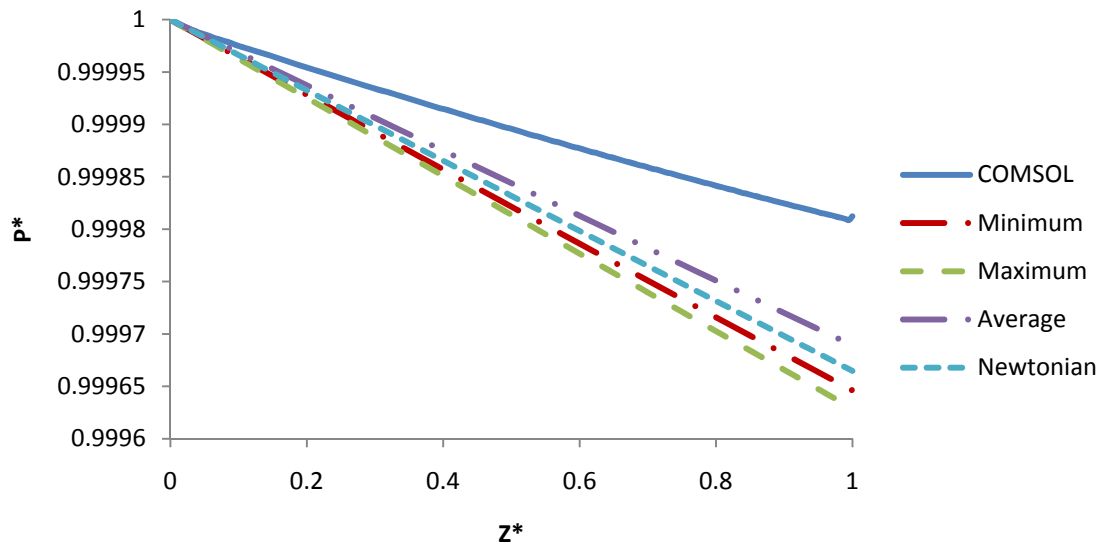


Figure 3.11: Pressure matches using different apparent viscosity concepts for Test 4 in Table C.1 without the modified  $\gamma^*$ .

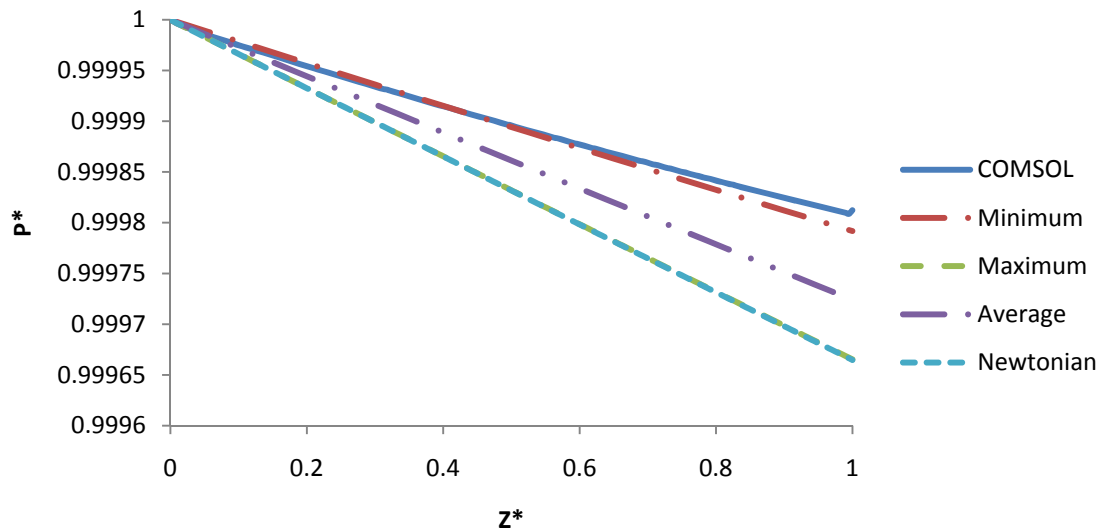


Figure 3.12: Pressure matches using different apparent viscosity concepts for Test 4 in Table C.1 with the modified  $\gamma^*$ .

In Figure 3.11, no viscosity value results in a good fit with the COMSOL solution. However, if  $\gamma^*_{new}$  is used rather than simply  $\gamma^*$ , the minimum viscosity results in

a very good match. The maximum viscosity results in the Newtonian solution because at sufficiently low shear rates, the viscosity becomes  $\mu_0$ , the same viscosity used in the Newtonian solution. More test results can be seen in Appendix C.

The Newtonian solution should result in a larger pressure drop than the shear-thinning solution because a shear-thinning fluid is less viscous. Two complete wells, whose properties are listed in Table 3.1, were modeled and compared. The only difference between the two cases was that one fluid was shear-thinning, using the properties found in Table 3.2, and the other was Newtonian,  $\mu_0$  of Table 3.2. The outlet pressure,  $p_T$ , was set to create equal leakage rates, 16.67 STB/D/m, at the toe of the well. Figure 3.13 compares the COMSOL axial pressure along the well (the toe of the well is located at 1,500 meters) to Equation 3.11, with  $\gamma^*_{new}$  and  $C_{L\_new}$ .

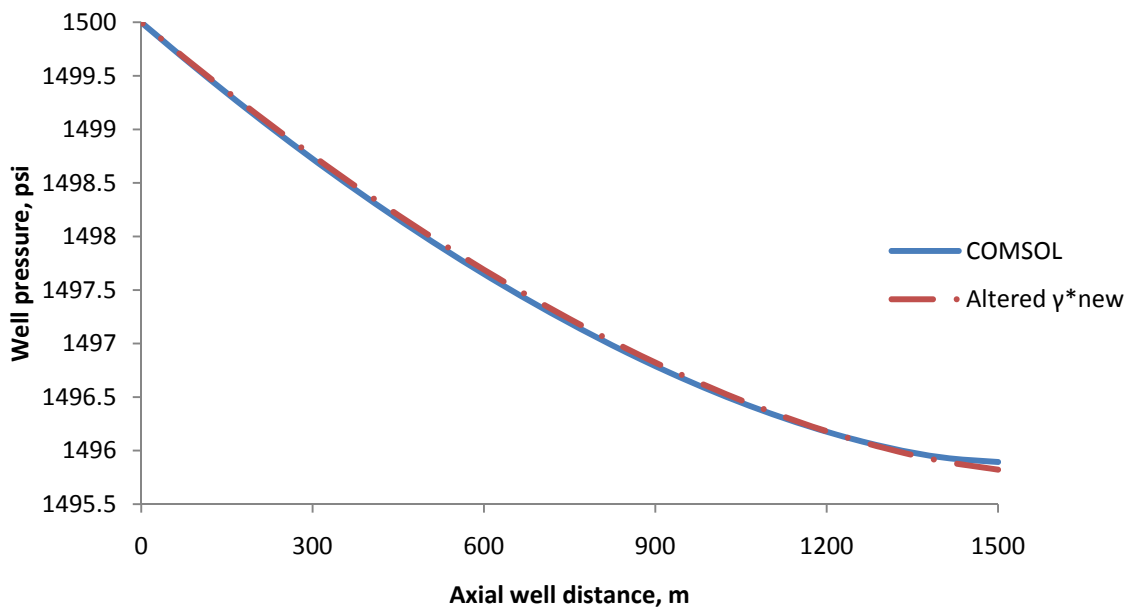


Figure 3.13: Axial well pressure comparison of COMSOL to Equation 1.4 (Equation 3.11 being used to calculate  $\gamma^*_{new}$  and  $C_{L\_new}$ ) for both the Newtonian and shear-thinning fluids with for the well-reservoir domains listed in Table 3.1.

Figure 3.13 illustrates the excellent axial pressure profile agreement for the non-Newtonian fluid. The error for the total axial pressure drop was 1.7%. For this particular case, the unaltered  $\gamma^*$  resulted in an error of 2.3%.

### **3.3 SHEAR-THICKENING**

HPAM can exhibit viscoelastic effects resulting in shear thickening behavior at high shear rates in porous media. The Unified Viscosity Model (Equation 1.9) proposed by Delshad et al. (2008) captures shear-thinning and thickening behavior (Figure 3.10). Based on the results of the thinning test given above, the apparent viscosity at  $r = R_w$  for both the well and reservoir was used. The test plan for shear-thinning fluids (Table C.1) was also used for the viscoelastic fluids. However, the viscoelastic effects in the porous media caused the injection pressures to be increased for the 100 md cases to 4000 psi for  $R_w = 0.5$  ft and 6000 psi for  $R_w = 0.25$  ft. Figure 3.14 and Figure 3.15 are also from Test 4 of Table C.1 for the viscoelastic rheology, shear-thickening properties of Table 3.2, with other tests appearing in Appendix C.

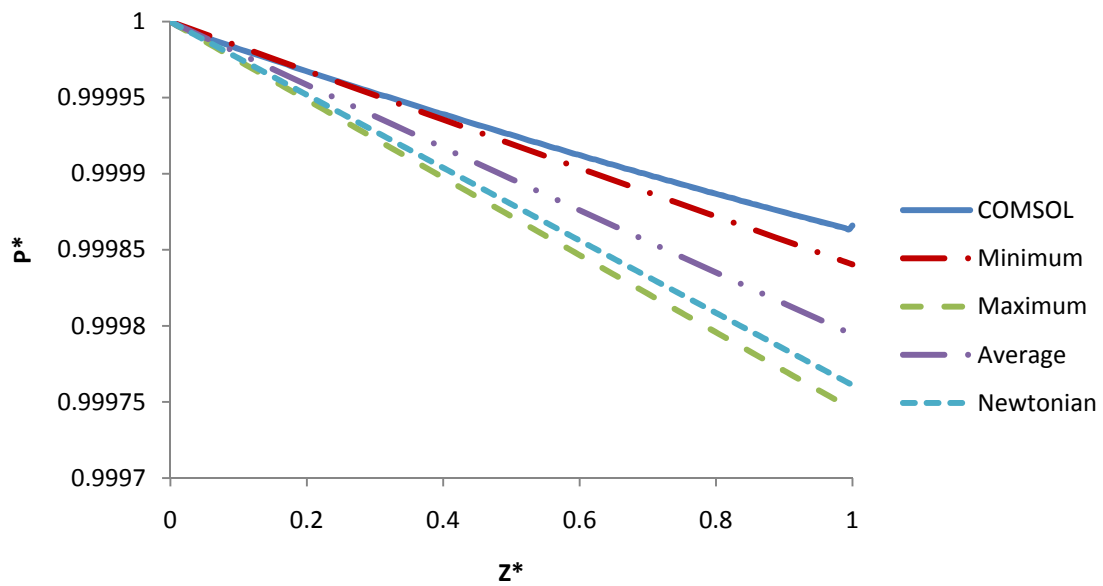


Figure 3.14: Pressure matches using different apparent viscosity concepts of viscoelastic fluids for Test 4 in Table C.1 without the modified  $\gamma^*$ .

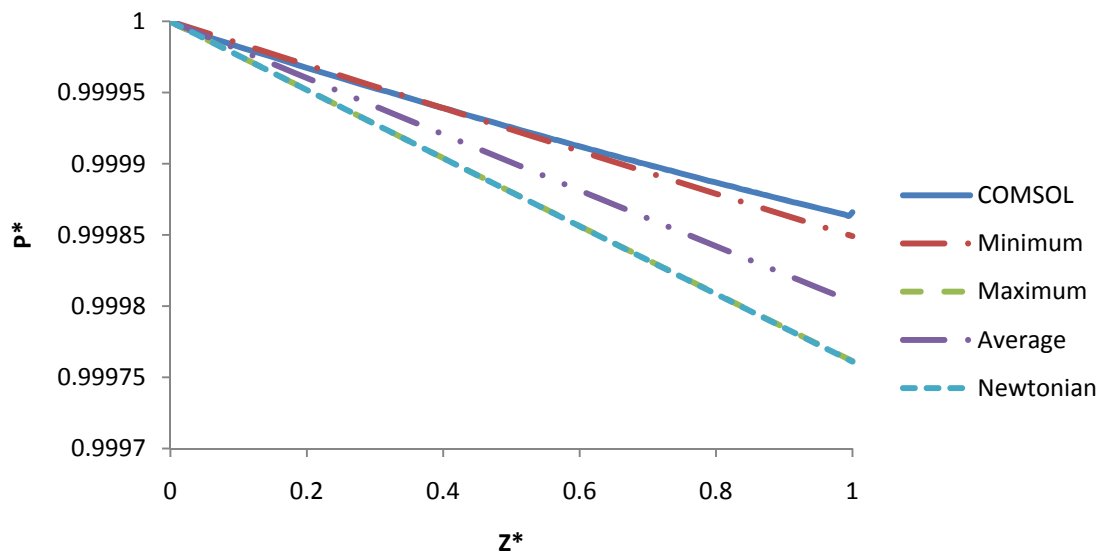


Figure 3.15: Pressure matches using different apparent viscosity concepts of viscoelastic fluids for Test 4 in Table C.1 with the modified  $\gamma^*$ .

The results were very similar to the shear-thinning results in Figures 3.11 and 3.12 with  $\gamma^*_{\text{new}}$  improving the agreement; however, the improvement was not as evident as in the shear-thinning results. The apparent viscosity in the reservoir was significantly closer to the well apparent viscosity because of thickening; therefore, the viscosity ratio is closer to unity, reducing the importance of the correction. The viscosity ratio will not always approach unity because at  $r = R_w$  the apparent reservoir viscosity can greatly exceed the apparent well viscosity. In this instance,  $\gamma^*_{\text{new}}$  still yielded a more accurate result. Figure 3.16 illustrates the better agreement by using  $\gamma^*_{\text{new}}$  for Test 5 when  $\mu_{\text{res}}|_{r=R_w} = 84$  cp and  $\mu_{\text{well}}|_{r=R_w} = 26$  cp.

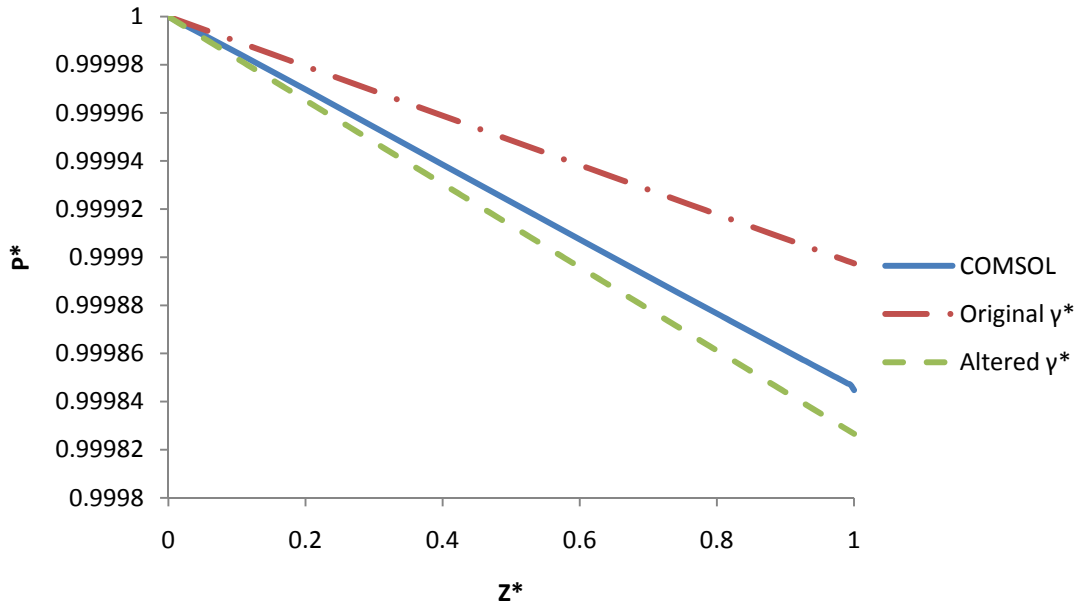


Figure 3.16: Pressure matches using  $\gamma^*_{\text{new}}$  when the apparent reservoir viscosity greatly exceeds the apparent well viscosity.

A full well with properties as those listed in Table 3.1 was modeled with a viscoelastic fluid. The shear rates peaked at approximately 90 1/s resulting in a 55 cp increase, 27 cp to 82 cp, from the shear-thinning fluid at  $r = R_w$  in the porous media.



Despite the large reservoir apparent viscosity difference, the leakage rate and well pressure drop difference appears negligible compared to the shear-thinning case. Figure 3.17 and Figure 3.18 compare the axial pressure drop and the leakage rate along the well for the shear-thickening (UVM) and shear-thinning (Carreau) cases compared to the Newtonian case.

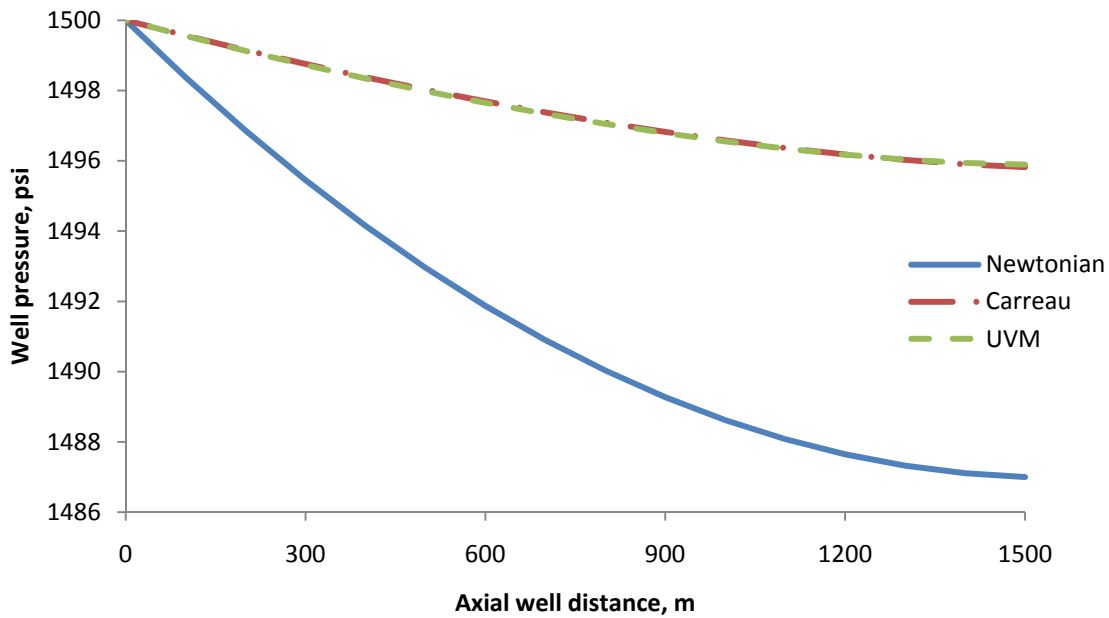


Figure 3.17: Axial well pressure using COMSOL for both the viscoelastic (UVM) and shear-thinning (Carreau) fluids compared to the Newtonian case for the well-reservoir domains listed in Table 3.1 and Table 3.2.

Figure 3.17 clearly shows that the Newtonian fluid results in a significantly larger pressure drop than the Carreau fluid for very similar flow rates. In fact, the pressure drop is approximately three times as large for this particular case. The result is not surprising because the thinning nature of polymers in wellbores provides injection benefits (Lake, 1989).

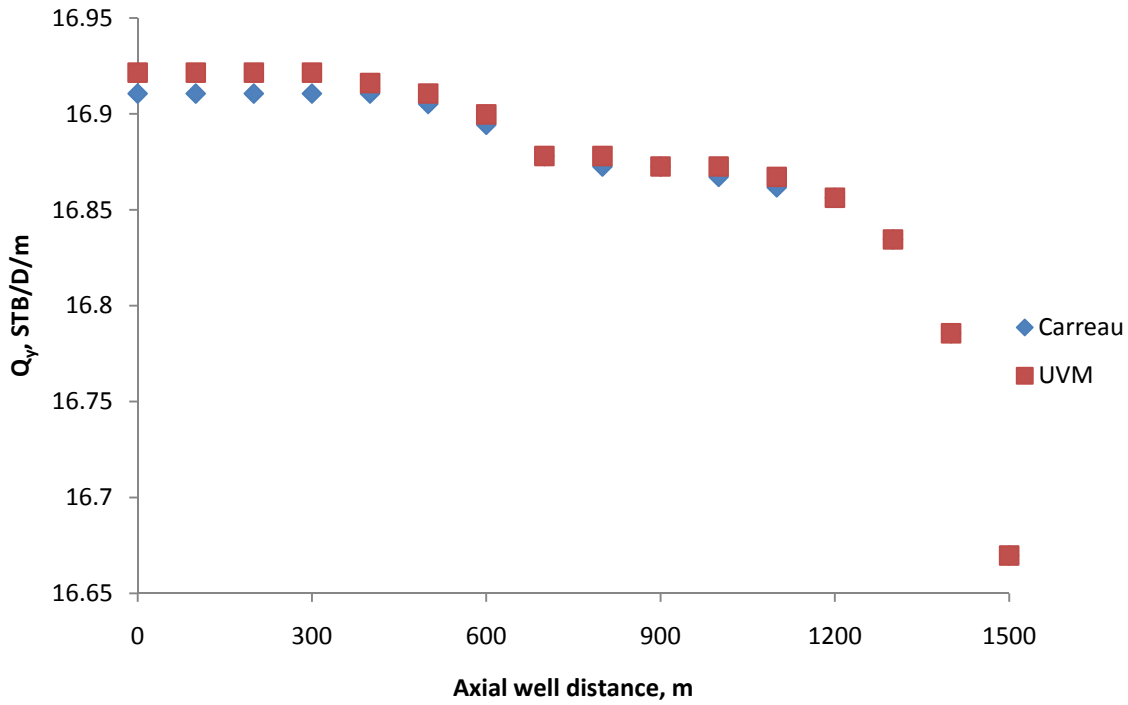


Figure 3.18: Leakage rates for both the viscoelastic (UVM) and shear-thinning (Carreau) fluids for the well-reservoir domains listed in Table 3.1 and Table 3.2.

The injection profile similarities are surprising because the reservoir apparent viscosity is significantly higher for the shear-thickening case than for the shear-thinning case. However, the leakage profile was created by significantly increasing the outlet pressure to create a 16.67 STB/D/m rate at the toe. The shear-thinning case had an outlet pressure of 1221 psi for a drawdown of 279 psi. The shear-thickening case had an outlet pressure of 1101 psi for a drawdown of 399 psi. The equivalent axial pressure drop implies the well viscosity is the dominant value when determining the pressure drop because the wellbore viscosities are equal for both cases. The viscoelastic effects in the reservoir do not appear to result in a pressure variation in the well; however, the viscoelastic effects do dramatically impact injection rates because an extra 120 psi was required to inject the polymer at the same leakage rate.

### **3.4 RELEVANT AXIAL PRESSURE DROPS**

Ozkan et al. (1995) discusses the importance of including pressure drop in production wells. When the pressure differential between the horizontal well and the reservoir is small, the pressure losses in the horizontal well can dramatically impact production. The process currently being examined is the reverse of the Ozkan et al. (1995) problem. The pressure drop will not reduce the fluid entering the wellbore; the pressure drop will result in an uneven injection profile. The question of relevance is a critical topic. When is the pressure drop sufficiently large to impact recovery? The magnitude of the pressure drop will be discussed in this chapter with the resulting impact on recovery to be discussed in Chapter 4 with the finite difference simulator implementation.

Four different injection rates, 10,000 STB/D, 20,000 STB/D, 30,000 STB/D, and 40,000 STB/D, four different fluid viscosities, 10 cp, 100 cp, 200 cp, and 300 cp, along with three different well lengths, 600 m, 1,600 m, and 3,000 m were tested with the properties given in Table B.1.

Only Newtonian fluids were simulated because a full set of polymer data was not available. Kim et al. (2010) have very recently created a database for EOR polymers that may be sufficient to run a similar series of tests including viscoelastic effects. Figure 3.19 illustrates the pressure drop for the four different viscosities for a 600 meter well.

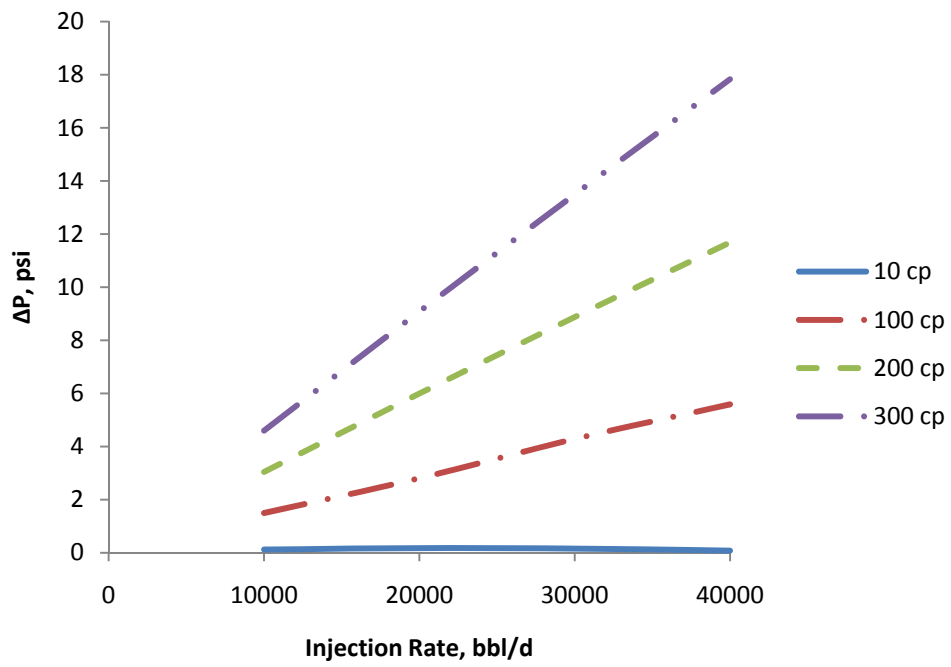


Figure 3.19: Pressure drop correlation for 10 cp, 100 cp, 200 cp, and 300 cp Newtonian fluids in a 600 meter well as a function of injection rate.

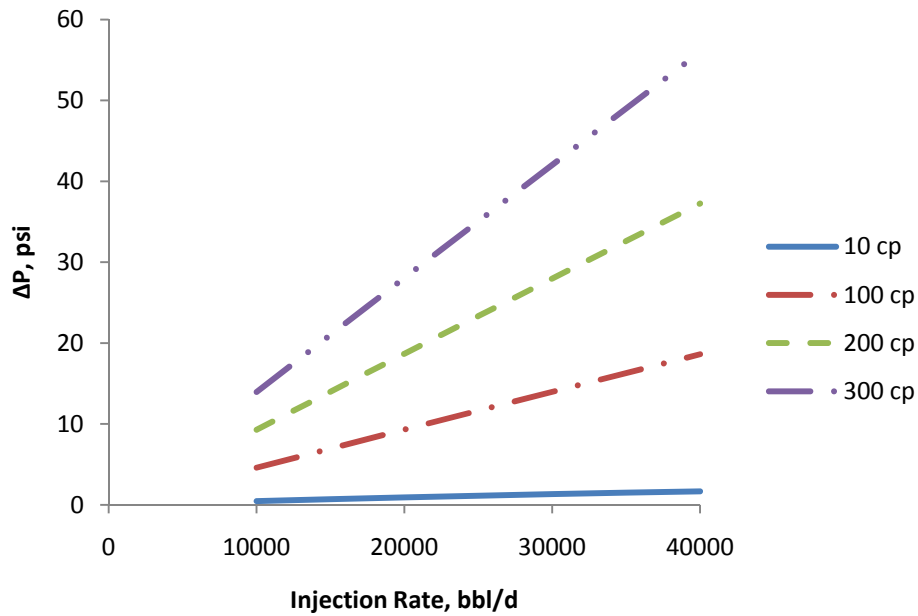


Figure 3.20: Pressure drop correlation for 10 cp, 100 cp, 200 cp, and 300 cp Newtonian fluids in a 1,800 meter well as a function of injection rate.

Despite the inclusion of leakage, the axial pressure drop for Newtonian fluids appears to be a linear function of injection rate with the 300 cp fluid resulting in a pressure drop of 18 psi at 40,000 STB/D. The pressure drop is also a strong function of well length as a well that is three times as long produces a pressure drop that is approximately three times as large as seen by Figure 3.20 for an 1,800 meter well. This is reasonable because the Hagen-Poiseuille equation (Bird et al., 2007), Equation 3.1, results in a linear pressure drop as a function of length.

### 3.5 INCLUSIVE PRESSURE EQUATION (IPE)

The non-Newtonian corrections are applicable for Newtonian fluids as well. A Newtonian fluid has a constant viscosity; therefore, the viscosity ratio of  $\mu_{\text{well}}/\mu_{\text{res}}$  in Equation 3.11 for  $\gamma^*_{\text{new}}$  equals 1. Also, the apparent viscosity value in Equation 3.11 for

$C_{L\_new}$  is a constant value. As a result of the simplifications, Equation 3.14 reduces to Equation 3.4. Equation 3.14 presents the Inclusive Pressure Equation (IPE).

$$P^* = \left\{ 1 + 2\gamma^*_{new} - 4\gamma^*_{new} \left( \frac{r}{R_w} \right)^2 \right\} \left[ \cosh \left( 4\sqrt{\gamma^*_{new}} \frac{z}{R_w} \right) - \frac{1}{C_{L\_new}} \sinh \left( 4\sqrt{\gamma^*_{new}} \frac{z}{R_w} \right) \right] \quad (3.14)$$

The new  $C_{L\_new}$  and  $\gamma^*$ , Equation 3.11, are presented again below.

$$\gamma^*_{new} = \frac{k}{R_w t} \frac{\mu_{well}}{\mu_{res}} \Big|_{@r=R_w}, \quad C_{L\_new} = \frac{R_w (P_o - P_T) \sqrt{\gamma^*_{new}}}{2\mu_{well} \Big|_{@R=R_w} V_m^o} \quad (3.11)$$

No change to the IPE is required for any fluid type as the only changes from the Newtonian equation, Equation 3.4, involve properly accounting for viscosity changes resulting from shear. Shear-thinning fluids require the use of Equation 1.8 (UVM) while shear-thinning fluids require the use of Equation 3.5. Therefore, the IPE is applicable for Newtonian, shear-thinning, and shear-thickening fluids for any well radius and reservoir permeability.

## **Chapter 4: IMPLEMENTATION IN UTCHEM**

Most reservoir simulators do not currently account for pressure drop in a horizontal well. UTCHEM is no different. UTCHEM, the University of Texas Chemical Compositional Simulator, is a three-dimensional, multiphase, multi-component, compositional, variable temperature, finite-difference numerical simulator. The simulator uses cell-centered pressures, harmonic mean for transmissibility, and a linear extrapolation for boundary cells. It has been continually expanded since its inception in 1978 to include many chemical and biological phenomena in porous media. It has been validated against numerous EOR experiments to insure its accuracy.

Wells are given one of two constraints: pressure or rate. The pressure constraint for horizontal wells creates a constant pressure along the entire completed length; therefore, the Inclusive Pressure Equation developed in Chapter 3 was needed to account for the pressure drop.

A series of tests, Table D.1, were run to determine the impact of the axial pressure drop resulting from the injection of highly viscous fluids (all tests used the UVM for the porous media for the HPAM described in Table 3.2). Injection differences are examined and the impact on oil recovery is reported. The commonly-applied assumption of uniform pressure is used as the benchmark to determine the importance of including axial pressure drop in wellbores.

### **4.1 IMPLEMENTATION**

The implementation of the IPE was straightforward. The proposed calculations for  $\gamma^*_{\text{new}}$  and  $C_{L\_new}$  (Equation 3.11) and the IPE (Equation 3.14), are given below.

$$\gamma_{new}^* = \frac{k}{R_w t} \frac{\mu_{well}}{\mu_{res}} \Big|_{@r=R_w}, \quad C_{L\_new} = \frac{R_w (P_o - p_T) \sqrt{\gamma_{new}^*}}{2 \mu_{well} \Big|_{@r=R_w} V_m^o} \quad (3.11)$$

$$P^* = \left\{ 1 + 2\gamma_{new}^* - 4\gamma_{new}^* \left( \frac{r}{R_w} \right)^2 \right\} \left[ \cosh \left( 4\sqrt{\gamma_{new}^*} \frac{z}{R_w} \right) - \frac{1}{C_{L\_new}} \sinh \left( 4\sqrt{\gamma_{new}^*} \frac{z}{R_w} \right) \right] \quad (3.14)$$

#### 4.1.1 Conductivity Equation

For the conductivity equation in Equation 3.11, the reservoir permeability,  $k$ , is known for each grid block in the simulator. The well radius,  $R_w$ , is set in the input file. The thickness value,  $t$ , in Equation 3.11 at which the constant pressure outlet was assigned was taken to be the Peaceman effective radius of the well (Peaceman, 1983), Equation 4.1, which was calculated for all completed well blocks.

$$r_o = 0.28 \frac{\left[ \left( \frac{k_x}{k_y} \right)^{1/2} \Delta x^2 + \left( \frac{k_y}{k_x} \right)^{1/2} \Delta y^2 \right]^{1/2}}{\left( \frac{k_x}{k_y} \right)^{1/4} + \left( \frac{k_y}{k_x} \right)^{1/4}} \quad (4.1)$$

The non-Newtonian viscosities in Equation 3.11 include the empirical constants,  $\mu_o$ ,  $\mu_\infty$ ,  $\mu_{max}$ ,  $n_1$ ,  $n_2$ ,  $\lambda_1$ ,  $\lambda_2$ ,  $\alpha$ ,  $\tau_f$ ,  $\kappa$ ,  $k_{rw}$ ,  $S_w$ , and  $\phi$  found using Equation 1.7, Equation 1.8 and Equation 1.9 were all specified in the input file. Therefore, the wellbore apparent viscosity, Equation 1.7, simply required the effective shear rate.

$$\mu_{well} = \mu_\infty + (\mu_o - \mu_\infty) \left( 1 + (\lambda_1 \dot{\gamma}_{w\_eff})^\alpha \right)^{(n_1-1)/\alpha} \quad (1.7)$$

Shear rate at the wall of a pipe for a power-law fluid is given in Equation 4.2 (Lake, 1989).

$$\dot{\gamma}_{w\_eff} = \frac{4V_m^o}{R_w} \quad (4.2)$$



The mean average velocity,  $V_m^o$ , per well block was known by adding the leakage rates of all well blocks further along the well from the previous time step, a variable within UTCHEM, to create a total well axial volumetric flux. Then the axial volumetric flux in each well block was divided by the well cross-sectional area to yield a mean average velocity.

The reservoir apparent viscosity given in Equation 1.8 requires only the effective shear rate in porous media, Equation 1.9.

$$\mu_{res} = \mu_{\infty} + (\mu_o - \mu_{\infty}) \left(1 + (\lambda_1 \dot{\gamma}_{eff})^{\alpha}\right)^{(n_1-1)/\alpha} + \mu_{max} \left(1 - e^{-\{(\tau_r \lambda_2 \dot{\gamma}_{eff})^{n_2-1}\}}\right) \quad (1.8)$$

$$\dot{\gamma}_{eff} = \kappa \left[ \frac{3n_1 + 1}{4n_1} \right]^{n_1/n_1-1} \left[ \frac{u_w}{\sqrt{k k_{rw} S_w \phi}} \right] \quad (1.9)$$

The only unknowns are  $u_w$ ,  $k_{rw}$ , and  $S_w$  and they were all calculated at  $r = R_w$ . The water saturation,  $S_w$ , was taken to be  $1-S_{or}$ . Finite-difference simulators give discrete values for all variables in all blocks. Therefore, any saturation value in the block is the saturation of the entire block. However, the entire block saturation is not relevant for this calculation, only the saturation directly affecting the velocity for the effective shear rate calculation. The well-reservoir interface should have the highest water saturation of any location because it is the injection point (i.e., all polymer must pass through the well-reservoir interface and heterogeneity should have little impact). The relative permeability was taken to be the end-point value which is also specified in the input file. The end-point was used because saturation was evaluated as the end point saturation,  $1-S_{or}$ . The Darcy velocity,  $u_w$ , was calculated by dividing the leakage rate of the given block from the previous time step by the perpendicular area of the well, calculated in Equation 4.3 where  $\Delta z$  is the grid block length.

$$Area = 2\pi R_w \Delta z \quad (4.3)$$

### **4.1.2 $C_L$ Equation**

The pressure drawdown of Equation 3.11,  $P_o - p_T$ , was calculated using the well's flowing pressure of the previous time step minus the grid block pressure of the previous time step. The conductivity equation was described above along with the apparent well viscosity. The only unknown was the mean velocity but that can be calculated as described in the previous section.

### **4.1.3 IPE**

All of the values in the IPE are known values or calculated above with the exception of the axial well length coordinate,  $z$ . The axial length was taken to be the grid block length. Therefore, the initial pressure,  $P_o$ , is the pressure value from the end of the previous grid block. The entire altered code with a more detailed explanation can be found in Appendix D.

## **4.2 MODEL CREATION AND TESTING PLAN**

The reservoir, well, and grid data are given in Table 4.1. Two reservoirs, a homogeneous reservoir with a permeability of 1 D and a heterogeneous reservoir with permeability geometric mean of 1 D and a Dykstra Parsons coefficient of 0.8 (Sahni et al., 2005), were created for testing. The 1 D value was intended to represent a highly permeable sand reservoir. Figure 4.1 depicts the reservoirs with one injector and one producer. The wells were 4500 feet long with 2000 feet between them.

Table 4.1: Reservoir, well, and grid properties for the UTCHEM model illustrated in Figure 4.1.

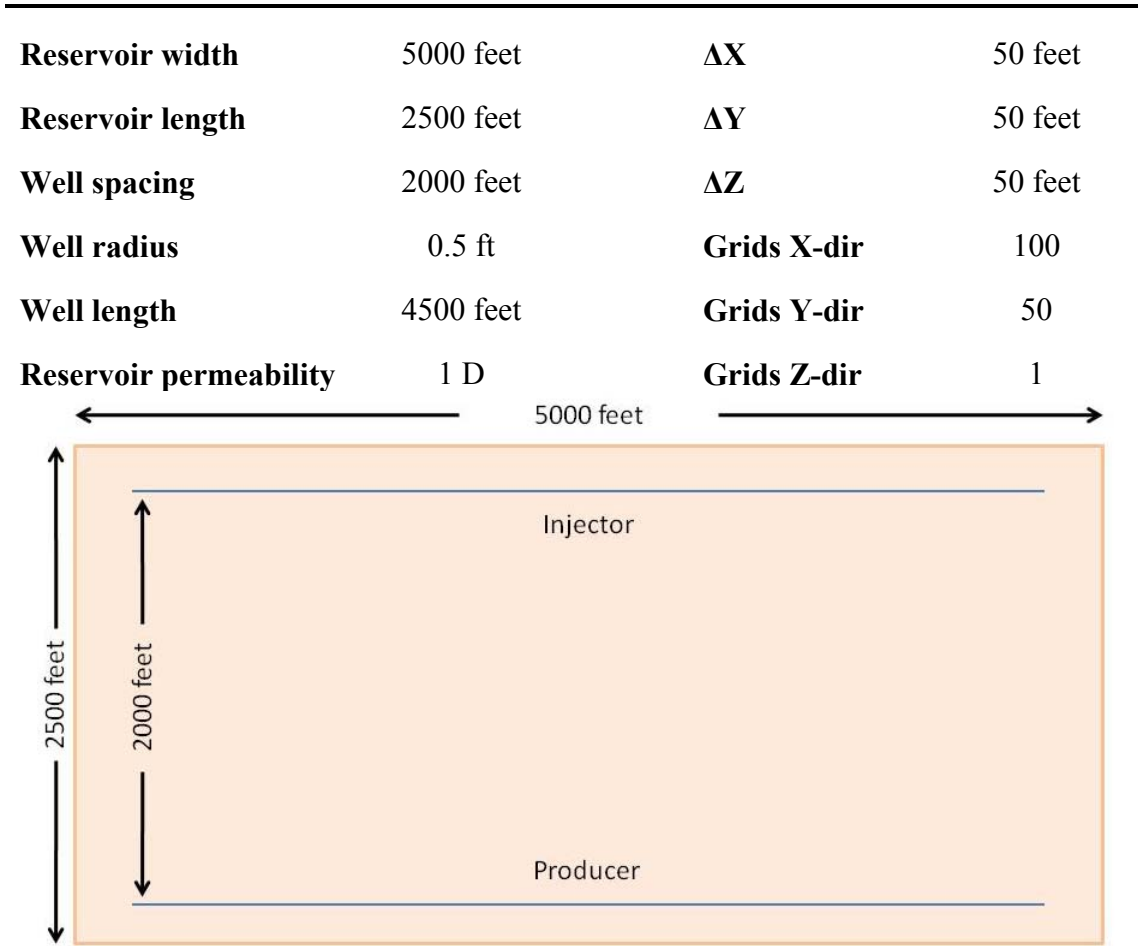


Figure 4.1: Physical dimensions and orientation of the UTCHEM model for implementation of the IPE.

Huh and Pope (2008) discuss residual oil saturation reduction is achievable by initially using polymer floods rather than waterfloods. The reservoirs were directly flooded with a polymer, once with uniform pressure and once including the IPE for fourteen different tests, nine with a homogeneous reservoir and five with a heterogeneous

reservoir. The testing plan is listed in Table D.1. Injection rates were controlled by creating large or small pressure gradients between the two wells and the reservoir.

### 4.3 HOMOGENEOUS RESERVOIRS

#### 4.3.1 Recovery Difference

The nine tests conducted for homogeneous reservoirs yielded a maximum recovery loss of 10.5% after 10 days but that same test recorded a 0.89% recovery loss after 1000 days. No appreciable difference in oil production occurred when using the IPE rather than the traditional assumption of uniform pressure along the well for any test at later times. At very early times, injection discrepancies occurred and are demonstrated in Figure 4.2 by plotting the water saturation values of the well grid blocks for Test 5 at 0.5 days and 50 days (Figure 4.3).

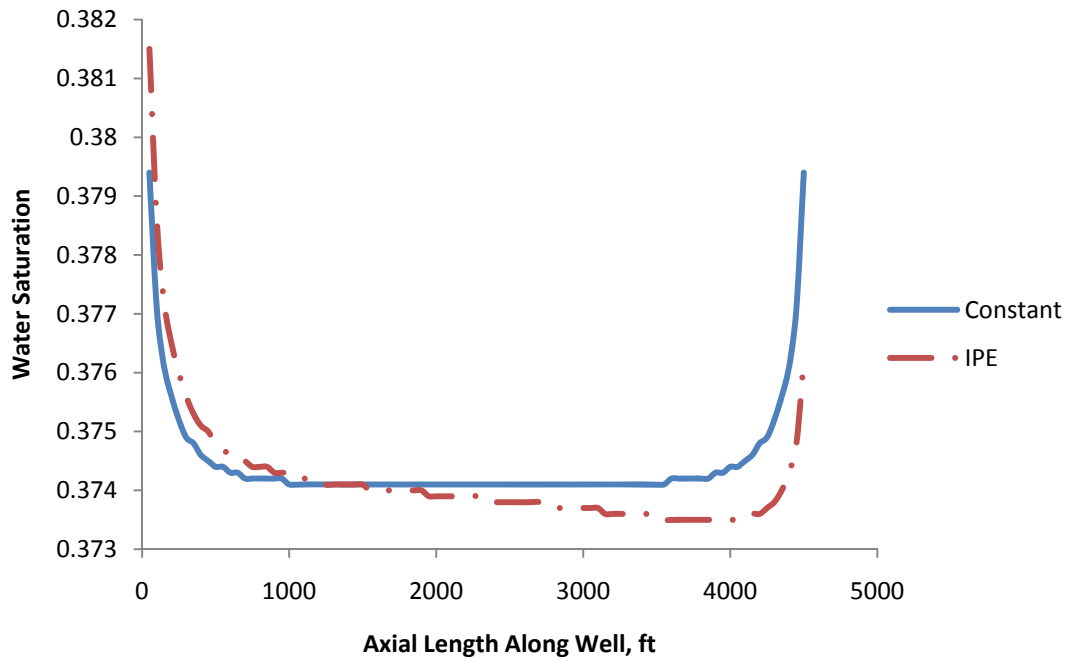


Figure 4.2: Injection discrepancies at 0.5 days between the IPE and a constant pressure assumption for Test 5 from Table D.1.

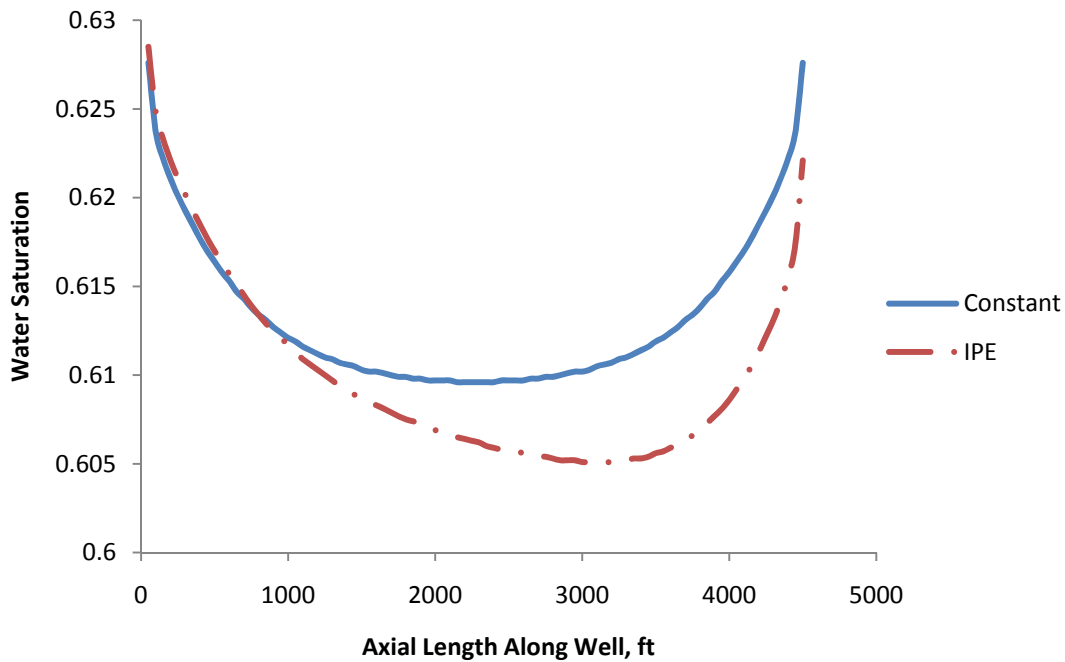


Figure 4.3: Injection discrepancies at 50 days between the IPE and a constant pressure assumption for Test 5 from Table D.1.

The U-shaped injection profile is consistent with many other studies regarding injection patterns (Jelmert and Thompson (1991); Vicente et al. (2004,)); however, a clear, albeit, small difference in water saturation can be seen at 4000 feet. The water saturation values given in Figure 4.2 demonstrate a slight reduction in injection toward the toe of the well (4500 ft). An injection discrepancy occurred at the heel of the well at 0.5 days indicating a shift in injection toward the heel and away from the toe. The oil recovery difference at 0.5 days was 4,709 barrels or 10.5%.

However, the injection profile of Figure 4.2 shifted more toward the toe of the well in Figure 4.3; however, it was still small (less than 0.1). The water saturation profiles of Test 5 in Table D.1 at 1000 days can be seen in Figure 4.4. There is no discernable difference between the two floods, while the constant pressure assumption

does produce 15,100 BBL more (only 0.89% difference). More recovery loss results can be found in Appendix D.

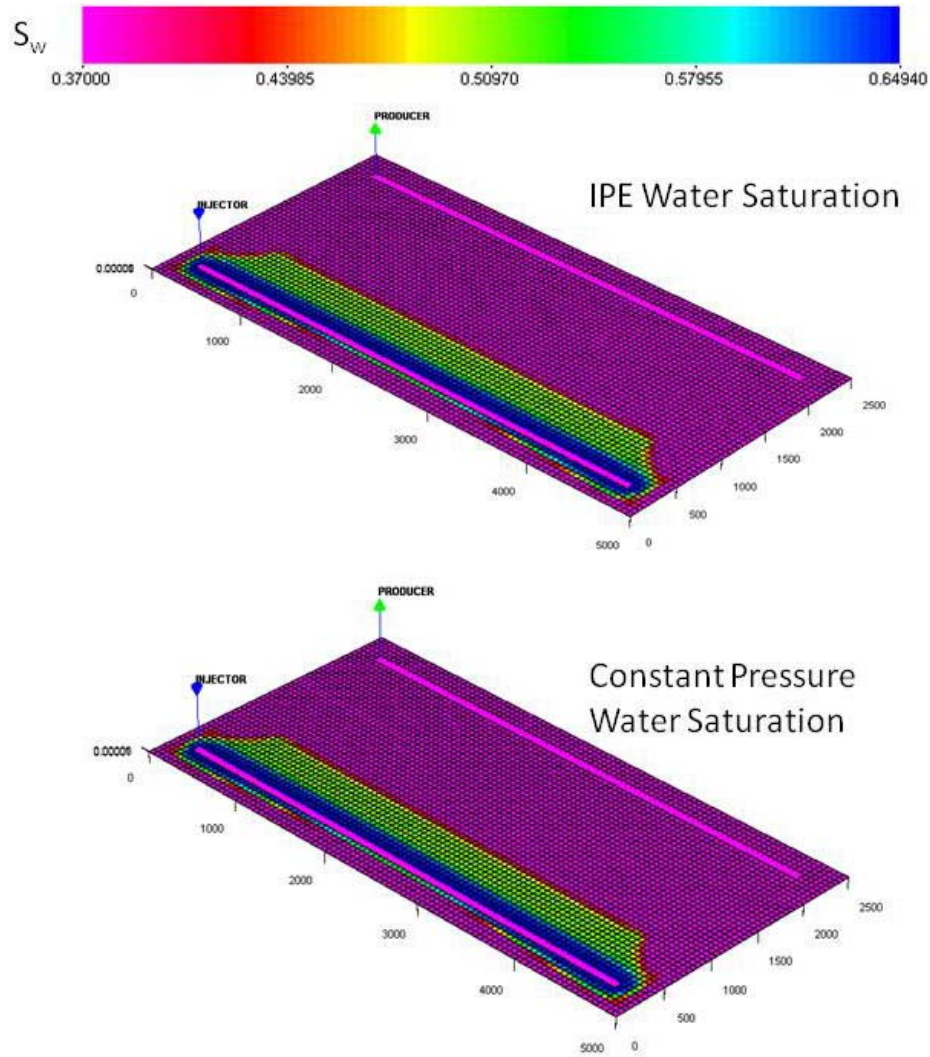


Figure 4.4: Water saturation profiles of Test 5 in Table D.1 for the IPE (top) and the constant pressure assumption (bottom) at 1000 days.

Figure 4.6 plots the cumulative lost recovery as a function of time while Figure 4.7 plots the same data as a function of percent recovery loss.

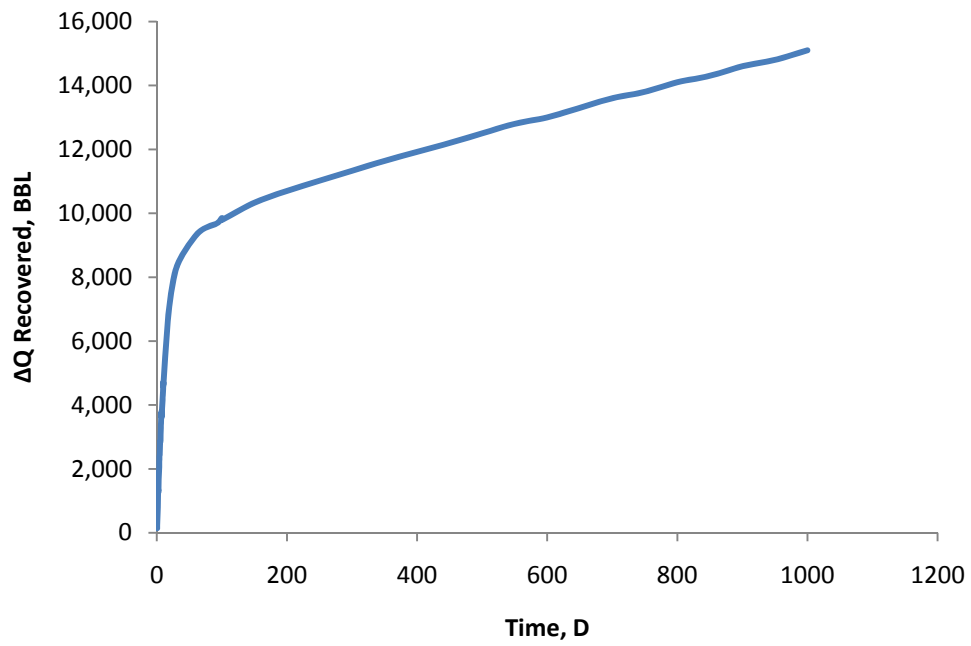


Figure 4.6: Cumulative lost recovery as a function of time for Test 5 of Table D.1.

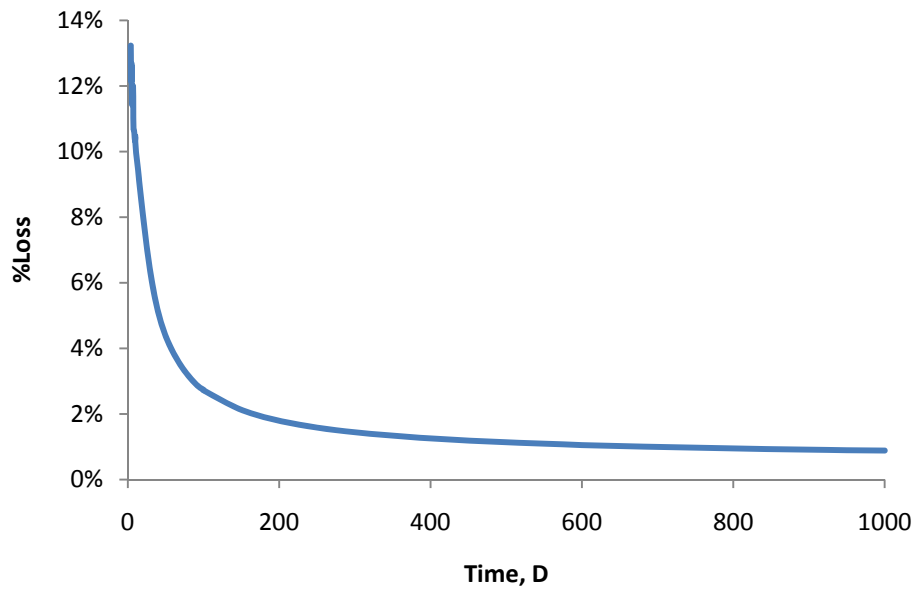


Figure 4.7: Percent recovery loss in recovery using Equation 4.4 as a function of time for Test 5 of Table D.1.

$$\%Loss = \frac{(CUM_{Constant} - CUM_{IPE})}{CUM_{IPE}} \quad (4.4)$$

The absolute value of lost oil recovery continues to grow with time; the percent recovery loss, Equation 4.4, continues to drop. The slope of the  $\Delta Q_{Recovered}$  changes sharply around 50 days and it was believed to occur because the axial pressure profile becomes more uniform.

### 4.3.2 Axial Pressure Profile

The well axial pressure profiles at 0.5 days show a 25 psi drop for Test 5. However, at 50 days the axial pressure drop was only 5 psi. Figure 4.5 illustrates the pressure becoming more uniform as a function of time.

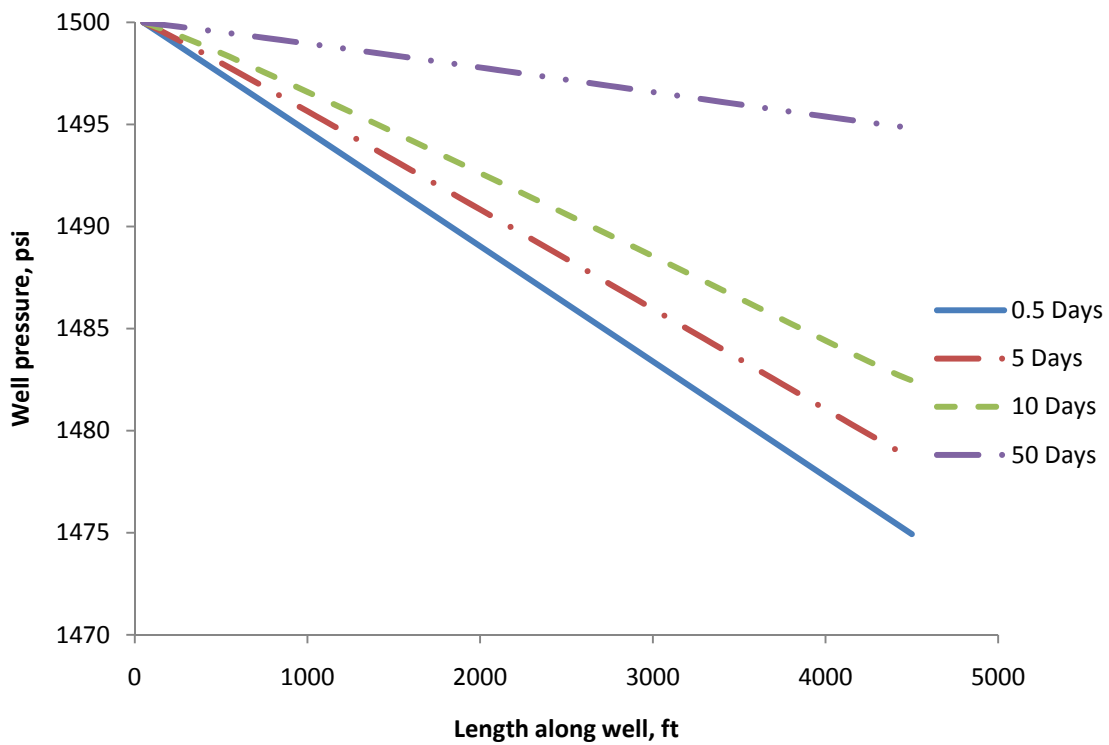


Figure 4.5: Axial well pressure profiles for Test 5 of Table D.1.



The reduction of axial pressure drop with time is apparent in the cumulative recovery difference with time. The sharp turn in Figure 4.6 occurs around 50 days which corresponds to the 5 psi drop in Figure 4.4. The movement of the pressure profile from 0.5 days to 50 days in Figure 4.4 corresponds perfectly to the steep incline of recovery loss prior to 50 days in Figure 4.6. The reason for this behavior is not clear and as a result it is unclear whether this actually occurs in the field. Further study regarding this phenomenon is warranted. A closer inspection of the leveling off effect needs to be undertaken to determine whether it actually occurs in real applications. If it does not, Figure 4.6 and Figure 4.7 appear to indicate that a significant portion of oil, far more than UTCHEM is calculating, could be lost to recovery because of axial pressure drop when the drawdown is small.

The linear appearance of the axial pressure profile results (at least partially) from a homogeneous reservoir (heterogeneity produces a different profile and is discussed later in this chapter) and a high injection rate of more than 20,000 BBL/D. A low flow test was conducted; however, a near linear profile still occurred. Further examination may be required to ascertain the reason for the linear shape when the equation is non-linear. It most likely results from the  $C_L$  value and perhaps smaller well grid blocks would yield low enough flow rates to generate some curvature.

Table 4.2 reveals that the axial pressure drop is only relevant at early times and when the pressure drawdown between the producer and injector is low. The result is similar to other studies (Novy (1995); Hill and Zhu (1998)).

Table 4.2: List of the percent recovery loss in oil recovery at 10 days, 100 days, and 1000 days for the nine homogeneous tests given in Table D.1.

	<b>%Loss (10 days)</b>	<b>%Loss (100 days)</b>	<b>%Loss (1000 days)</b>	<b>Drawdown, <math>P_o - p_T</math></b>
<b>Test 1</b>	0.024%	0.005%	0.002%	1400 psi
<b>Test 2</b>	0.064%	0.007%	0.004%	800 psi
<b>Test 3</b>	0.167%	0.057%	0.015%	1400 psi
<b>Test 4</b>	0.421%	0.129%	0.032%	800 psi
<b>Test 5</b>	10.466%	2.739%	0.886%	110 psi
<b>Test 6</b>	0.023%	0.015%	0.002%	1400 psi
<b>Test 7</b>	0.066%	0.029%	0.005%	800 psi
<b>Test 8</b>	0.158%	0.069%	0.031%	1400 psi
<b>Test 9</b>	0.411%	0.143%	0.056%	800 psi

Test 5 resulted in significant loss of recovery; however, more tests with lower injection rates need to be simulated. Perhaps counter-intuitively, lower injection rates yielded larger pressure drops for the non-Newtonian polymers. For non-Newtonian fluids, the higher flow rate lowers the viscosity of the fluid in the wellbore and reduces the well axial pressure drop. Therefore, low drawdowns produce a greater axial pressure decrease than large drawdowns. The total axial pressure drop as it changes with time for Test 3 and Test 5 was plotted in Figure 4.8.

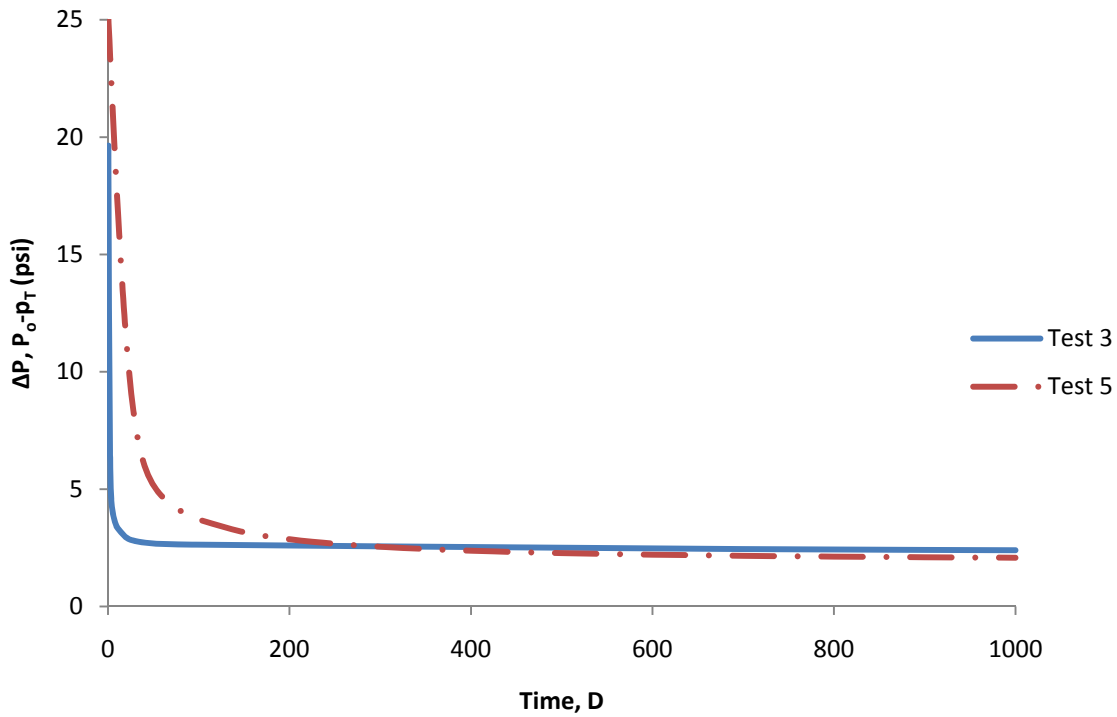


Figure 4.8: Axial well pressure loss comparison as a function of time for Test 3 and Test 5 of Table D.1.

Lower permeability also resulted in more recovery loss. Test 1, 2, 3, and 4 had a permeability of 1 D while Test 6, 7, 8, and 9 had a permeability of 500 md. Figure 4.9 compares the recovery loss at 1000 days for the two permeability values. Low permeability values (e.g., 10 md) need to be tested to determine the recovery implications.

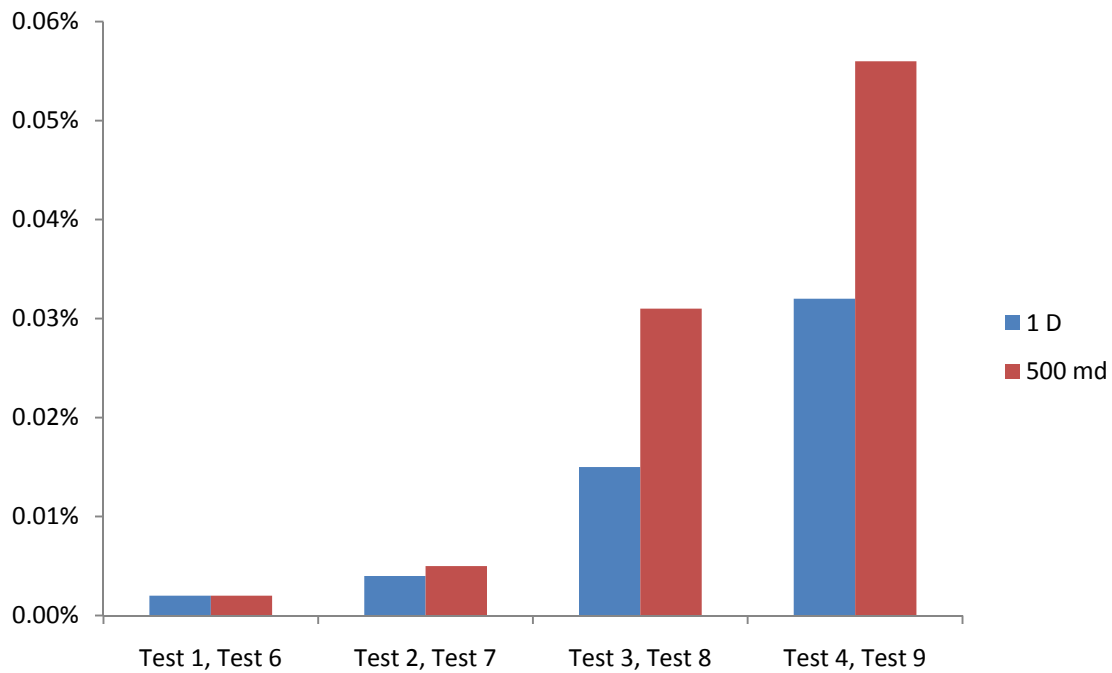


Figure 4.9: Bar graph of percent loss in recovery using Equation 4.4 comparing 1 D tests to 500 md tests.

#### 4.4 HETEROGENEOUS RESERVOIRS

Oilfields are not homogeneous. In fact, heterogeneity is one of the major reasons why polymers are useful in enhanced oil recovery. Water leaves a lot of unrecovered oil partially because of inefficient injection patterns in heterogeneous reservoirs. Polymers have better mobility ratios than water because of their high viscosity; consequently, they can dramatically improve sweep efficiency. As a result, a heterogeneous permeability field was created. The permeability field had a Dykstra-Parsons coefficient of 0.8 and a geometric mean value of 1 D. A probability distribution can be seen in Figure D.1.

The early time injection inefficiencies of the homogeneous cases also occurred in the heterogeneous cases. The cumulative recovery differences at late times were negligible for the heterogeneous cases just as they were for the homogeneous cases. The

axial pressure profiles became more uniform with time just like the homogeneous cases. The images can be seen in Appendix D.

A few differences arose between the homogeneous and heterogeneous cases. The total axial pressure drop for the heterogeneous cases was higher than the homogeneous cases. Figure 4.10 compares the axial pressure profile of Test 5 to Test 14. The parameters for the two tests are the same with the exception of the permeability field.

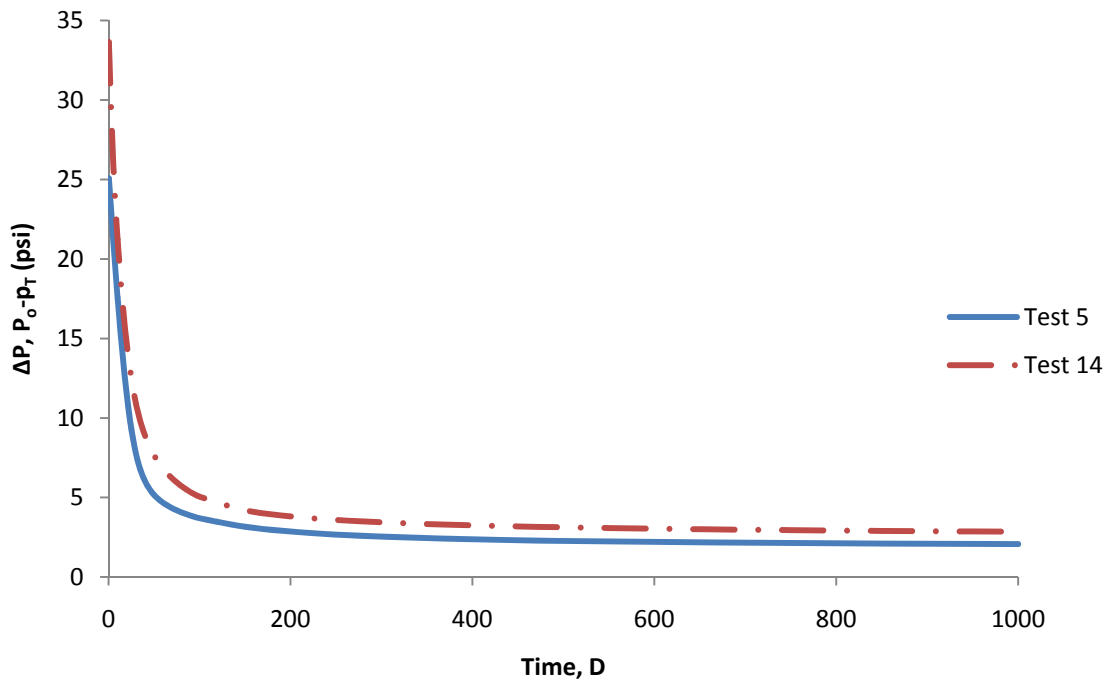


Figure 4.10: Axial pressure profile comparison for Tests 5 and 14.

The axial pressure profile for the heterogeneous cases was not nearly linear like the homogeneous cases. The varying permeability created a unique axial pressure profile. Figure 4.11 plots the axial pressure profile at early times while Figure 4.12 plots later times.

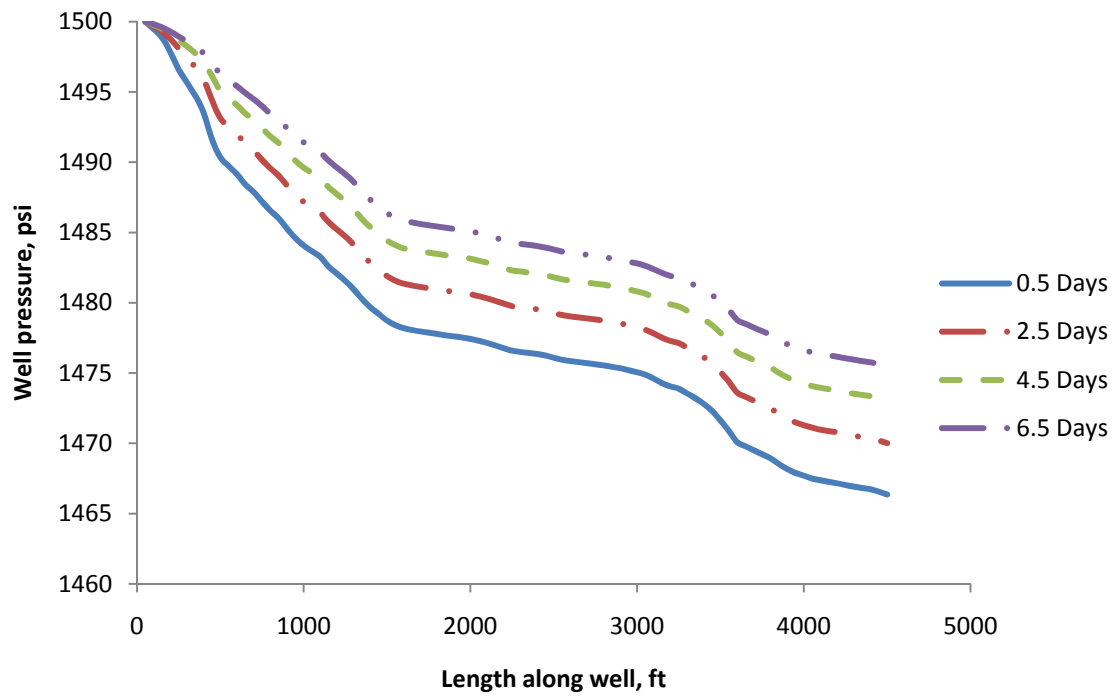


Figure 4.11: Early time axial pressure profiles for Test 14 of Table D.1.

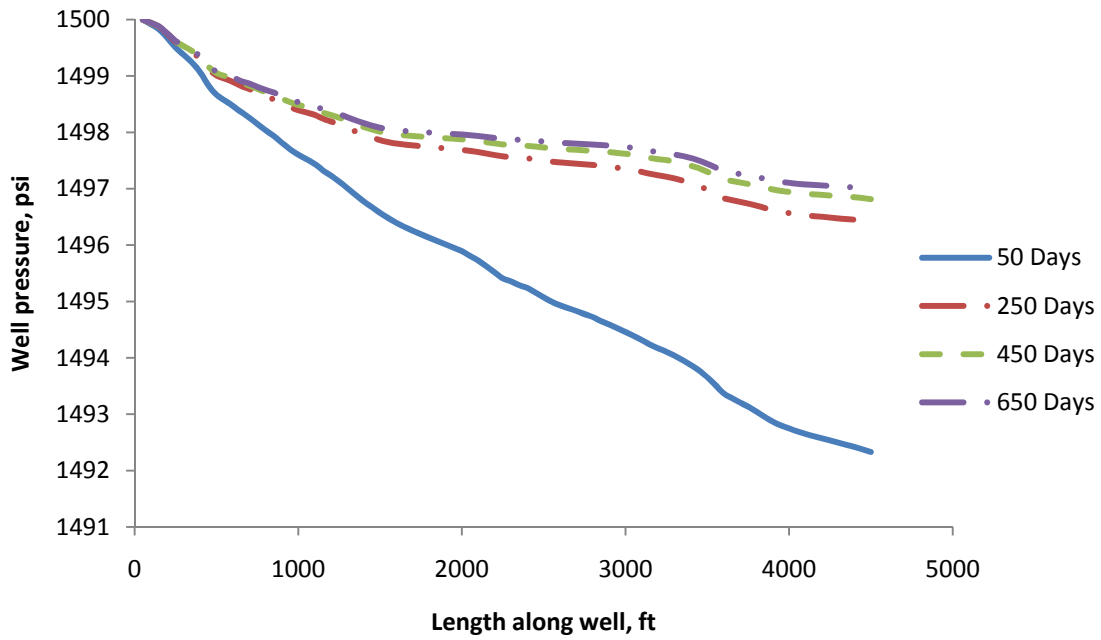


Figure 4.12: Late time axial pressure profiles for Test 14 of Table D.1.

Not only did the axial pressure drop decrease with time, the axial pressure profile became smoother. Figure 4.11 illustrates the axial pressure profile undulating while Figure 4.12 depicts smoother curves.

The heterogeneous cases also produced more percent loss than the homogeneous cases. Figure 4.13 is a histogram comparing Tests 1, 2, 3, and 4 to Tests 10, 11, 12, and 13 respectively at 10 days.

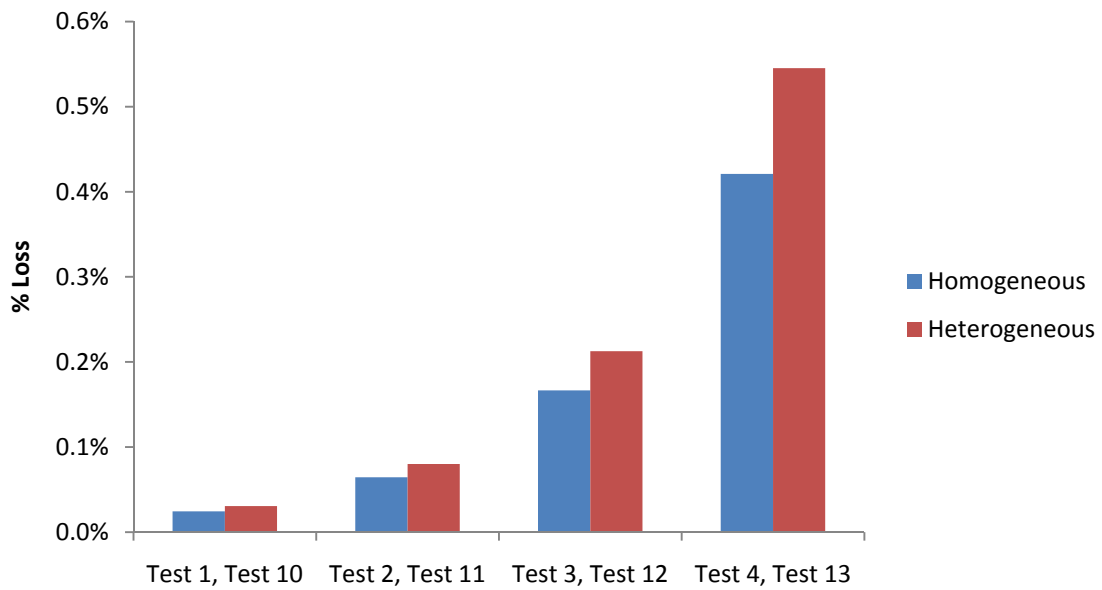


Figure 4.13: Bar graph comparing the percent loss of the homogeneous and heterogeneous cases at 10 days.

The low drawdown cases, Test 5 and Test 14, also show the same trend as the high drawdown cases shown in Figure 4.13. Figure 4.14 depicts the low drawdown cases at 10 days, 100 days, and 1000 days.



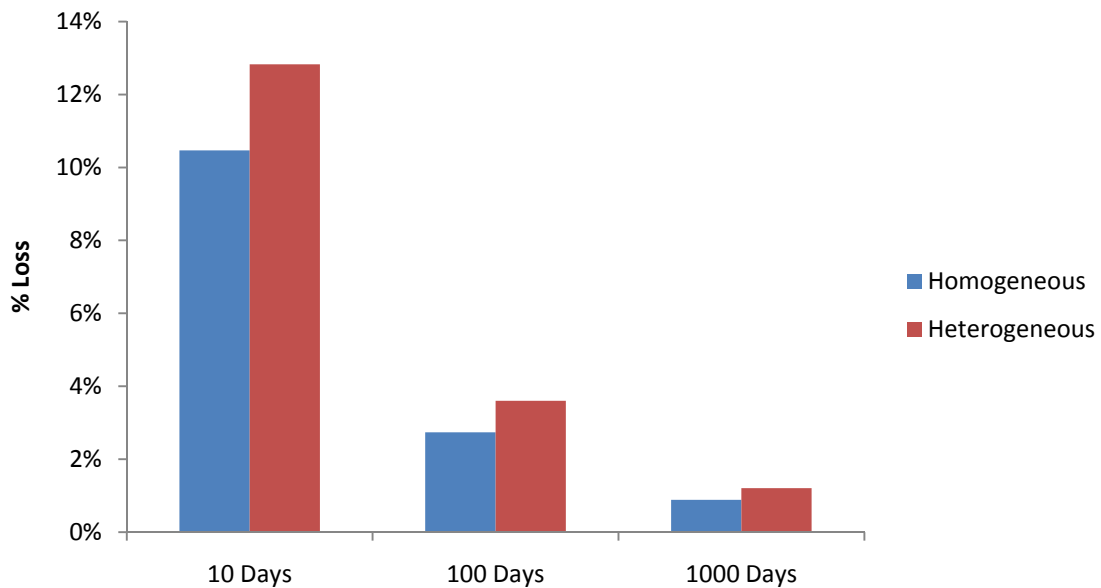


Figure 4.14: Bar graph comparing the percent loss of Tests 5 and 14 at 10 days, 100 days, and 1000 days.

Figure 4.14 displays the same trend as Figure 4.7 where the percent loss decreases with time. The early time losses equally as much as 12% in the heterogeneous case may impact the economics because of the time value of money. A more detailed analysis of the net present value of some EOR projects with the addition of the IPE may yield different managerial decisions.

## **Chapter 5: COMPLETIONS**

Horizontal wells can be completed in a number of ways. Previously, only open-hole completions had been discussed. However, gravel packs and perforations were also modeled to determine the effects of completions on the pressure drop.

### **5.1 GRAVEL PACKS**

Gravel packs are traditionally used to prevent sand production. However, when some production wells become uneconomic because of a high water cut, they are turned into injectors. As a result, the injection of polymers in gravel packs can occur. The gravel pack was modeled as a thin rectangle between the wellbore and reservoir. Figure 5.1 depicts the boundary conditions just as they are shown in Figure 2.2 with the gravel pack included.

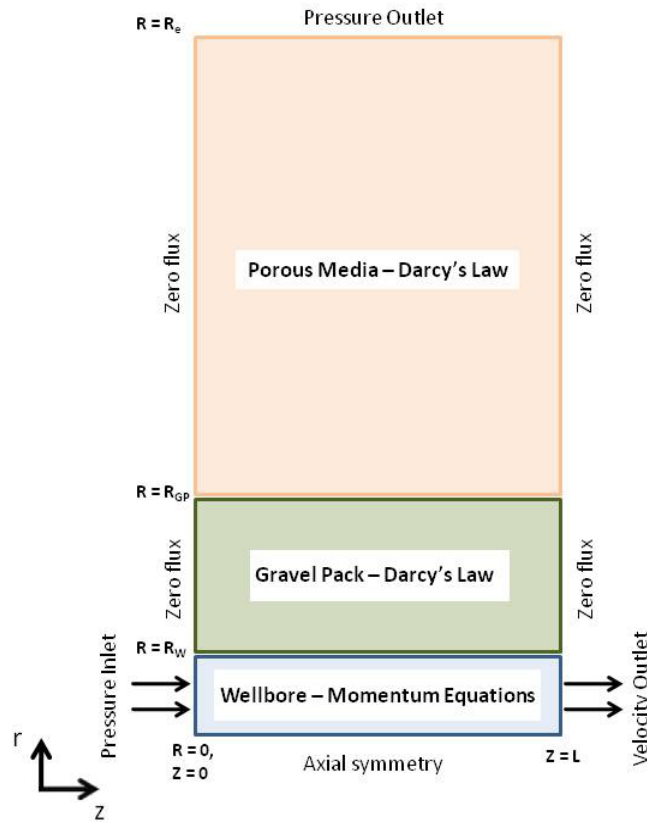


Figure 5.1: COMSOL model with the corresponding physics and boundary conditions including the gravel pack subdomain (radial dimensions of the well and gravel pack are highly exaggerated in the schematic).

The viscosity ratio was evaluated at  $r = R_w$  as was done for the flow of non-Newtonian fluids. The reservoir outlet pressure was still assumed to be  $p_T$  at  $r = R_e$  but a comparison was made to determine whether it should be evaluated at  $r = R_{GP}$ . The model properties were the same as those listed in Table 3.1 with two exceptions: the reservoir width was still 10 meters but it was composed of 0.203 meters of gravel pack and 9.797 meters of reservoir and the segment length was reduced to 10 meters because of extra mesh requirements at the gravel pack-reservoir interface. The permeability of the combined system,  $k_{ave}$ , was evaluated using Equation 5.1, a radial composite system.

$$k_{ave} = \frac{\ln(R_e/R_w)}{\sum_{i=1}^n \frac{\ln(r_i/r_{i-1})}{k_i}} \quad (5.1)$$

The gravel pack was given a permeability of 10 D and the resulting equivalent permeability for the composite geometry was 1 D. A comparison was made between Newtonian, shear-thinning, and viscoelastic fluids in Figure 5.2.

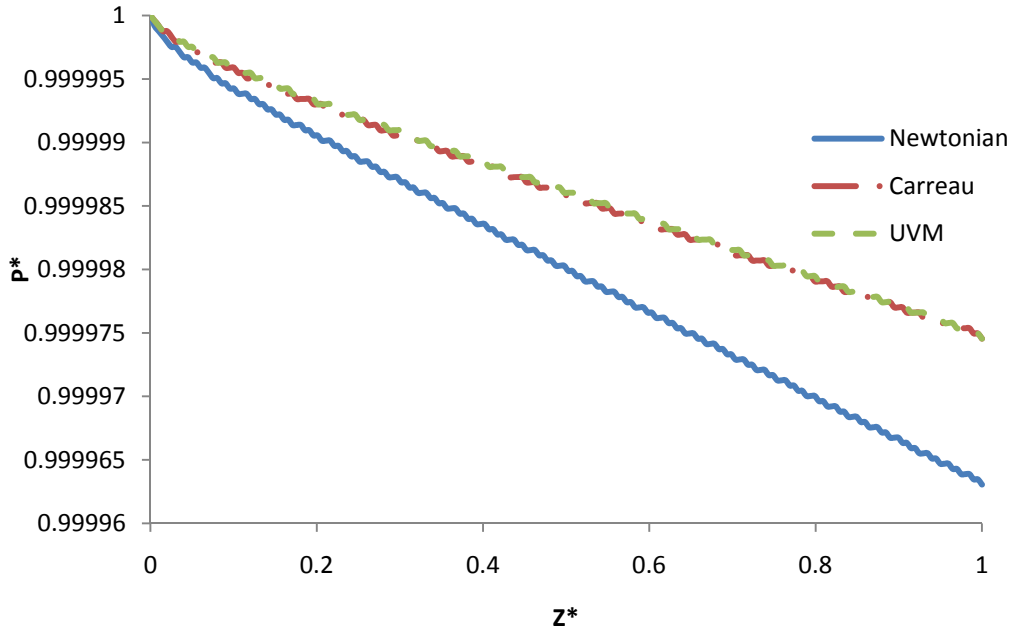


Figure 5.2: Non-dimensional axial pressure comparison between Newtonian, shear-thinning, and viscoelastic fluids with a gravel pack for  $Q_y/Q_z = 0.01$ .

As expected, the Newtonian fluid results in the largest pressure drop with the shear-thinning and viscoelastic fluids having identical results. The viscoelastic effects in porous media do not have an impact on the axial pressure drop within the well. The pressure values evaluated at  $r = R_{GP}$  were compared with the pressure values evaluated at  $r = R_w$ . Figure 5.3 demonstrates that the pressures at  $r = R_w$  yield better results than those at  $r = R_{GP}$ .

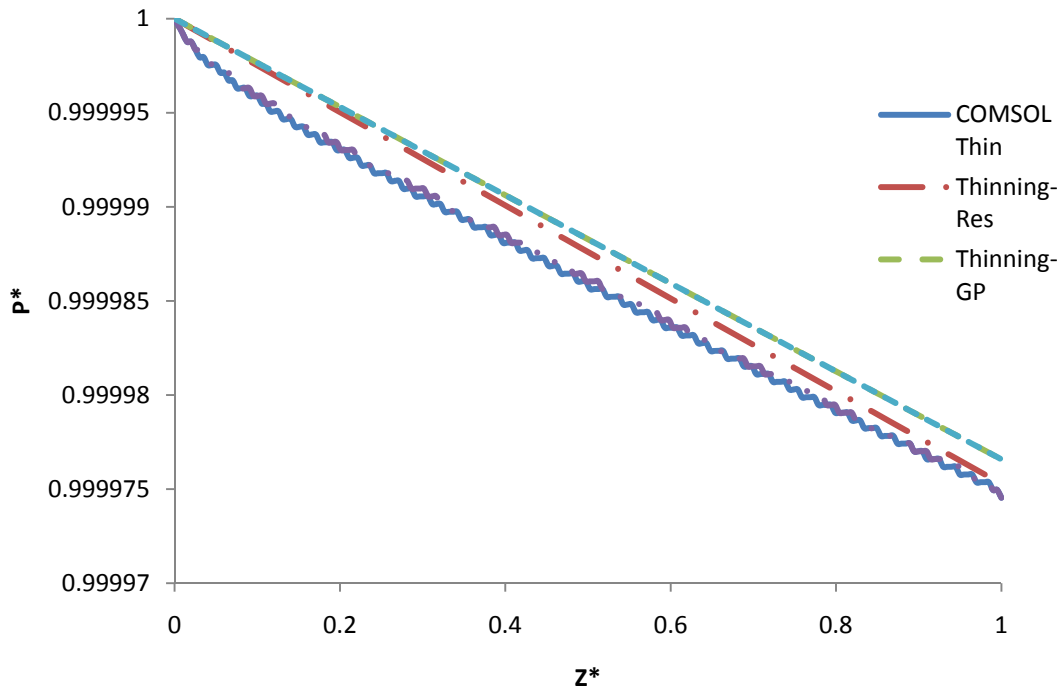


Figure 5.3: Shear-thinning and viscoelastic non-dimensional axial pressure drop with viscosities evaluated at  $r = R_w$  and  $r = R_{GP}$  for  $Q_y/Q_z = 0.01$ .

The COMSOL thinning (Carreau) and thickening (UVM) cases once again demonstrated identical axial pressure profiles. The thickening fluid pressure was also evaluated at  $r = R_{GP}$  but the result was very poor and thus not shown. Clearly, the match was not as good for the gravel pack. Some extra inertial effects might be occurring or perhaps the radial composite value for the permeability was not the best approach. A more in depth study into different permeability options may provide more accurate results and warrants further study.

The axial well pressure drop for a Newtonian fluid with a gravel pack was compared to the same case without a gravel pack. The leakage rates were set to be 20 STB/D/m for both cases. The effective permeability with the gravel pack was larger;

therefore, the gravel pack case required a higher reservoir outlet pressure (lower drawdown) to produce 20 STB/D/m. Figure 5.4 illustrates the comparison between the two Newtonian cases.

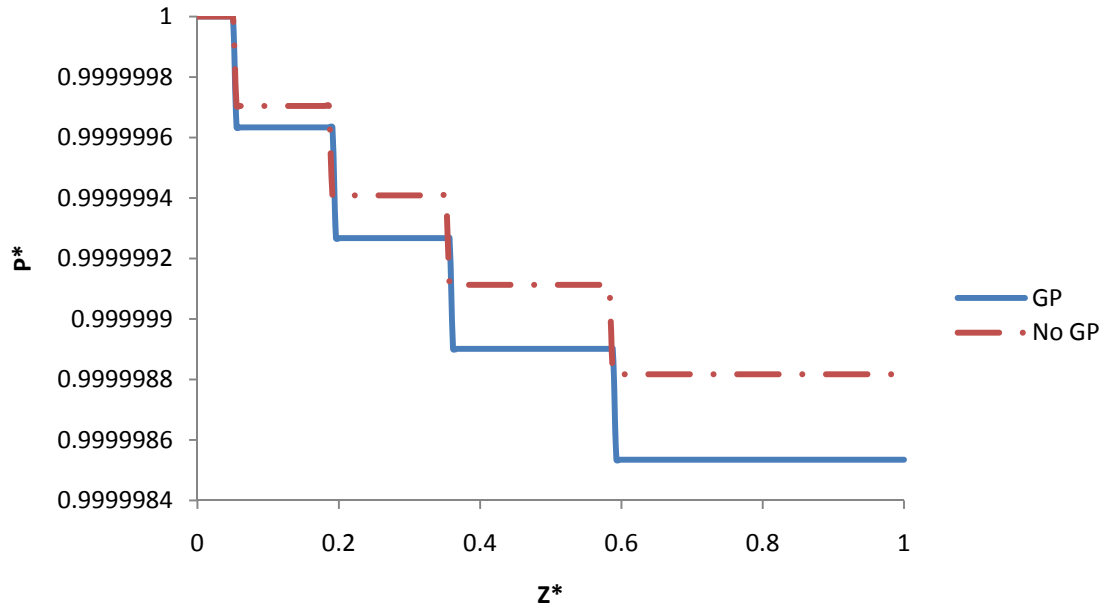


Figure 5.4: Axial pressure drop for a Newtonian fluid both with and without a gravel pack for  $Q_y/Q_z = 0.1$ .

The axial pressure drop was larger for a gravel pack than for no gravel pack though the absolute value was negligible. The excellent agreements for non-Newtonian fluids without a gravel pack presents an interesting discrepancy between the reasonably poor agreements with a gravel pack, illustrated in Figure 5.3. The apparent viscosity ratio might not be best evaluated at  $r = R_w$  for a gravel pack. A more detailed analysis of gravel packs with different specifications might yield greater insight into the fluid dynamics occurring in composite radial geometries. The results appear step-like because

the pressure drop was very small over the short segment. The axial pressure values calculated by COMSOL did not have enough digits to produce a smooth curve.

## **5.2 PERFORATIONS**

Perforations allow communication between a cased wellbore and a reservoir. Many different perforation orientations could be modeled; however, for simplicity, the perforations were modeled as cone that was rotated around the well. Figure 5.5 illustrates the boundary conditions and the physics.

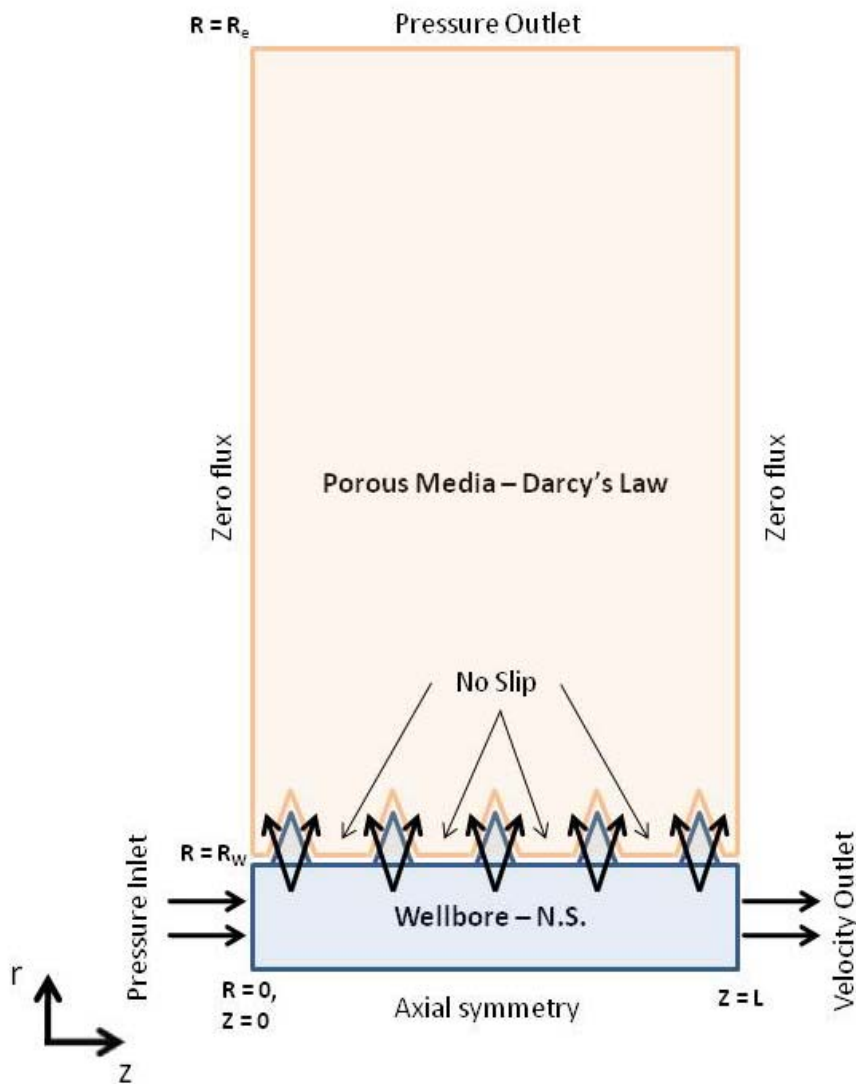


Figure 5.5: COMSOL model with the corresponding physics and boundary conditions for a perforated well.

Perforations dramatically limit area through which the fluid in the well can travel into the reservoir. As a result, a very large pressure drop across the perforations occurs. The IPE, Equation 3.14, was applied for shear-thinning and shear-thickening fluids with the well radius ignoring the perforations and the viscosities were evaluated at the



perforation-reservoir interface. Figure 5.6 compares the IPE to COMSOL for the properties listed in Table E.1.

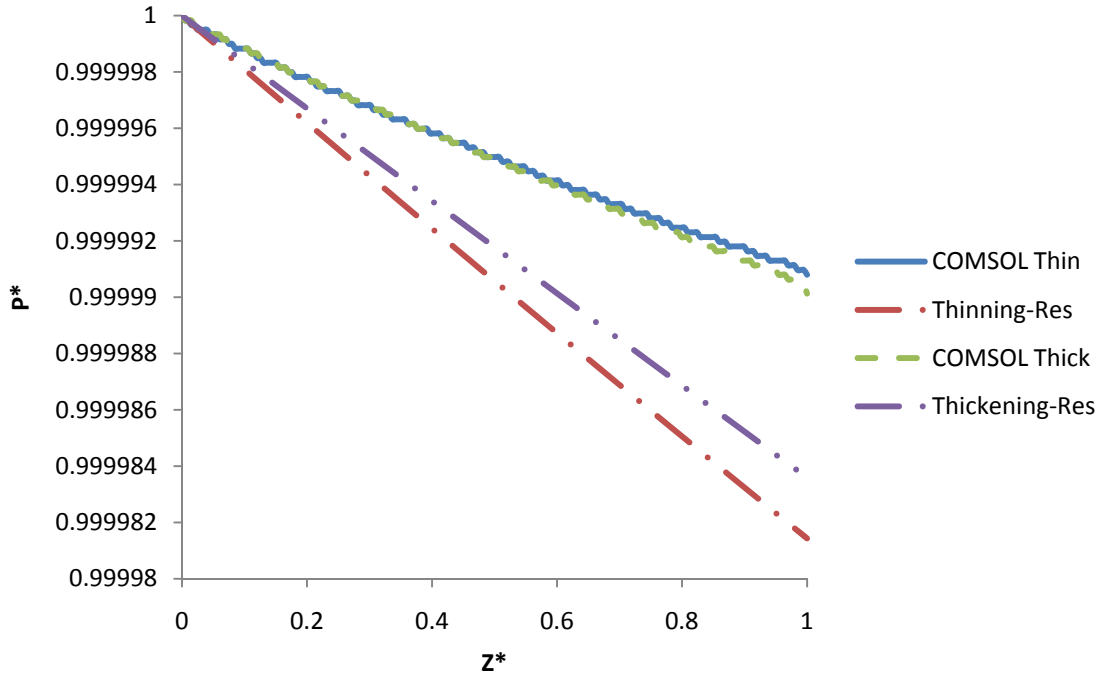


Figure 5.6: Shear-thinning and viscoelastic non-dimensional axial pressure drop with viscosities evaluated at perforation-reservoir interface for  $Q_y/Q_z = 0.01$ .

The agreement was poor most likely because of very large viscosity variations at the perforation-reservoir interface. The viscosity, in the shear-thinning case, fell by an order of magnitude across the interface. Complicated flow patterns most likely occur within the perforations and more study is required to understand the local physics.

The difference in axial pressure drop between perforations and no perforations over the simulated length was negligible. Su and Gudmundsson (1994) claim 15% of axial pressure drop results from mixing caused by perforations though their study did not include non-Newtonian fluids and was referring to production wells. Different perforation orientations may impact the axial pressure, as Yuan et al. (1998), by altering

the shear rate and flow profile in the wellbore. In this model, 20 perforations were added in the 10 meter section, spaced evenly. A more densely populated perforation arrangement could dramatically increase the shear rate. However, as previously discussed, shear-thinning fluids result in less pressure drop than Newtonian fluids with the same zero shear rate plateau. Therefore, a more densely populated set of perforations might reduce the axial pressure drop by thinning the polymer.

## Chapter 6: CONCLUSIONS AND RECOMMENDATIONS

Highly viscous fluids generate a significant pressure drop in tubes. Marshall and Trowbridge (1974) created a pressure correlation for flow in tubes with permeable walls, Equation 1.4. The model was tested using COMSOL software where the wellbore, governed by the momentum and continuity equations, was coupled to the reservoir, governed by Darcy's Law.

The Marshall and Trowbridge (1974) equation is applicable for low leakage rates and high viscosities of Newtonian fluids. Wells in practical oilfield situations can have very large velocity fluctuations. Here, it is proposed to implement the analytical solution by utilizing a unique  $C_L$  value (Equation 1.6) in each well segment as given in a finite difference simulator rather than one  $C_L$  value for the entire well.

Oilfield polymers are non-Newtonian. The non-Newtonian behavior was accounted for in a new Inclusive Pressure Equation (IPE), Equation 3.14. A viscosity ratio (the apparent viscosity in the wellbore, evaluated at  $r = R_w$ , using the Carreau model, divided by the apparent viscosity in the porous media, evaluated at  $r = R_w$ , using the UVM proposed by Delshad et al. (2008)) was added to the conductivity equation, Equation 1.5. The viscosity value in the original  $C_L$  equation (Equation 1.6) was modified to be the apparent viscosity in the well at  $r = R_w$ . Viscoelastic properties do not impact the axial well pressure profile. The new equation is applicable for Newtonian fluids (set  $\mu_0 = \mu_\infty$  and  $\mu_{\max} = 0$ ) and non-Newtonian fluids with any well radius and reservoir permeability.

The IPE was implemented in UTCHEM, a finite-difference reservoir simulator, to examine the importance of the resulting pressure decrease. Injection inefficiencies

occurred at early times but did not significantly impact oil recovery in any case that was tested. The loss of early production has a greater impact on the economics of a project than the loss of late production because of the time value of money. Consequently, the economics of a polymer flood might be dramatically impacted since axial pressure drops results in reduced oil recovery at early times for low drawdown cases. However, the well-reservoir interaction mitigates the pressure reduction with time resulting in virtually no loss in oil recovery at later times.

#### **RECOMMENDATIONS AND FUTURE WORK**

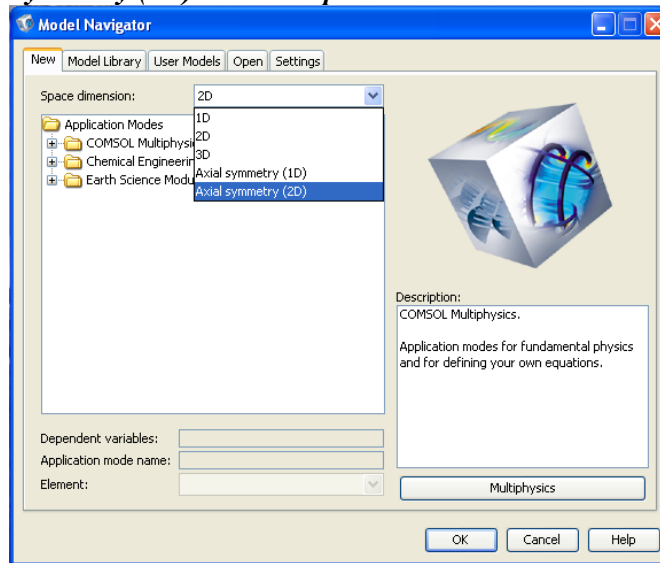
- A 2<sup>nd</sup> order polynomial appeared to describe the ratio of a CFD solution to Marshall and Trowbridge (1974) for a wide range of flow conditions. It is possible the coefficients could be related to the fluid and medium properties, but more work to understand the physical meaning behind the coefficients could provide further insight into the mathematical and physical behavior of fluids in tubes with permeable walls.
- Only one highly viscous polymer was tested in both COMSOL and UTCHEM. A larger set of tests for viscoelastic fluids may yield a more rigorous conclusion regarding the relevance of viscous pressure drops for polymer injections.
- Different non-Newtonian fluids, e.g., Bingham fluids, and viscosity correlations, e.g., pure power law without the plateaus found in the popular Carreau model, could also be simulated to determine if the IPE will also properly predict the axial pressure behavior.
- Further inquiry into the pressure equalizing behavior of the well-reservoir system is warranted. The exact cause of this phenomenon remains unknown.

- Gravel packs and perforations were briefly explored; however, a more comprehensive set of completions would be useful to determine a more appropriate guess as to the importance of the viscous pressure drop. Liners, different gravel pack specifications, and different perforation orientations can all be explored. Even fractured wellbores may merit some inspection.
- A comparison to an actual field injection could also aid in the validity of the model. Pressure gauges could be placed along a wellbore to determine the accuracy of the IPE.
- The reverse trend of the Hagen-Poiseuille equation presents an opportunity for further study. A peak pressure drop must occur because zero flow produces zero pressure drop and yet lower axial volumetric fluxes yield higher axial pressure drop than higher axial volumetric fluxes as discussed in Figure 4.8.
- The net impact on the economics of a polymer flood because of early time production losses warrants examination. Only one polymer was tested and many other tests need to be simulated to determine a comprehensive set of data regarding the economic magnitude of early time production losses.

## Appendix A: MODEL BUILDING INSTRUCTIONS

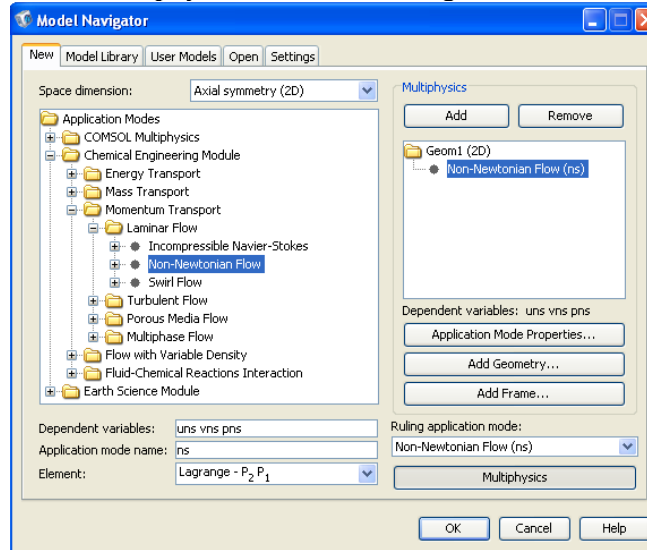
COMSOL Multiphysics™ is a finite-element software that was used to analyze the theoretical Marshall and Trowbridge (1974) solution. The coupled system of a well and reservoir was created using the following steps.

1. Select *Axial Symmetry (2D)* from the *Space dimension* tab



The axial symmetry was used to create a rotated model about the center of the wellbore. The symmetrical nature of the coupled system creates a 2D rather than 3D problem because no variation in the  $\vartheta$  direction, using cylindrical coordinates (i.e.  $r$ ,  $\vartheta$ , and  $z$ ), was assumed.

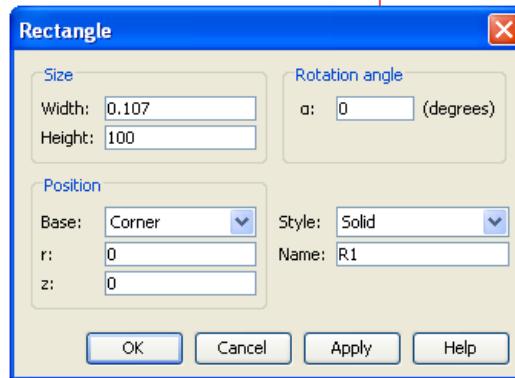
2. Select **Chemical Engineering: Momentum Transport: Laminar Flow: Non-Newtonian Flow**:
  - a. In the Dependent variables type: *uns vns pns*
  - b. In the Application mode name type: *ns*
  - c. Then select **Multiphysics** on the bottom right and click **Add**



3. Select **Porous Media Flow: Brinkman Equations**:
  - a. In the Dependent variables type: *ubr vbr pbr*
  - b. In the Application mode name type: *br*
  - c. Then click **Add**
  - d. Click **OK**

The physics are governed by Navier-Stokes equations in the wellbore and Darcy's law in the porous media. Darcy's law is only pressure dependent; therefore, Brinkman equations were used instead to allow for velocity dependence in the viscosity calculation.

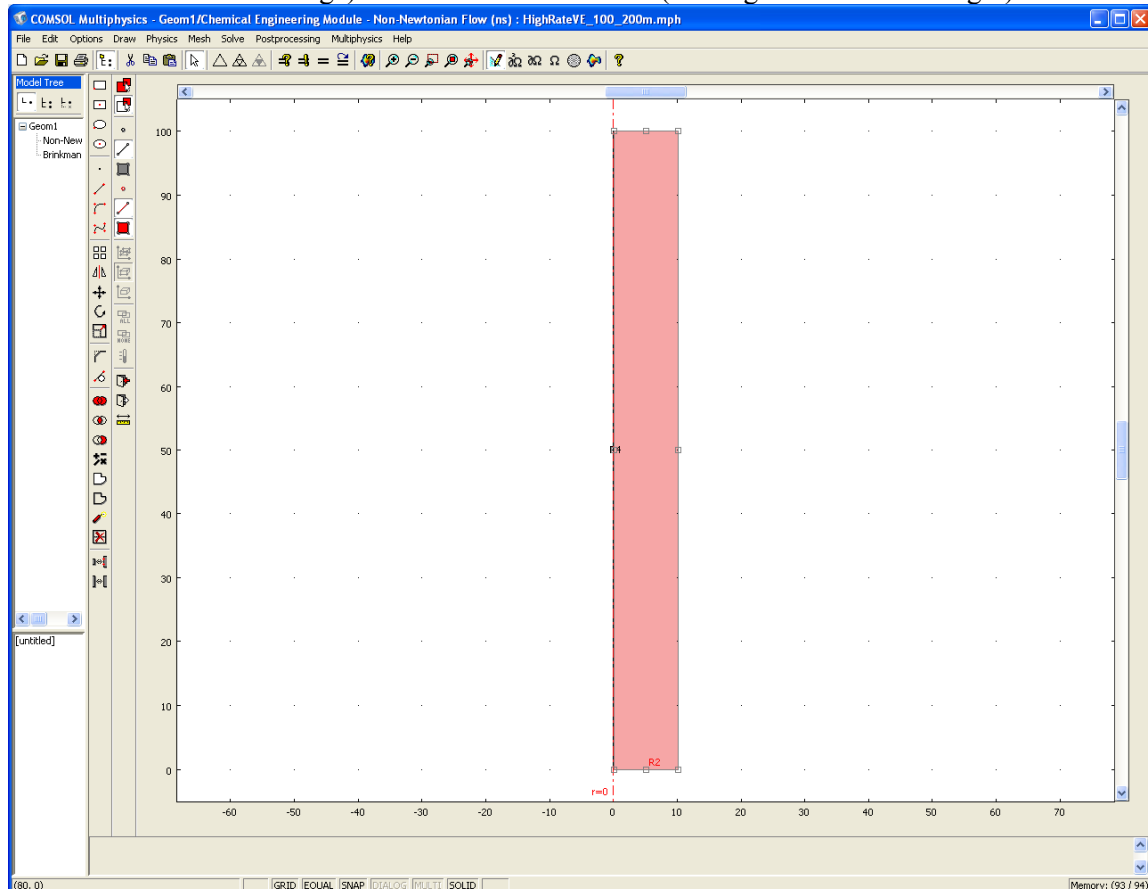
4. Click **Draw: Specify Objects: Rectangle:**
  - a. Type 0.107 in the Width, 100 in the Height.
  - b. Click **OK**



- c. Repeat with dimensions for R2:
  - i. Width: 10
  - ii. Height: 100
  - iii.  $r$ : 0.107
  - iv.  $z$ : 0
  - v. Click **OK**



- d. Then click Zoom Extents button. This should create two rectangles, one for the pipe (the one on the dotted red line marking the symmetry but is too small to see in this image) and one for the reservoir (the large section on the right).



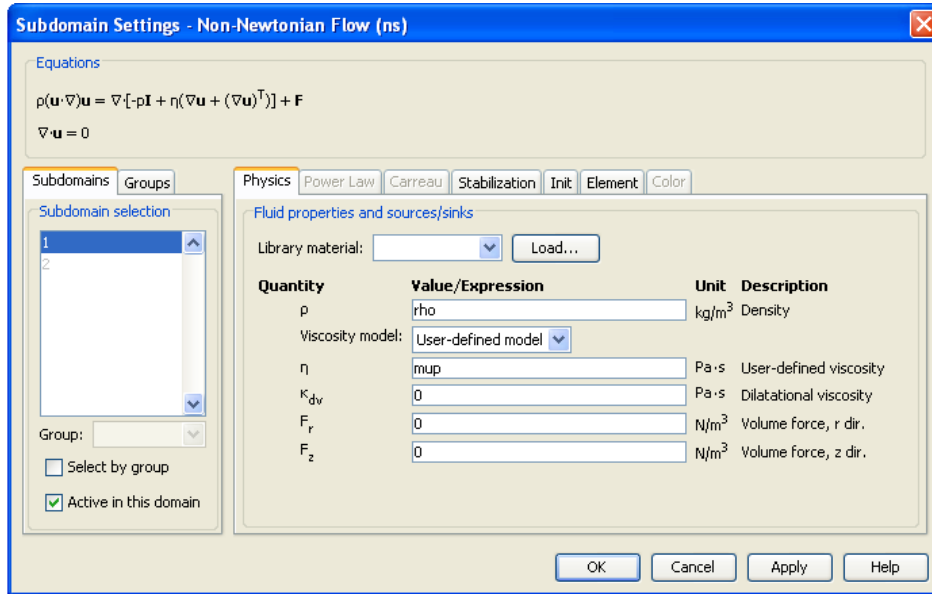
The dimensions are set to meters; therefore, the well radius of 0.107 meters corresponds to a 0.35 ft radius. The 10 meter thick reservoir was chosen because the viscosity value stabilizes around 10 meters. Therefore, no more fluctuation occurs with a larger reservoir thickness and it would only add computation. The 100 meters were chosen as the largest length that could be solved given the computer limitations to allow for mesh optimization.

5. Select **Options: Constants:**
  - a. Enter the values shown below
  - b. Click **OK**

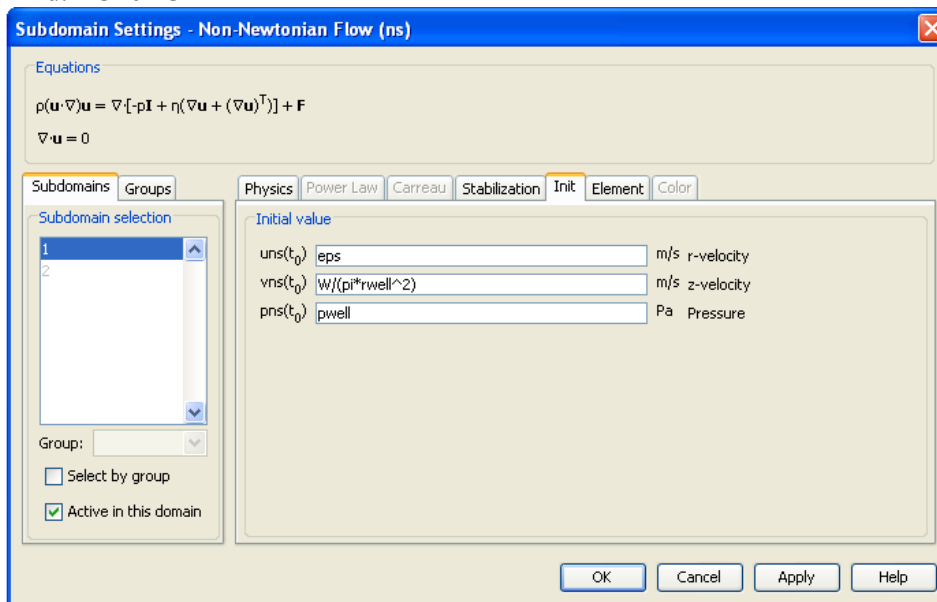
Name	Expression	Value	Description
rho	1000 [kg/m^3]	1000[kg/m^3]	Density
W	$((1000 \cdot 1589) / (3600 \cdot 24))$ [m^3/d]	$(2.128612e-8)$ [m^3/s]	Injection rate
rwell	.107 [m]	0.107[m]	Well radius
pwel	1.03448276e7 [Pa]	1.034483e7[Pa]	Well pressure
mup	128 [mPa*s]	0.128[kg/(m·s)]	Zero viscosity
muw	0.2 [mPa*s]	$(2e-4)$ [kg/(m·s)]	Infinite viscosity
mumax	250 [mPa*s]	0.25[kg/(m·s)]	Maximum viscosity
n1	.653	0.653	Thinning
n2	1.5	1.5	Thickening
alpha	2	2	
C	1	1	
tau	.023	0.023	Thickening
lam	1 [s]	1[s]	Thinning
lamda	.03 [s]	0.03[s]	Thickening
phi	.31	0.31	Porosity
Sw	.65	0.65	Water saturation
krw	1	1	Water relative perm
Umax	.001 [m/s]	0.001[m/s]	Max velocity in wellbore
perm	9.869e-13 [m^2]	$(9.869e-13)$ [m^2]	Reservoir perm

All of the constant variables are placed here. The units must be put in brackets. COMSOL does not recognize centipoises so viscosities must be entered as mPa\*s or Pa\*s. Pressure can be specified as psi or Pa but the shaded gray region will automatically convert it to metric units.

6. Select **Non-Newtonian** in the box on the far left
  - a. Click **Physics: Subdomain Settings**. Select 2 in the subdomain box, click **Active** in this domain. That should remove the check mark.
  - b. This means that the Non-Newtonian physics is solely in domain one, the tubing. Then enter the values shown below.

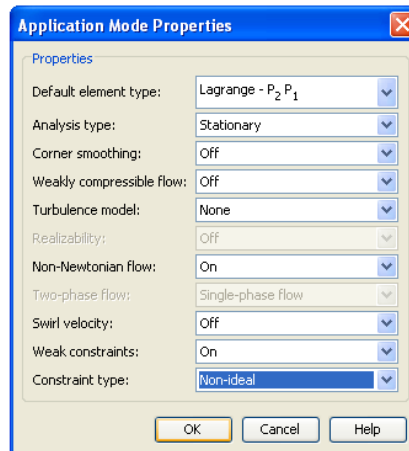


7. Select the **Init** tab
  - a. For  $uns(t_0)$ , enter eps
  - b. For  $vns(t_0)$ , enter  $W/(\pi \cdot r_{well}^2)$
  - c. For  $pns(t_0)$ , enter  $p_{well}$
  - d. Click **OK**



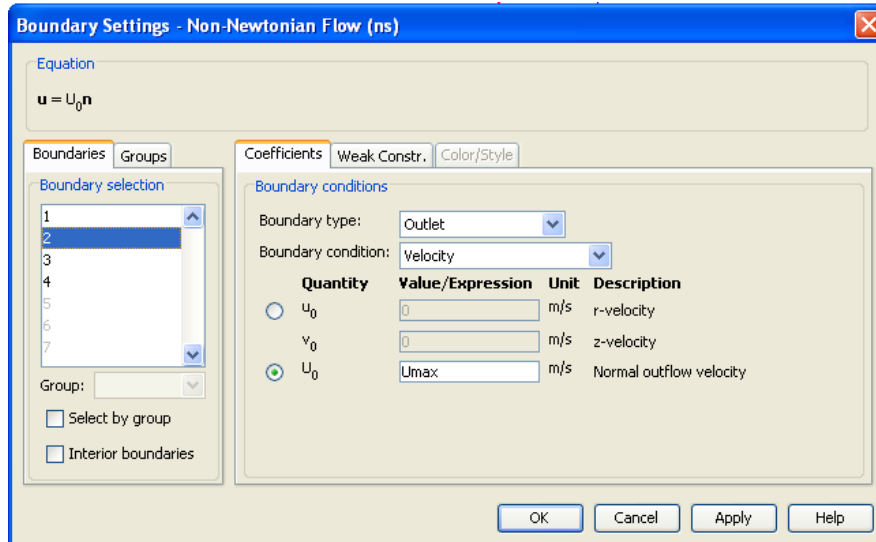
The initial settings were taken from a similar model in the model library. The importance is unknown as a comprehensive study of the conditions was not undertaken. The  $z$ -velocity condition was altered and no discernable difference occurred in the solution values but the computation time possibly could have changed; it was not documented.

8. Select **Physics: Properties**. Notice that Non-Newtonian Flow can be turned on or off. It should be turned on now. If it was turned off, it would revert to Incompressible Navier-Stokes equations.
  - a. Set Weak Constraints – **ON**
  - b. Set Constraint Type – **Non-Ideal**
  - c. Click **OK**



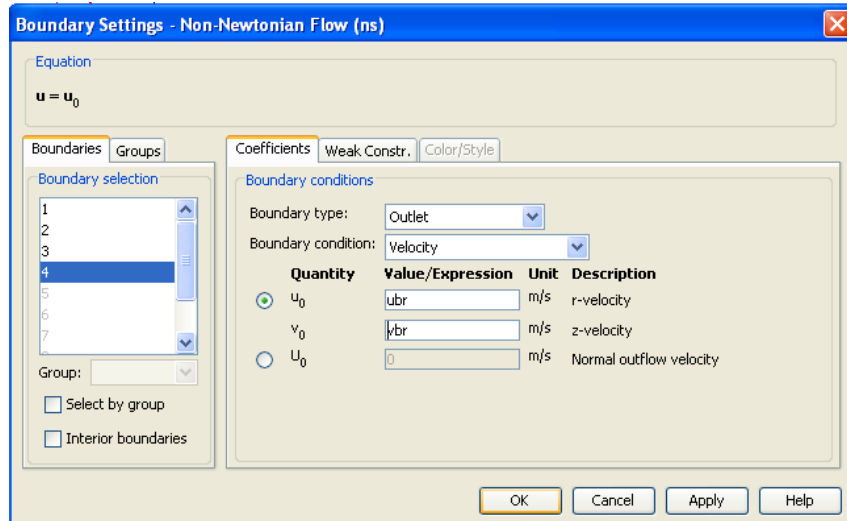
9. Select **Physics: Boundary Settings**:
  - a. Select 1 on the left
    - i. Boundary type – Symmetry Boundary
    - ii. Boundary condition – Axial Symmetry

- b. Select 2
  - i. Boundary type – Outlet
  - ii. Boundary condition – Velocity
    - 1.  $U_o - U_{max}$



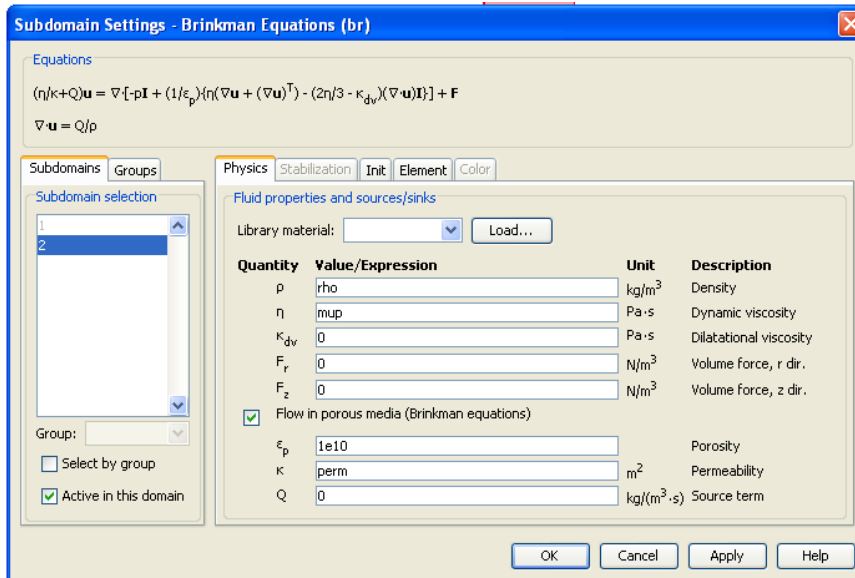
- c. Select 3
  - i. Boundary type – Inlet
  - ii. Boundary condition – Pressure, no viscous stress
    - 1.  $p_o - p_{well}$
- d. Select 4
  - i. Boundary type – Outlet
  - ii. Boundary condition – Velocity
    - 1.  $u_o - ubr$
    - 2.  $v_o - vbr$
  - iii. This couples the Navier-Stokes equations to the Brinkman equations. One side must have velocity and the other pressure. I have found that velocity out of the pipe and pressure into the gravel pack couples better than vice versa.

e. Click **OK**



The boundary settings are explained in Chapter 2. The velocity outlet can be specified as any function and some other options were attempted. If an analytical function can describe the velocity profile, it can be used.

10. Select **Brinkman equations** on the far left: **Physics: Subdomain Settings:**
  - a. Select 1 in the far left.
    - i. Select **Active** in this domain (check mark should go away).
  - b. Select 2
    - i. Enter the values shown below



- ii. The 1E10 in the porosity box is the alteration to the Brinkman equations that convert them to Darcy's law. While not physically possible, mathematically it works and is useful.
- iii. Click the **Init** tab. Enter  $p_{well}$  for  $p_{br}(t_0)$ .
- iv. Click **OK**

11. Select **Physics: Properties:**

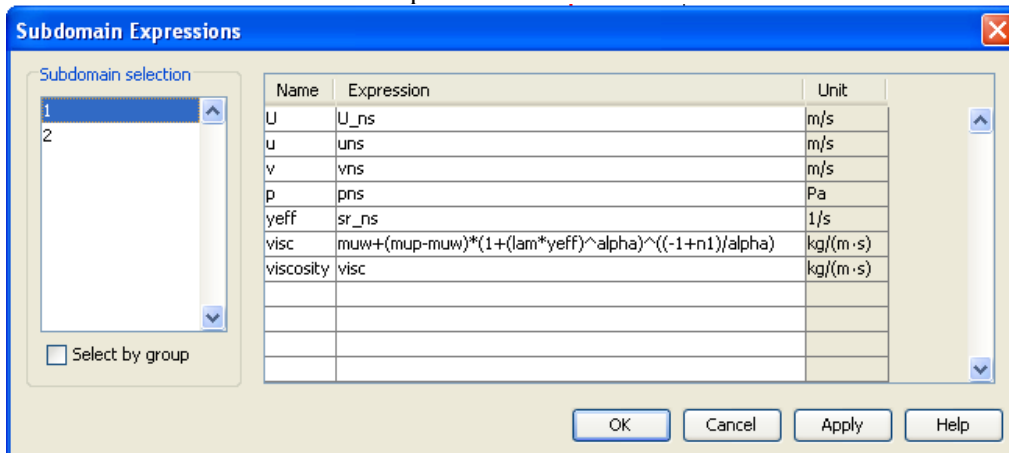
- a. Set Weak Constraints – **ON**
- b. Set Constraint type – **Non-Ideal**
- c. The only difference from this step and step 8 is Non-Newtonian should be OFF now.

12. Select **Physics: Boundary Settings:**

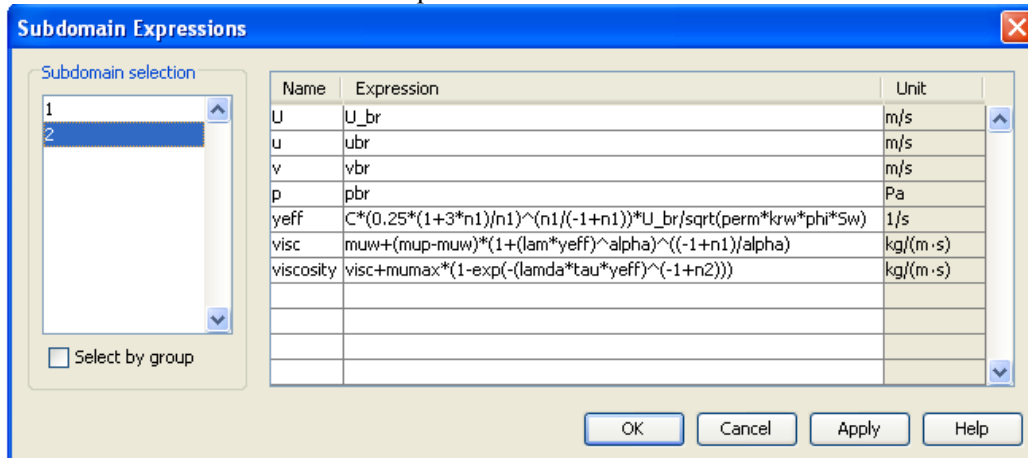
- a. Select 4
  - i. Boundary type – Inlet
  - ii. Boundary condition – Pressure, no viscous stress
  - iii.  $P_o = p_{ns}$
- b. Select 5
  - i. Boundary type – Wall
  - ii. Boundary condition – Slip
- c. Select 6
  - i. Boundary type – Wall
  - ii. Boundary condition – Slip
- d. Select 7
  - i. Boundary type – Outlet
  - ii. Boundary condition – Pressure, no viscous stress
  - iii.  $P_o = 0.9 * p_{well}$
  - iv. Click **OK**

The slip condition applied on Boundary 5 and Boundary 6 is because the well segment is part of the entire well. As a result, a no velocity condition would yield a non-physical situation in which the velocity in the reservoir would be zero along a plane. The boundary is intended to represent a no flux boundary.

13. Select **Options: Expressions: Subdomain Expressions:**  
 a. Select 1 and enter the equations shown below



- b. Select 2 and enter the equations shown below



The subdomain expressions allow for the user to define any new properties. It does not alter the differential equation but does allow an expression to be used rather than a constant for certain variables in the differential equations.

14. Select **Mesh: Free Mesh Parameters**

- a. Select the Boundary tab
- i. Select 4 in the left box
  - ii. Enter 0.08 for the Maximum element size. The important point is mesh refinement should yield a more accurate result but at the expense of memory and computation time. It is possible to run out of memory but that will be different for every computer.
  - iii. Click **OK**

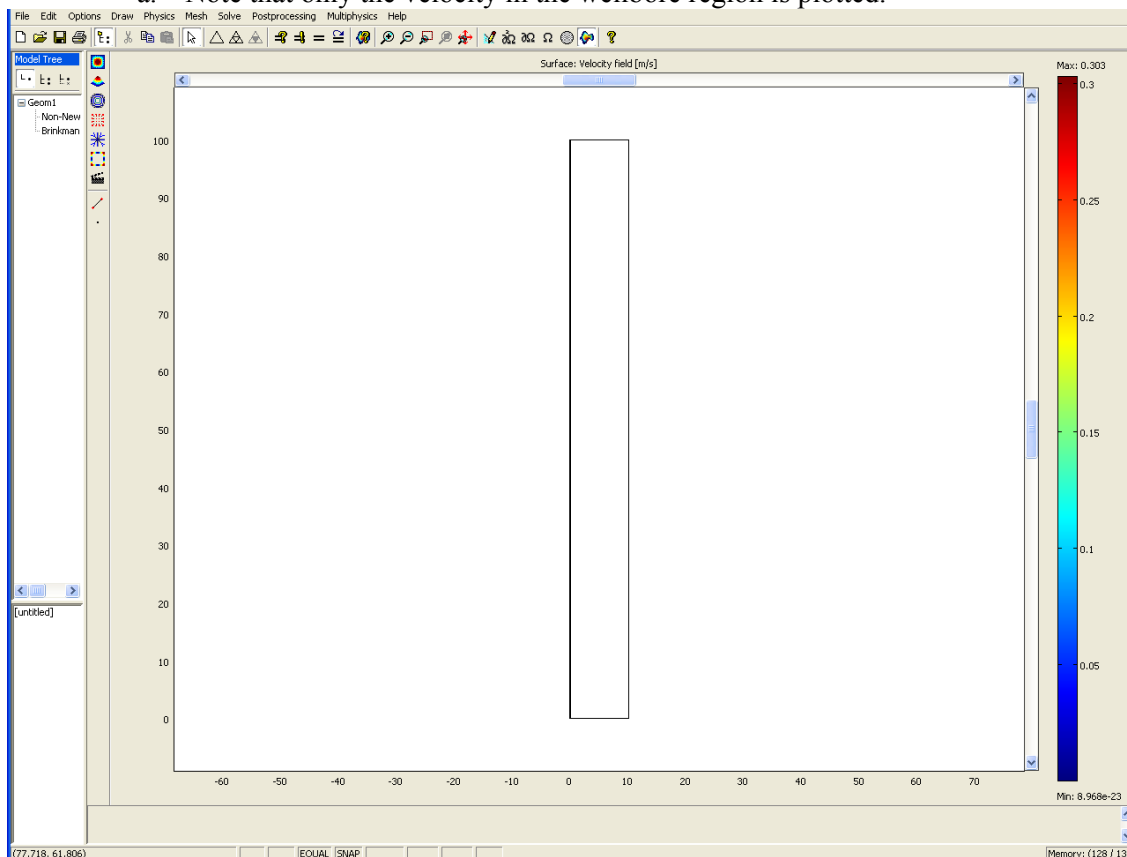


The mesh refinement is a function of well length and computer memory. A separate optimization will probably be required for each different computer.

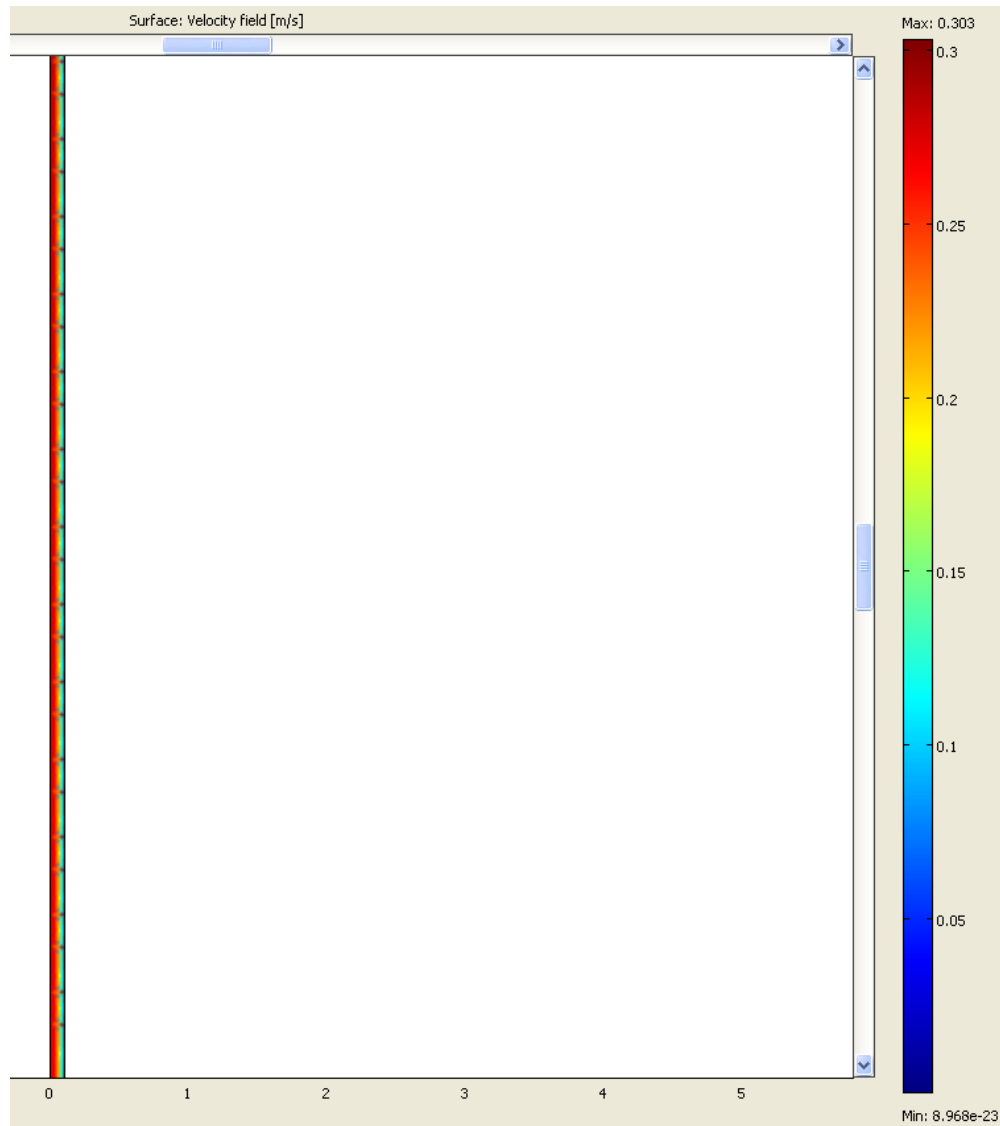
15. Select Solver: Solver Parameters
  - a. Click the **Stationary** tab
    - i. Enter 150 for Maximum number of iterations
    - ii. Click **OK**

16. Click the **Initialize mesh** on the toolbar

17. Click **Solve**
  - a. Note that only the velocity in the wellbore region is plotted.

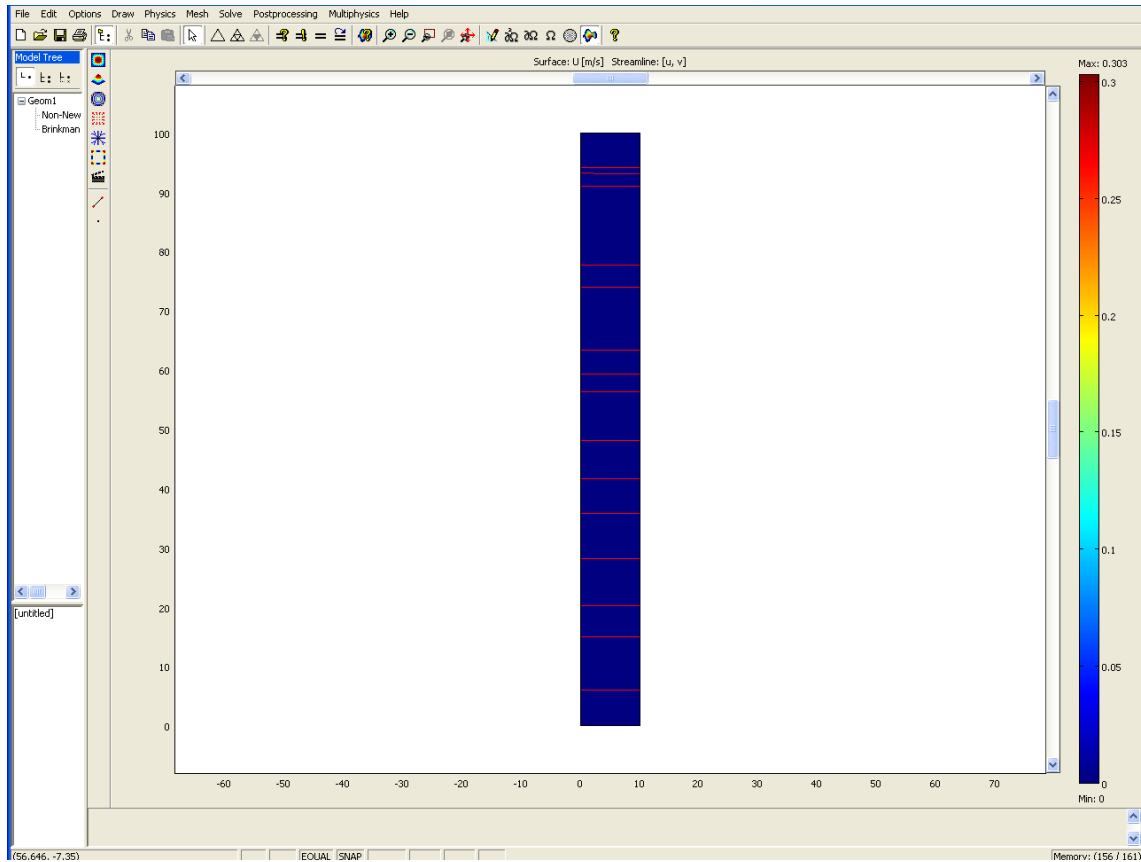


The image above looks like there is no plot; however, the wellbore is very small compared to the reservoir thickness. The image below is a blown up picture of the wellbore illustrating the velocity profile.



18. Select *Postprocessing: Plot Parameters:*
  - a. Select the *Surface* tab
    - i. Enter  $U$  for expression

- b. Select the **Streamline** tab
  - i. Enter  $u$  and  $v$  for the  $r$  and  $z$  components respectively
  - ii. Click the box at the top left that says **Streamline plot** (a check mark should appear)
  - iii. Click **OK**

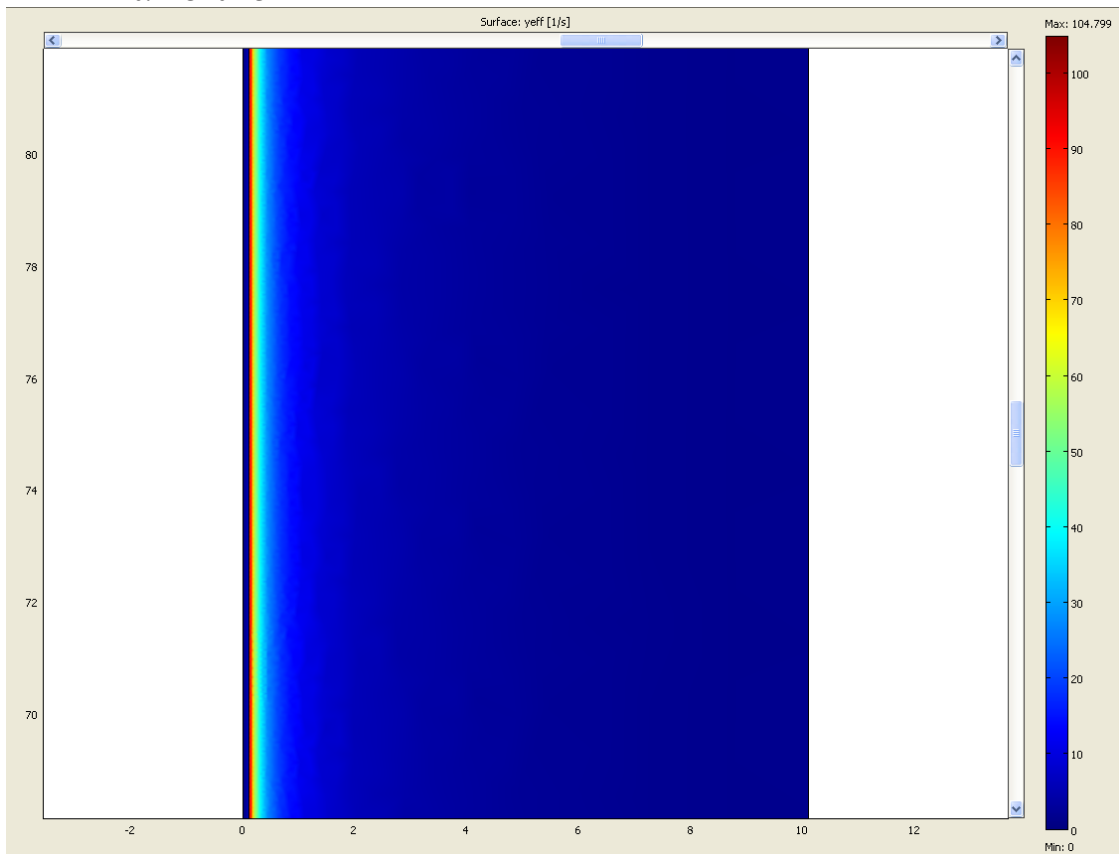


19. Select **Solve: Solver Manager:**
  - a. Select **Current Solution**
  - b. Click **OK**

The current solution allows the user to now have an iterative velocity because an initial velocity is specified. The solving of the Newtonian case first can also give faster convergence because the solution may not change that dramatically.

20. Select **Non-Newtonian** on the far left: **Physics: Subdomain Settings:**
  - a. Highlight 1 on the far left
  - b. Type  $visc$  for the User-defined viscosity for shear thinning (viscosity for shear thickening)
  - c. Click **OK**

21. Select **Brinkman equations** on the far left: **Physics Subdomain Settings:**
  - a. Highlight 2 on the far left
  - b. Type *visc* for User-defined viscosity for shear thinning (viscosity for shear thickening)
  - c. Click **OK**
22. Click **Initialize Mesh**
23. Click **Solve**
24. Select **Postprocessing: Plot parameters:**
  - a. Click the **Surface** tab
  - b. Enter *yeff* in the Expression box
  - c. Click **OK**



## **Appendix B: NEWTONIAN CASES**

The following images detail some of the 48 well tests that were run as well as the low and high leakage rate comparisons for the 1,500 meter wells that were tested in the case of the shear-thinning and shear-thickening polymer validations. The plots will include the alteration of using a single  $C_L$  value for each grid block, labeled New  $C_L$ . Table B.1 includes the test plan and the corresponding psi drop for each test. The images, Figure B.1 through Figure B.7, are all for a 30,000 STB/D injection rate and a 200 cp viscosity.

Table B.1: List of 48 full-length wells and the corresponding total axial pressure drop to determine the limitations of Marshall and Trowbridge (1974).

$\mu$ , cp	$Q_o$ , STB/D	600 meters	1,800 meters	3,000 meters
		$\Delta P$ , psi	$\Delta P$ , psi	$\Delta P$ , psi
10	10,000	0.1224	0.4604	0.8132
	20,000	0.1785	0.9231	1.6681
	30,000	0.1602	1.3324	2.5089
	40,000	0.0805	1.6720	3.3003
100	10,000	1.4999	4.5993	7.8138
	20,000	2.8102	9.3168	15.6623
	30,000	4.2894	13.9800	23.6030
	40,000	5.5906	18.6303	31.6161
200	10,000	3.0459	9.2787	15.6541
	20,000	5.9969	18.6840	31.2518
	30,000	8.8757	27.9864	46.9442
	40,000	11.6853	37.2659	62.6947
300	10,000	4.6010	13.9538	23.5319
	20,000	9.0857	28.0682	46.9059
	30,000	13.4920	42.0387	70.3607
	40,000	17.8286	56.0005	93.8472

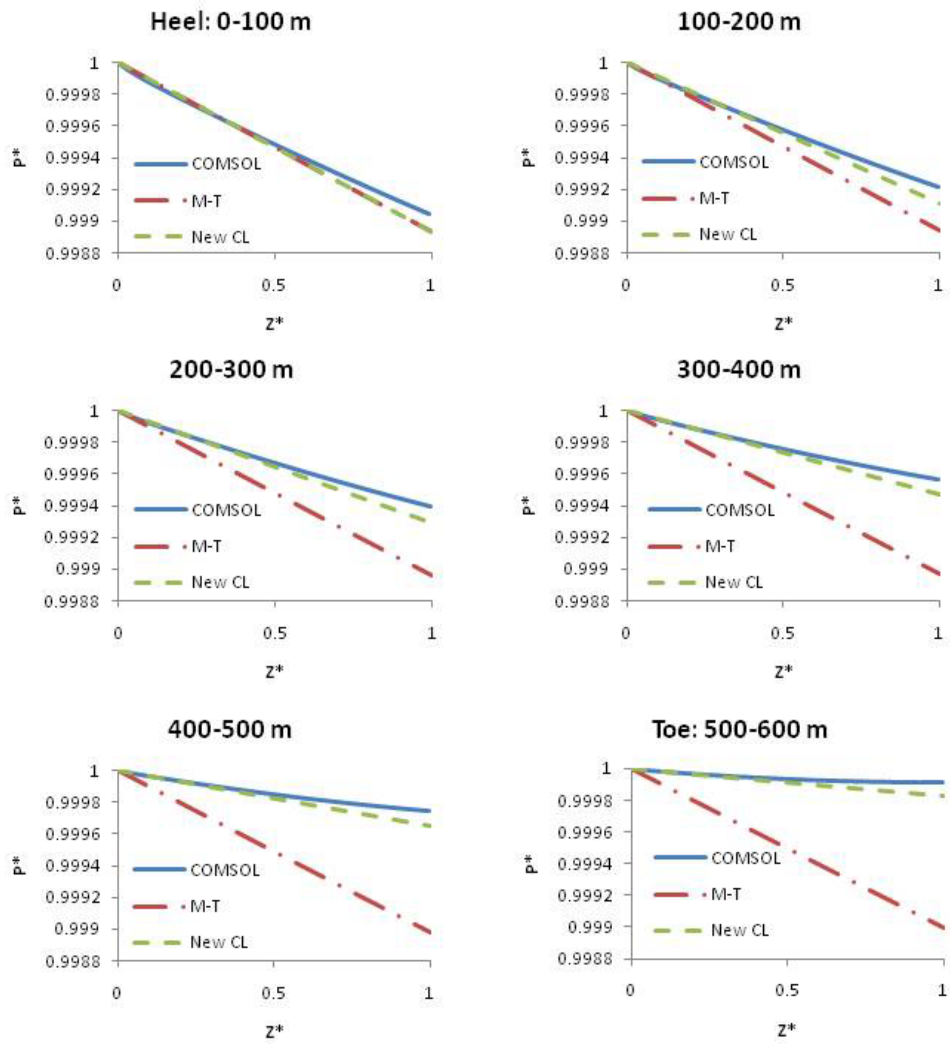


Figure B.1: Marshall and Trowbridge (1974) equation, M-T, compared to the COMSOL solution along the well for 600 meter case.

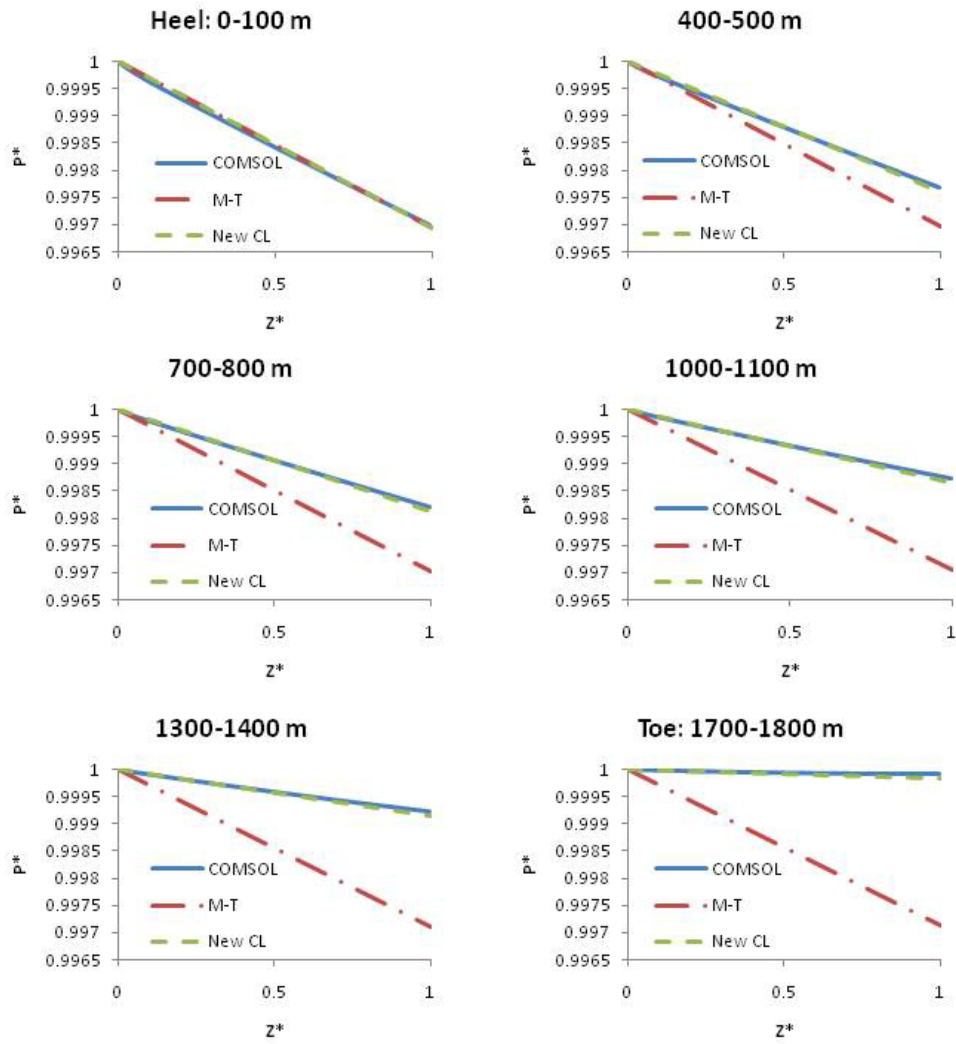


Figure B.2: Marshall and Trowbridge (1974) equation, M-T, compared to the COMSOL solution along the well for 1800 meter case.



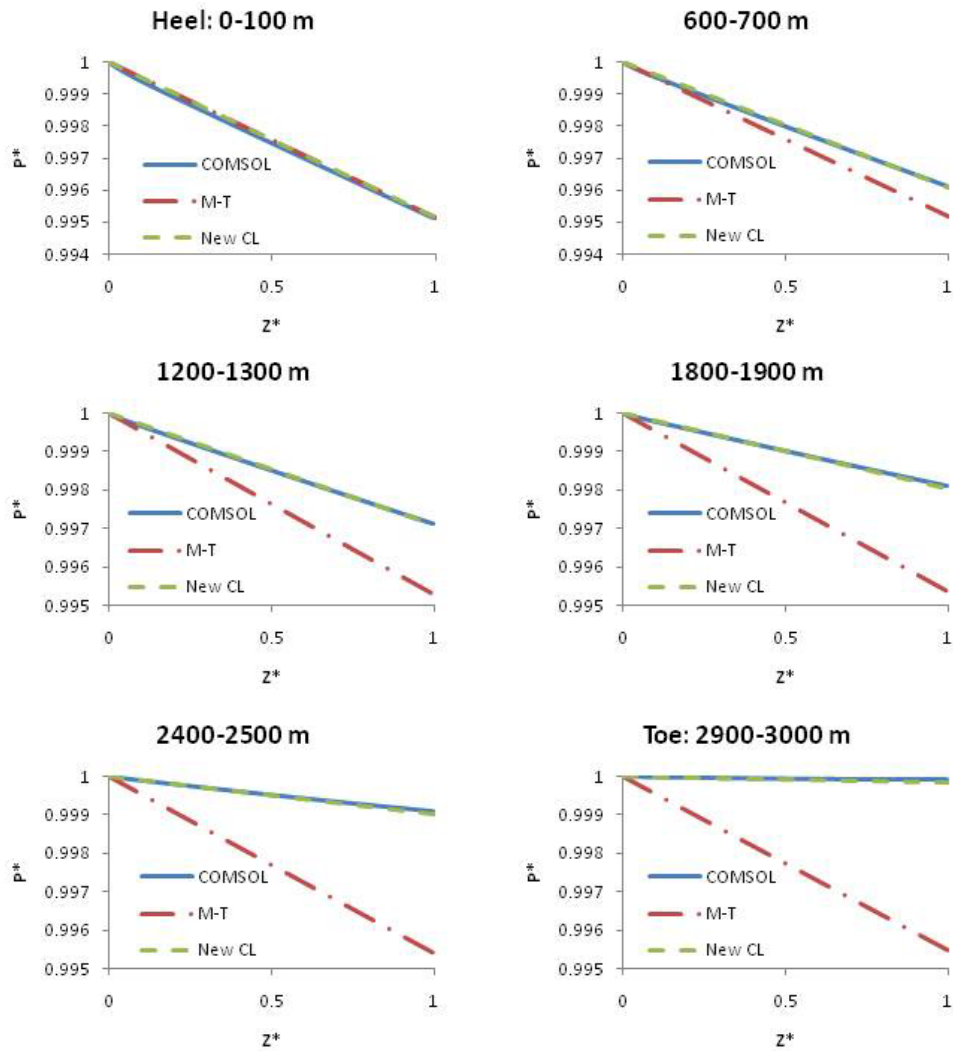


Figure B.3: Marshall and Trowbridge (1974) equation, M-T, compared to the COMSOL solution along the well for 3000 meter case.

The one  $C_L$  value per segment resulted in significant improvement over the single  $C_L$  value for the entire well for all of the segments, especially near the toe of the well. The Marshall and Trowbridge (1974) equation, even with the single  $C_L$  value per segment, always over-predicted the pressure drop. The Marshall and Trowbridge (1974) equation was more accurate for the longer wells because the leakage rate was lower. A

2<sup>nd</sup> order polynomial of the ratio of the COMSOL non-dimensional pressure value divided by the analytical Marshall and Trowbridge (1974) equation using one  $C_L$  per segment was used to evaluate its convergence as a function of leakage rate. Figure B.4 illustrates that longer wells result in better agreement because the leakage rate is lower.

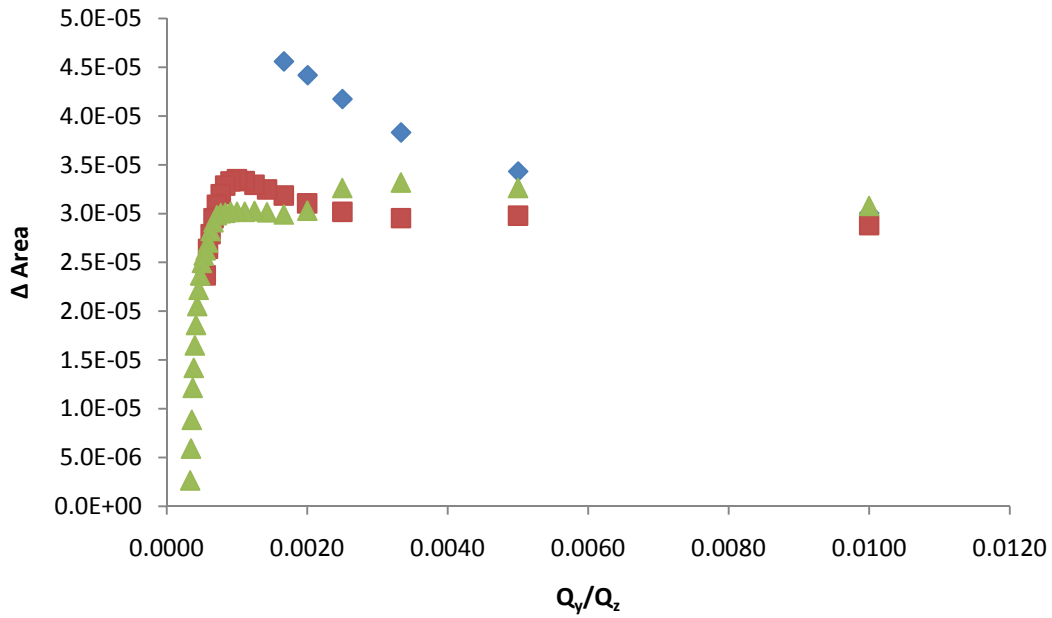


Figure B.4: Area difference between the 2<sup>nd</sup> order polynomial and unity converging to zero as a function of well length.

The polynomial coefficients used to evaluate the 2<sup>nd</sup> order polynomial appear to be a family of curves. Figure B.5 depicts the curves for A, the 2<sup>nd</sup> order coefficient, as a function of  $Q_y/Q_z$  and Figure B.6 depicts the curves for A as a function of Reynolds Number.

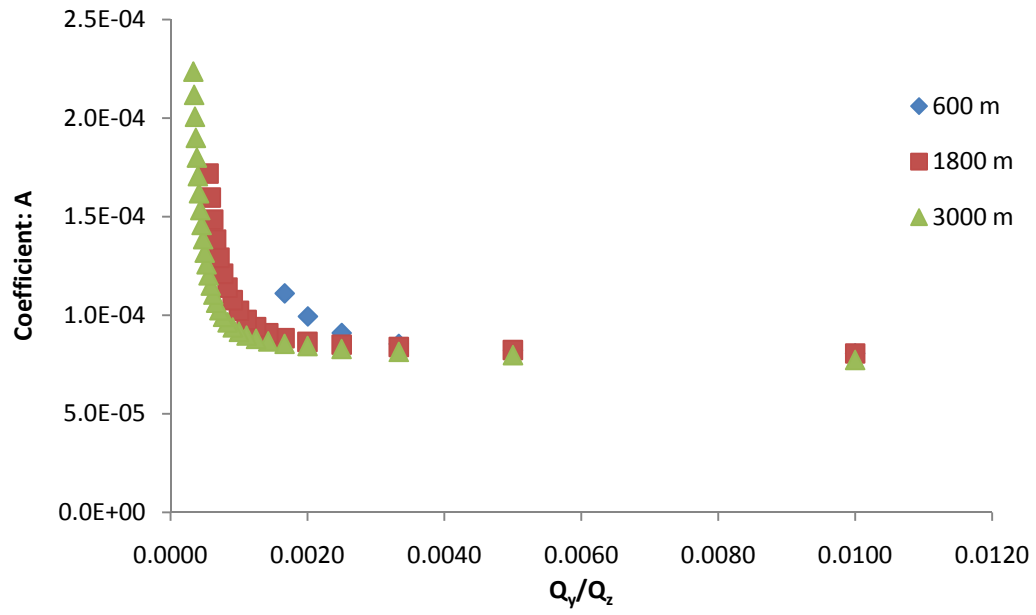


Figure B.5: Coefficient of 2<sup>nd</sup> order term, A, as a function of  $Q_y/Q_z$ .

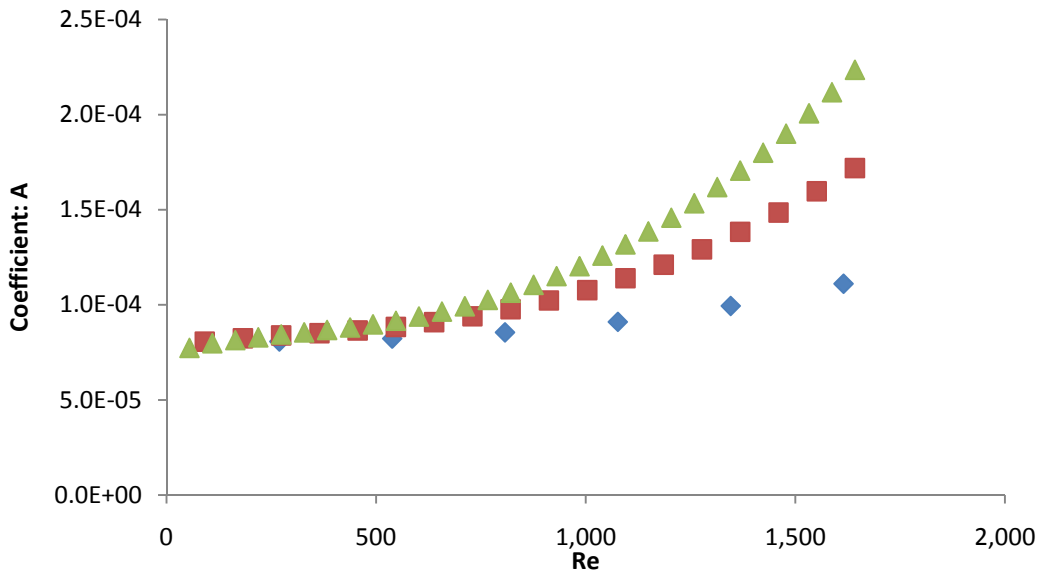


Figure B.6: Coefficient of 2<sup>nd</sup> order term, A, as a function of Reynolds Number.

Far more research could be done to determine the physical meaning of the coefficients. The 1<sup>st</sup> order term, B, also appeared to have a set of curves that could be collapsed with the right dimensionless terms. Figure B.7 demonstrates the set of family curves.

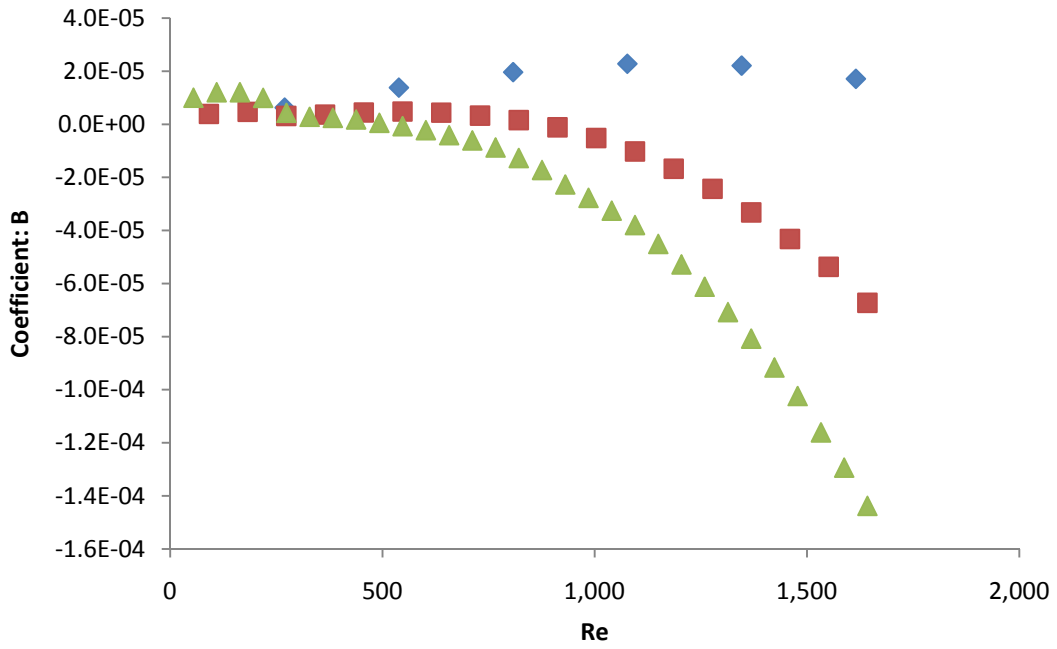


Figure B.7: Coefficient of 1<sup>st</sup> order term, B, as a function of Reynolds Number.

## Appendix C: NON-NEWTONIAN CASES

Both shear-thinning and shear-thickening fluids were modeled using the test plan shown in Table C.1. Only high leakage rates were examined because low leakage rates would result in an approximately Newtonian solution.

Table C.1: Shear-thinning and shear-thickening test plan to determine the accuracy of the apparent viscosity evaluation at  $r = R_w$ .

	<b>P<sub>o</sub>, psi</b>	<b>R<sub>w</sub>, ft</b>	<b>k, md</b>	<b>Q<sub>y</sub>/Q<sub>z</sub></b>
<b>Test 1</b>	1500	0.25	1000	0.001
<b>Test 2</b>	1500	0.25	1000	0.00333
<b>Test 3</b>	1500	0.5	1000	0.001
<b>Test 4</b>	1500	0.5	1000	0.00333
<b>Test 5</b>	3000	0.25	100	0.001
<b>Test 6</b>	3000	0.25	100	0.00333
<b>Test 7</b>	3000	0.25	1000	0.001
<b>Test 8</b>	3000	0.25	1000	0.00333
<b>Test 9</b>	3000	0.5	100	0.001
<b>Test 10</b>	3000	0.5	100	0.00333
<b>Test 11</b>	3000	0.5	1000	0.001
<b>Test 12</b>	3000	0.5	1000	0.00333

### C.1 SHEAR-THINNING

Both high axial fluxes and low axial fluxes yield close agreements. Figure C.1 shows the agreement for Test 3 of Table C.1 where  $Q_y/Q_z$  was equal to 0.001. Clearly,

the match was not excellent but was an improved over the solution of Marshall and Trowbridge (1974).

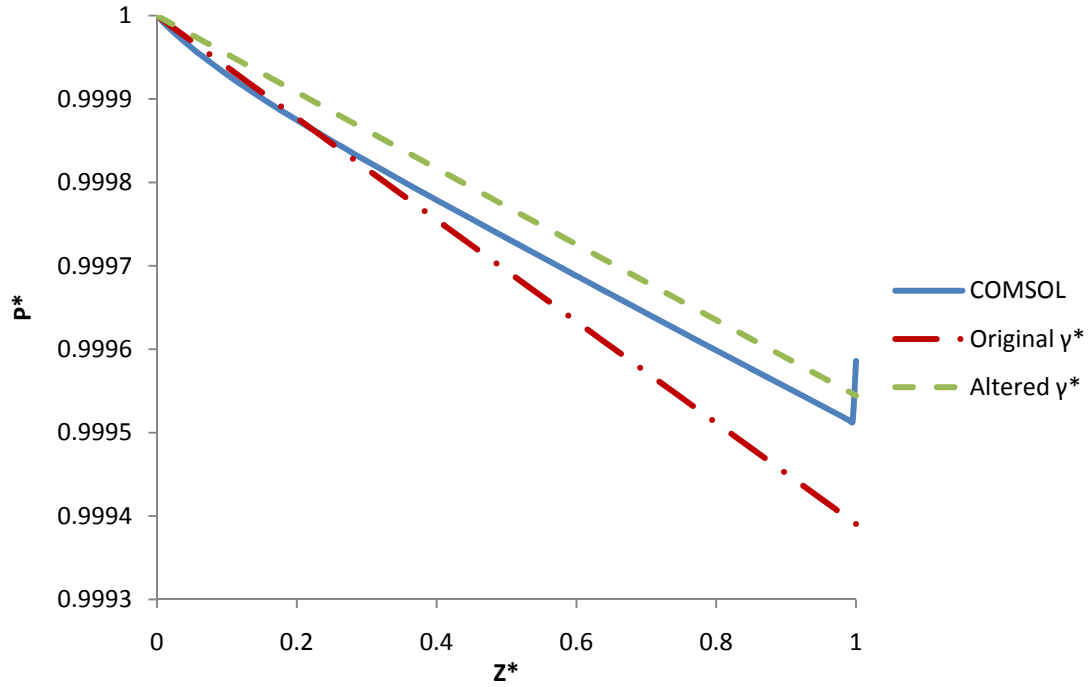


Figure C.1: Test 3 from Table C.1 using the IPE including the viscosity ratio in the conductivity ratio, Equation 3.6, evaluated at  $r = R_w$  for a shear-thinning fluid.

Test 4 yielded much better results but still deviated from the numerical solution, especially as  $Z^*$  approached one. Figure C.2 clearly demonstrates the viscosity ratio is a critical addition to the IPE.

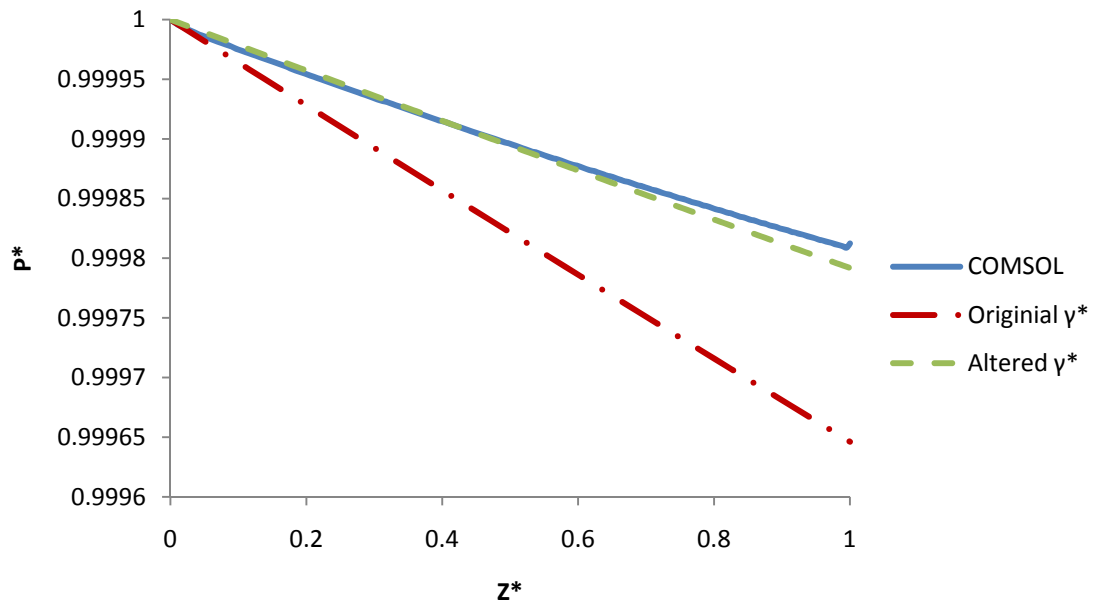


Figure C.2: Test 4 from Table C.1 using the IPE including the viscosity ratio in the conductivity ratio, Equation 3.6, evaluated at  $r = R_w$  for a shear-thinning fluid.

The high pressure tests had a similar agreement to the low pressure tests. The permeability and well radius variations did not impact the comparison. Figure C.3 depicts the pressure match for Test 6 which includes a low permeability, small well radius, and high  $Q_y/Q_z$ .



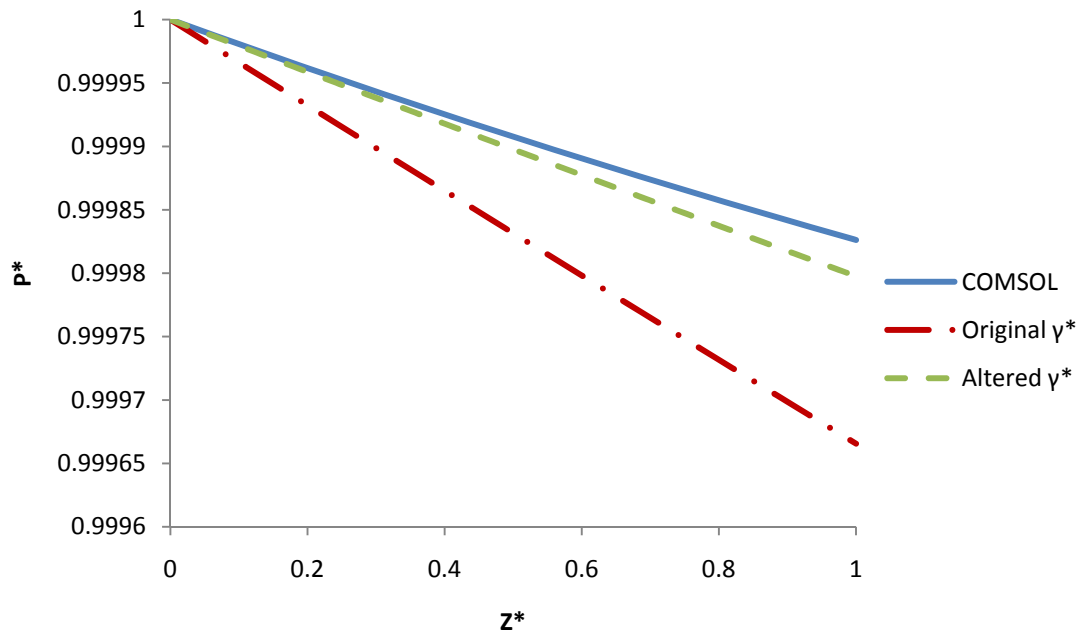


Figure C.3: Test 6 from Table C.1 using the IPE including the viscosity ratio in the conductivity ratio, Equation 3.6, evaluated at  $r = R_w$  for a shear-thinning fluid.

Table 3.1 and Table 3.2 list the properties of the 1500 meter well that was modeled in Figure C.4. The IPE converges as  $Q_y/Q_z$  increases along the well.

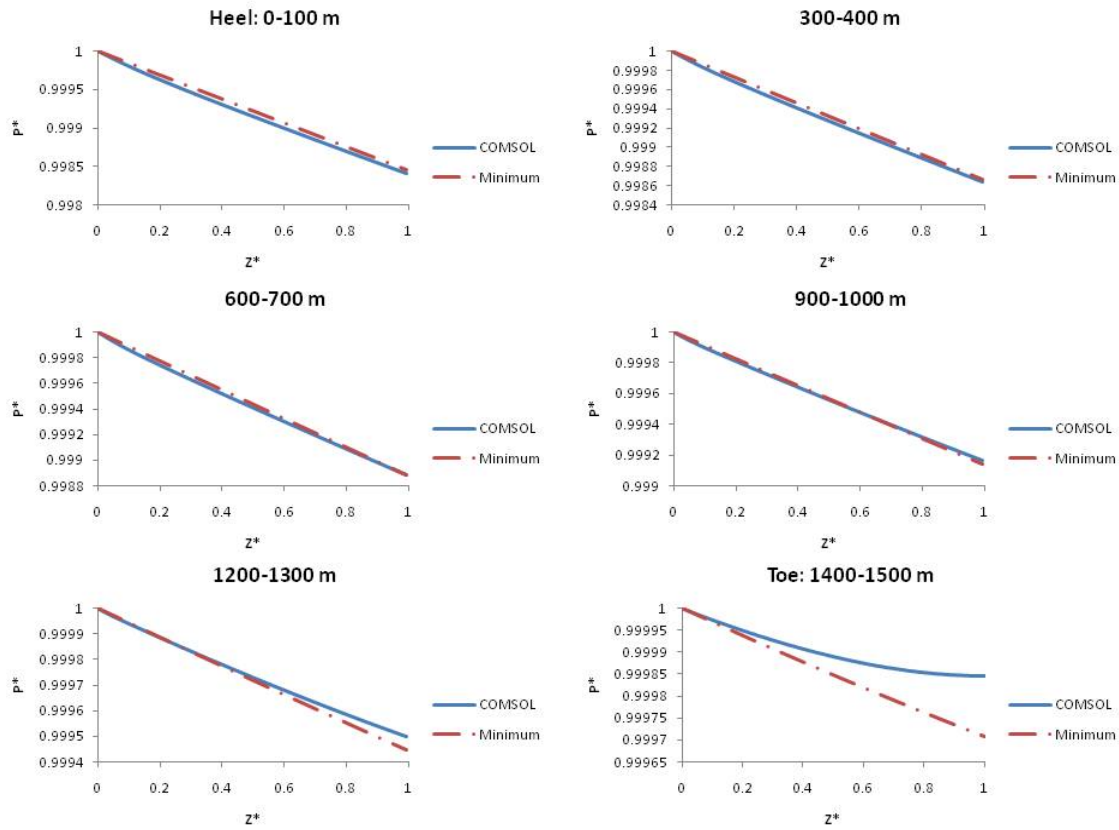


Figure C.4: Full length, 1500 meter well, with the reservoir properties listed in Table 3.1 and shear-thinning properties listed in Table 3.2.

## C.2 SHEAR-THICKENING

The shear-thinning results demonstrated good agreement when the viscosity ratio was included in the conductivity ratio. The shear-thickening results were better than the shear-thinning results because the viscosity ratio was less important. In the shear-thinning fluids, a very large viscosity discrepancy occurred across the wellbore-reservoir interface. The viscosity difference at  $r = R_w$  was inverted for the thickening case. The reservoir viscosity was below the well viscosity for the thinning case yielding a ratio greater than one. However, the ratio was less than one for the shear-thickening tests because the reservoir viscosities were larger than the well viscosities.

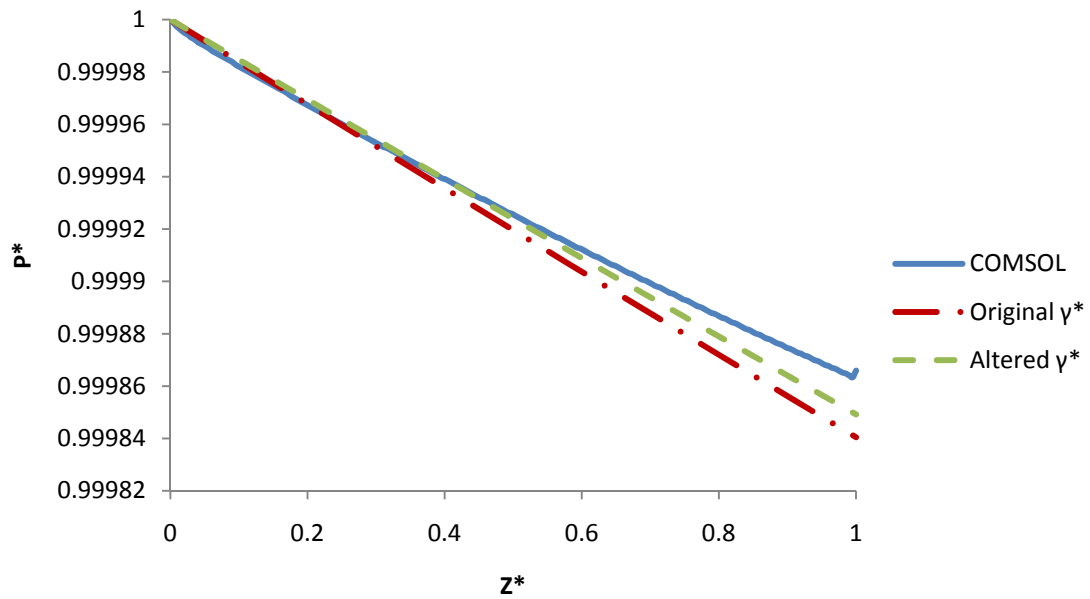


Figure C.5: Test 4 from Table C.1 using the IPE including the viscosity ratio in the conductivity ratio, Equation 3.6, evaluated at  $r = R_w$  for a shear-thickening fluid.

In Figure C.5, the conductivity ratio modification was not as critical for the shear-thickening fluids though the modification did result in improvement, as it did in all cases. A full length well for shear-thickening fluids was modeled as well but the result was virtually identical to the shear-thinning axial pressures and thus not shown.

## Appendix D: UTCHEM

### D.1 ANALYSIS

The following images detail the fourteen tests that were performed, listed in Table D.1. Each test included a comparison between the traditional uniform pressure assumption and the proposed Inclusive Pressure Equation. The distribution of permeability within the reservoir is illustrated in Figure D.1. The 50% probability is 1 D; therefore, both the heterogeneous case and the homogeneous case have an average (constant in the homogeneous case) permeability of 1 D. Each case had a well injection pressure of 1500 psi, an initial reservoir pressure of 1400 psi, and a duration of 1000 days. The  $\gamma^*_{\text{new}}$  value for each case was calculated by taking the average value across all well blocks.

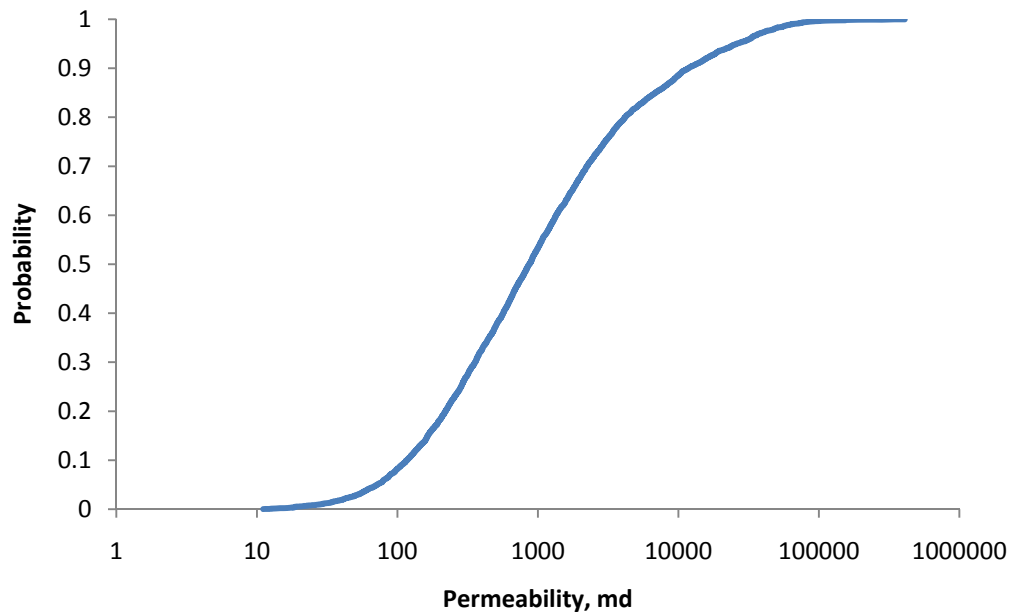


Figure D.1: Probability distribution for permeability in the reservoir blocks for the heterogeneous tests listed in Table D.1.

Table D.1: List of the 14 tests conducted to determine the importance of pressure drop in polymer injections.

	<b>Permeability</b>	<b>Well Radii</b>	<b>Reservoir</b>	$\gamma^*_{\text{new}}$	<b>Producer</b>
	<b>Type</b>		<b>Permeability</b>		<b>Pressure</b>
<b>Test 1</b>	<b>Homogeneous</b>	0.5 ft	1000 md	1.49E-12	100 psi
<b>Test 2</b>		0.5 ft	1000 md	1.29E-12	700 psi
<b>Test 3</b>		0.25 ft	1000 md	1.66E-12	100 psi
<b>Test 4</b>		0.25 ft	1000 md	1.4E-12	700 psi
<b>Test 5</b>		0.25 ft	1000 md	7.86E-13	1390 psi
<b>Test 6</b>		0.5 ft	500 md	7.79E-13	100 psi
<b>Test 7</b>		0.5 ft	500 md	5.91E-13	700 psi
<b>Test 8</b>		0.25 ft	500 md	8.65E-13	100 psi
<b>Test 9</b>		0.25 ft	500 md	6.29E-13	700 psi
<b>Test 10</b>	<b>Heterogeneous</b>	0.5 ft	1000 md	2.27E-12	100 psi
<b>Test 11</b>		0.5 ft	1000 md	1.97E-12	700 psi
<b>Test 12</b>		0.25 ft	1000 md	2.48E-12	100 psi
<b>Test 13</b>		0.25 ft	1000 md	2.13E-12	700 psi
<b>Test 14</b>		0.25 ft	1000 md	1.32E-12	1390 psi

### D.1.1 Homogeneous Reservoirs

The homogeneous reservoirs with a large drawdown produced negligible differences in oil recovery. The recovery loss, Equation 4.4, was plotted as a function of time and  $\gamma^*_{\text{new}}$  and shown in Figure D.2 for the production well pressure of 100 psi.

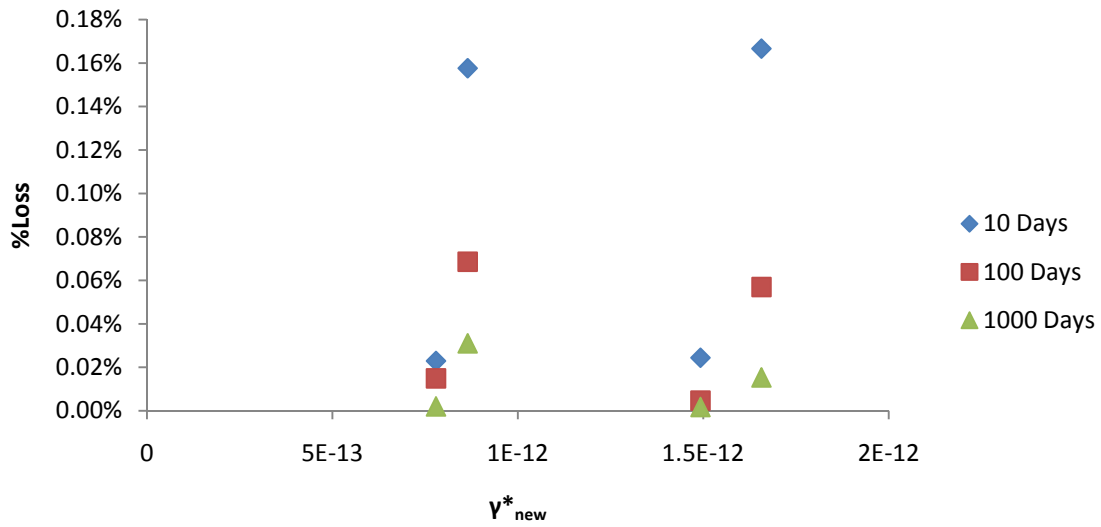


Figure D.2: Recovery loss of the 100 psi production wells plotted as a function of  $\gamma^*_{new}$ .

No trend appeared for either the 100 psi production wells or the 700 psi production wells. Further examination is required for the 1390 psi cases. Only one test was simulated and clearly it produced the most significant results.

### D.1.2 Heterogeneous Reservoirs

The heterogeneous reservoirs had the same trends as the homogeneous reservoirs. Figure D.3 presents the peak at 0.5 days.

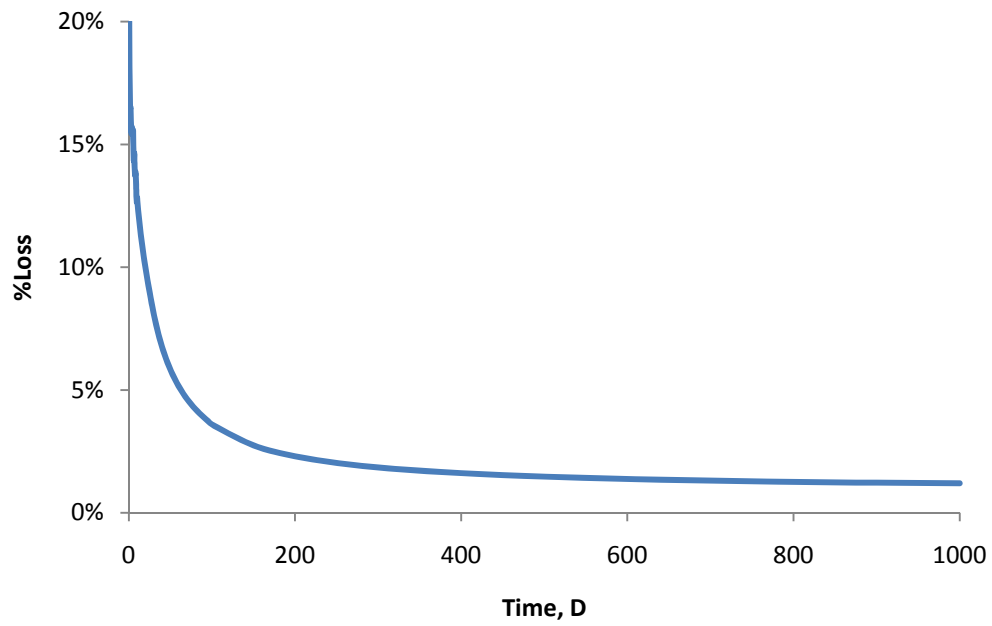


Figure D.3: Percent loss of Test 14.

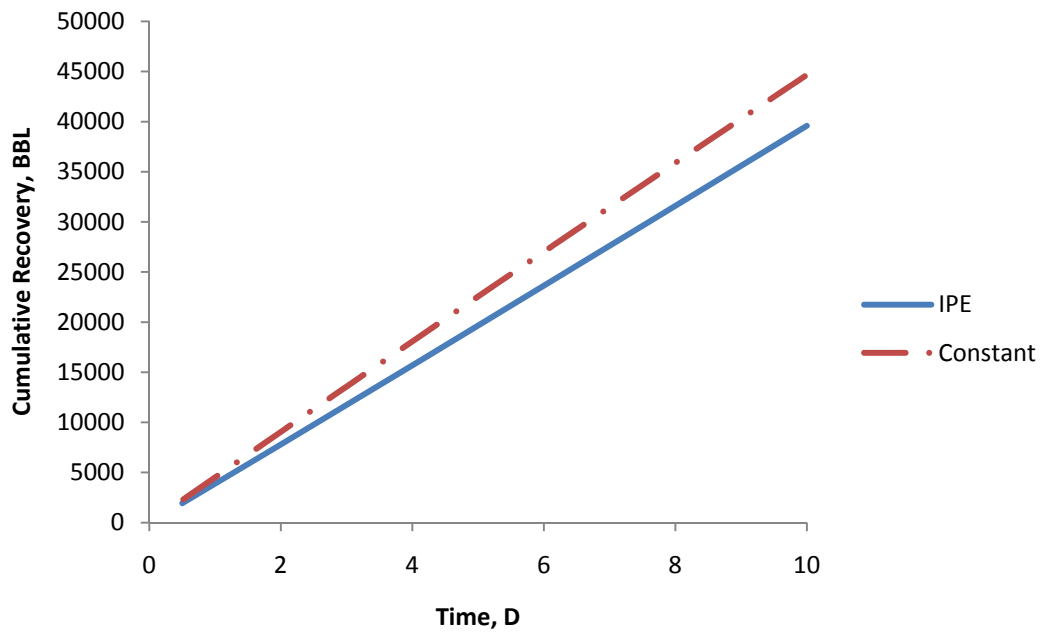


Figure D.4: The early time cumulative recovery profile of Test 14 comparing the IPE to a constant pressure horizontal well.

The early time differences can be dramatic as shown by Figure D.3 and Figure D.4. Further investigation of other low drawdown cases could produce a better understanding of the impact axial pressure drop resulting from the injection of highly viscous polymers.

## D.2 CODE

UTCHEM required a number of changes to implement the IPE. Two global variables were created, *CMAXNEW* ( $\mu_o$ ) and *FACTINEW* ( $\mu_{max}$ ). The declaration and initialization of *CMAXNEW* and *FACTINEW* were made in *alloc1.f* and *module12.f*. The *grate.f* subroutine required a single line alteration that allows for grid block pressures in horizontal wells to change. The bulk of the code alterations occurred in *viscos.f* and *well.f*.

### D.2.1 Viscos.f Subroutine

*Viscos.f* is the viscosity calculation subroutine. It includes many different features including gas viscosity calculations based on pressure. For this work, the salinity dependent polymer viscosity section was altered. The UVM in Equation 1.9 (Delshad et al. 2008) and shown below requires the zero shear viscosity,  $\mu_o$ , and the maximum shear viscosity,  $\mu_{max}$ .

$$\mu_{res} = \mu_{\infty} + (\mu_o - \mu_{\infty}) \left( 1 + (\lambda_1 \dot{\gamma})^{\alpha} \right)^{(n_1 - 1)/\alpha} + \mu_{max} \left( 1 - e^{\{-(\tau_r \lambda_2 \dot{\gamma})^{n_2 - 1}\}} \right) \quad (1.8)$$

$$\mu_o = \mu_w \left( 1 + (A_{p1} C_p + A_{p2} C_p^2 + A_{p3} C_p^3) C_{SEP}^{S_p} \right) \quad (D.2)$$

$$\mu_{max} = \mu_w \left( 1 + (A_{p11} C_p + A_{p22} C_p^2) C_{SEP}^{S_p} \right) \quad (D.3)$$

The zero shear viscosity was calculated using Equation D.2 and the maximum shear viscosity was calculated using Equation D.3. *CMAXNEW* is the zero shear viscosity for each grid block. The concentration in the grid block would not be the proper



concentration value. Like the apparent well and reservoir viscosities (Equation 1.7 and Equation 1.8) in Equation 3.6, the concentration is needed at  $r = R_w$ . Therefore, the initial concentration (3000 ppm in this test as listed in Table 3.2) was used for the calculation of  $C_{MAXNEWPartA}$  shown below.  $SSLOPE$ , shown below, is a UTCHEM input parameter that corresponds to  $S_p$  in Equation D.1 and Equation D.2.  $VISW$  is the infinite shear viscosity ( $\mu_w$ ) as pictured in Figure 3.9.

C Greg Alteration 2010:

```
CMAXNEWPartA = ((AP3*0.3+AP2)*0.3+AP1)*0.3
CMAXNEW(I) = VISW(I)*(1+CMAXNEWPartA*(CSEP(I)**SSLOPE))
FACTINEW(I) = VISW(I)*(1+((AP22*0.3+AP11)*0.3)*(CSEP(I)**SSLOPE))
```

$FACTINEW$  is the maximum shear viscosity given in Equation D.2. Like  $C_{MAXNEW}$ , the concentration needs to be evaluated at  $r = R_w$  and thus the initial concentration value was used.

### D.2.2 Well.f Subroutine

The well.f subroutine governs pressure calculations for wells, both vertical and horizontal. The velocity in the wellbore,  $V_m^o$ , appears in Equation 3.11 and Equation 4.2 and must be calculated. The injection rate per grid block,  $QB(ID,IWB)$  was summed to yield a total well injection rate,  $QWTOT(IWB)$ .

```
C GREG Horizontal Well Pressure Drop 2010
DO 186 IWB = 1,NWBC(ID)
  IJK = IJKPOS(IWC(ID,IWB),JWC(ID,IWB),KWC(ID,IWB))
  PWFR(ID,IWB)=PWF(ID)
  DO 188 L = 1,NPHAS
    SUMPC=SUMPC+PI(ID,IWB,L)*PRC(IJK,L)
188  CONTINUE
  QB(ID,IWB)=PIB(ID,IWB)*PWFR(ID,IWB)-SUMPC
  IF (IWB.GT.1) THEN
    QWTOT(IWB) = QWTOT(IWB-1)+QB(ID,IWB)
  ELSE
    QWTOT(IWB) = QB(ID,IWB)
  ENDIF
186  CONTINUE
QBWELL(1) = QWTOT(NWBC(ID))
```

The mean velocity in the wellbore,  $V_m^o$ , was then calculated from QWTOT by subtracting  $QB$  from each previous block (yielding  $QWELL$ ) and then dividing it by the well cross-sectional area to yield  $UWELL$ . The velocity in the reservoir,  $URES$ , was calculated by dividing  $QB$ , the UTCHEM variable for injection rate per grid block, by the cross-sectional area of the well in each grid block.

The shear rate in the well,  $YEFFWell$ , was calculated directly from Equation 4.2 and  $UWELL$ .  $VISWell$  is the apparent well viscosity using the Carreau model. The shear rate in the reservoir,  $YEFFRes$ , employed Equation 1.9 with the saturation value being the residual oil saturation,  $S2RW$ . The apparent reservoir viscosity,  $VISRes$  used Equation 1.8 with  $FACT1NEW$  as the maximum viscosity,  $\mu_{max}$ . The viscosity ratio,  $VISRatio$ , was then calculated by dividing the apparent well viscosity by the apparent reservoir viscosity.

```

DO 190 IWB = 1,NWBC(ID)
    IJK = IJKPOS(IWC(ID,IWB),JWC(ID,IWB),KWC(ID,IWB))
C
    IF (IDIR(ID).LT.3) THEN
        IF (IFLAG(ID).EQ.3.AND.IWB.GT.1) THEN
            QBWELL(IWB)=QBWELL(IWB-1)-QB(ID,IWB-1)
C
C Flow Rate in Well
    UWELL=QB(ID,IWB)/(86400*PIE*RW(ID)**2)
C Viscosity in Well
    YEFFWell=4*UWELL/RW(ID)
    VISWell=VISW(IWB)+(CMAXNEW(IWB)-VISW(IWB))*
&          (1+(BETAV*YEFFWell)**2)**((EXP1-1)/2)
C
C Viscosity in Reservoir
    URES = QB(ID,IWB)/(86400*DX(IWB)*2*PIE*RW(ID))
    YEFFRes=GammaC*((3*EXP1+1)/(4*EXP1))**((EXP1/(EXP1-1))*
&          URES/SQRT((1-S2RW(IWB,1))*POR(IWB)*PERMX(IWB)*1.06175E-11
    VISRes=VISW(IWB)+(CMAXNEW(IWB)-VISW(IWB))*
&          (1+(BETAV*YEFFRes)**2)**((EXP1-1)/2)+
&          FACT1NEW(IWB)*(1-EXP(-1*(TETAV*YEFFRes)**(EXP2-1)))
    VISRatio=VISWell/VISRes

```

The viscosity ratio was then used to calculate  $\gamma_{\text{new}}$ ,  $\text{GammaMT}$ , in Equation 3.11.  $RO$  is the Peaceman equivalent radius found Equation 4.1.  $C_L$ , Equation 3.11, uses the block pressure,  $P(IJK,1)$ , as the constant pressure outlet.

```

C Marshall and Trowbridge Solution
  GammaMT=PERMX(IWB)*1.06175E-11*VISRatio/(RW(ID)*RO(ID,IWB))
  CL=RW(ID)*(PWFR(ID,IWB-1)-P(IJK,1))*6894000*SQRT(GammaMT)/
&      (2*VISWell*UWELL)
  StarMT = 4*SQRT(GammaMT)*DX(IWB)/RW(ID)
  PWFR(ID,IWB)=P(IJK,1)+(PWFR(ID,IWB-1)-P(IJK,1))*(1+2*GammaMT)*
&      (COSH(StarMT)-(1/CL)*SINH(StarMT))
  ENDIF
ENDIF

```

The bottomhole pressure was calculated using Equation 3.14 with the inlet pressure value being the previous well block pressure,  $PWFR(ID,IWB-1)$ .

## Appendix E: COMPLETIONS

### E.1 GRAVEL PACKS

Gravel packs and perforations are two completion techniques that are commonly employed in the oilfield. The gravel pack was modeled with a constant width of 0.203 meters and a permeability of 10 D. The reservoir was prescribed a thickness of 9.797 meters and a permeability of 1 D to create a total thickness of 10 meters. The radial composite permeability was calculated to be 0.98 D, roughly one 1 D. Therefore, the two systems, Figure 2.2 (no gravel pack) and Figure 5.1 (with a gravel pack), should be mathematically equal for a given length. The gravel pack required more elements so 0.014 was used as a maximum element size for both the well-gravel pack interface and the gravel pack-reservoir interface.

Table E.1: List of well and reservoir properties are given below.

---

<b>Well radius</b>	0.107 m	<b>P<sub>o</sub></b>	1500 psi
<b>Segment length</b>	10 m	<b>k<sub>GP</sub></b>	10 D
<b>Gravel pack thickness</b>	0.203 m	<b>k<sub>res</sub></b>	1 D
<b>Reservoir thickness</b>	9.797 m	<b>Q<sub>y</sub></b>	20 STB/D/m
<b>Q<sub>y</sub>/Q<sub>z</sub></b>	0.01	<b>Q<sub>y</sub>/Q<sub>z</sub></b>	0.1

Two different  $Q_y/Q_z$  ratios were tested, 0.01 and 0.1 (0.01 was shown in Chapter 3) with a leakage rate of 20 STB/D/m. Figure E.1 compares the Newtonian, shear-thinning, and shear-thickening non-dimensional axial pressure drops with a gravel pack.

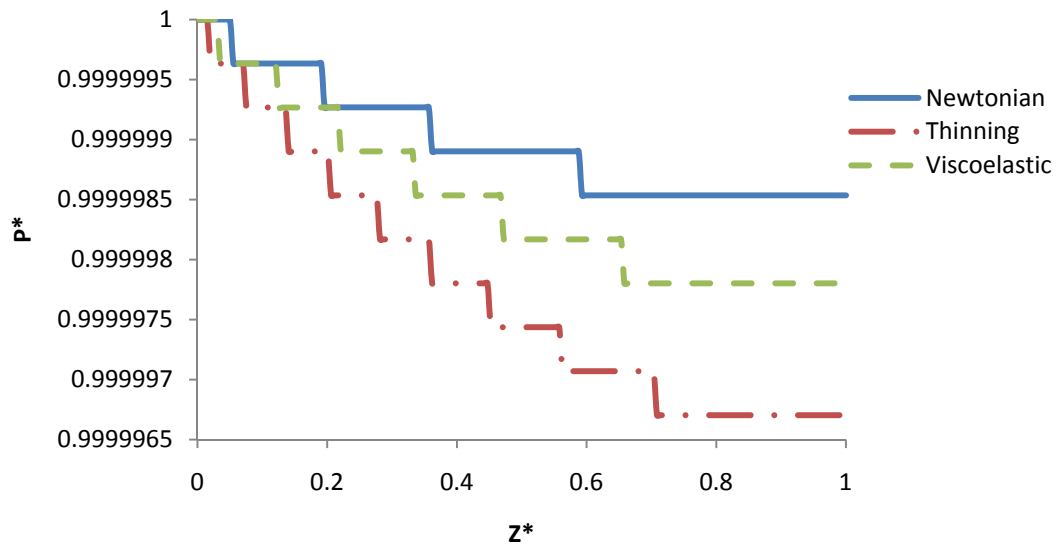


Figure E.1: Newtonian, shear-thinning, and shear-thickening non-dimensional axial pressure for a model including a gravel pack.

Figure E.1 is the first instance of the viscoelasticity impacting the axial pressure drop; however, the absolute value of the pressure drop was negligible in this particular case. A larger set of gravel packs could provide more details regarding their impacts on fluid flow in the wellbore. As discussed in Chapter 5, the gravel pack prediction using the IPE is not adequate. Figure E.2 also illustrates the shortcomings of the IPE when applied to radial composite systems.

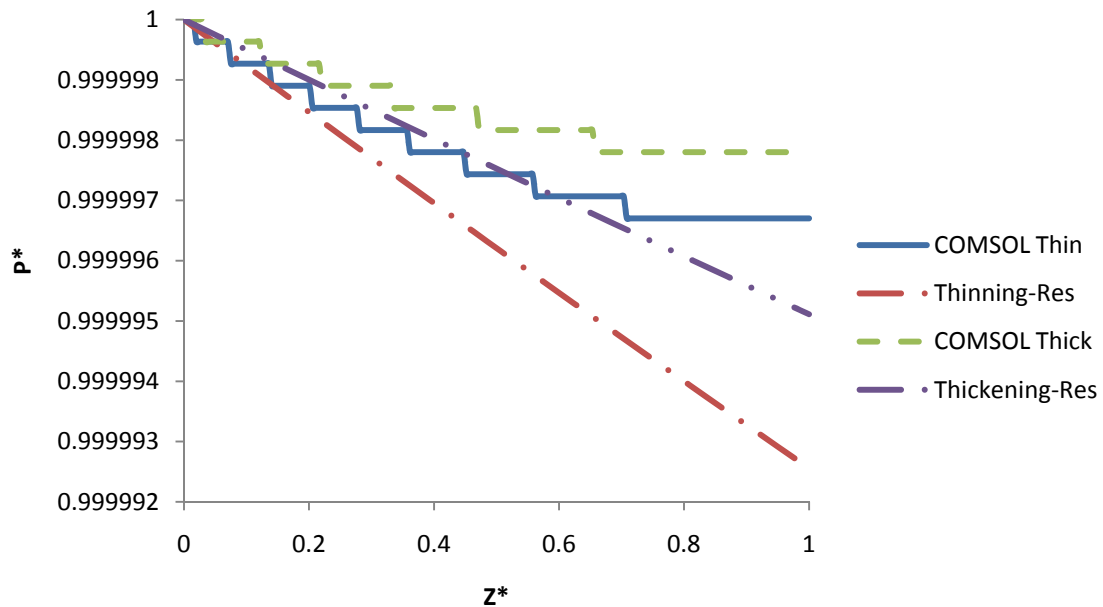


Figure E.2: Shear-thinning and shear-thickening non-dimensional axial pressure match using the IPE for a model including a gravel pack.

## E.2 PERFORATIONS

Perforations are perhaps the most common completion technique and they are used to connect the wellbore and the reservoir. They were modeled using Navier-Stokes in their subdomain because it was assumed the explosion removed all debris from the perforated area. The assumption may be poor, further tests could be conducted to determine the proper physics within the perforation. A no slip condition was applied everywhere at the well-reservoir interface with the exception of the perforations themselves. The perforations were modeled as cones that were rotated in a 3D manner. The cones were spaced two per meter with a base of 0.04 meters and a height of 0.093 meters. Figure E.3 illustrates the pressure drop near the perforations because of the convergence of flow being forced through the small apertures.

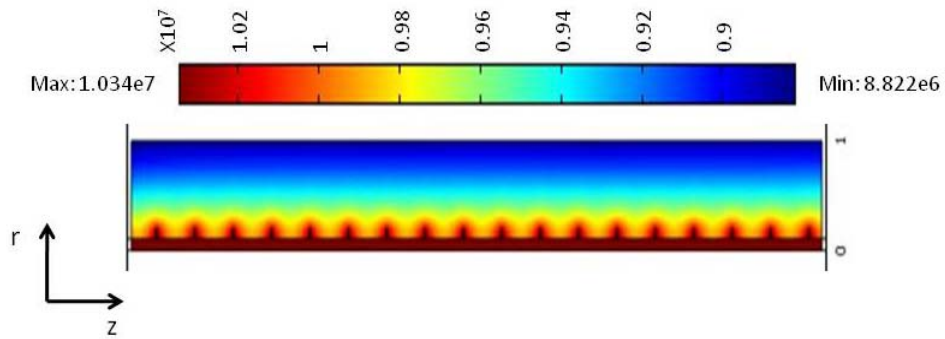


Figure E.3: COMSOL pressure solution for a shear-thinning fluid in 10 meters of perforations spaced 2 per meter.

Figure E.4 illustrates the very complicated flow profile in the perforations. The flow in the well and reservoir was well-behaved but the perforations created inertial flow regimes despite low Reynolds Number. The streamlines, represented by the red line, curl around inside the perforation and a clear velocity profile is not discernible.

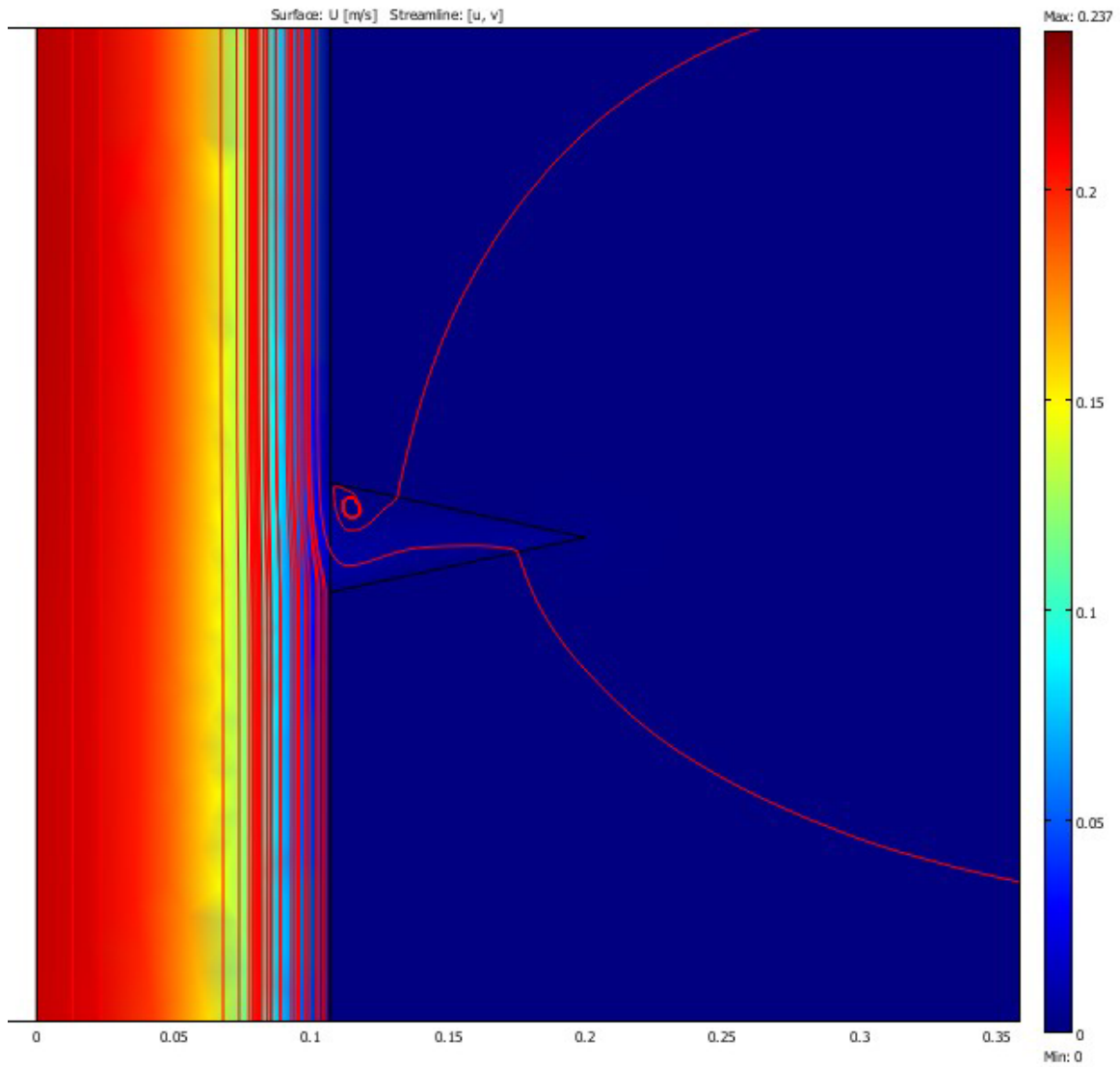


Figure E.4: Inertial flows in perforations illustrated by the tortuous velocity streamline.

The regime shift illustrated in Figure E.4 might be a reason for the large disagreement shown in Figure 5.6 between the IPE and COMSOL. Figure E.5 depicts a cross-section of the velocity.



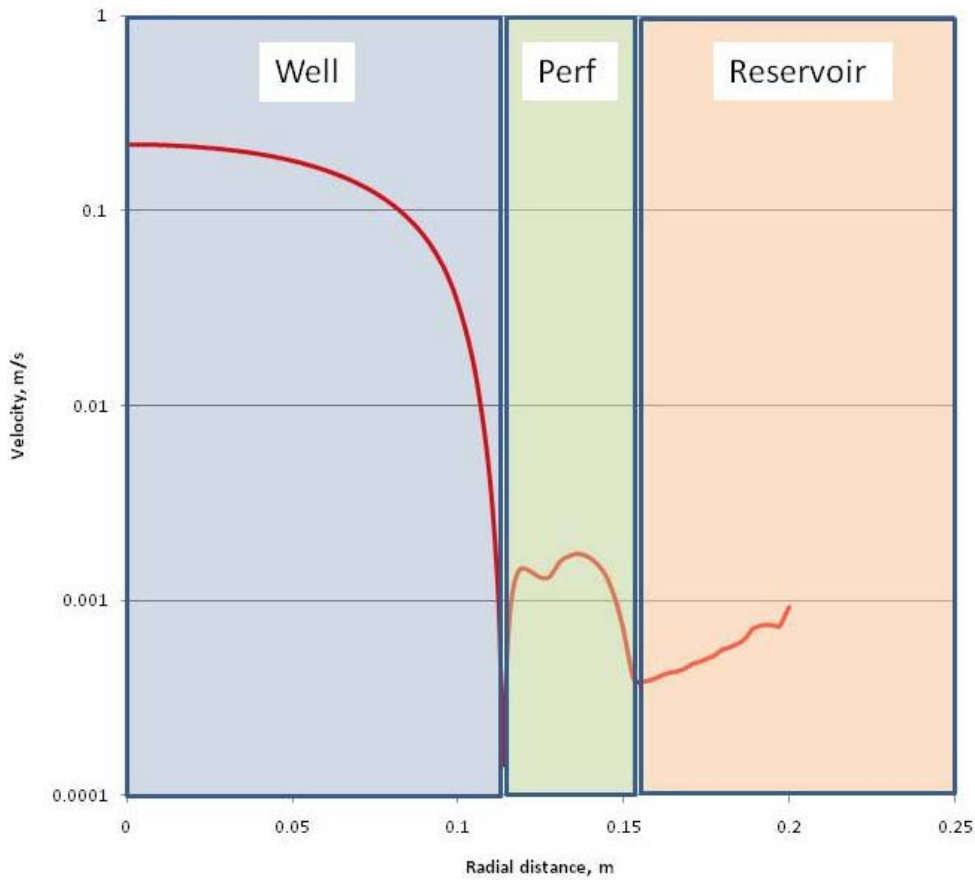


Figure E.5: Inertial flow in perforations illustrated by the tortuous velocity streamline.

The velocity profile in the well was well-behaved and the velocity profile in the reservoir appears reasonable. However, large fluctuations occur in the middle region, the perforations. The flow equations in this particular region appear inadequate and more study into the physics with the perforations themselves would be beneficial to understanding the limitations of the IPE.

## NOMENCLATURE/ABBREVIATIONS

A	Coefficient of 2 <sup>nd</sup> order parameter in 2 <sup>nd</sup> order polynomial
A <sub>p1</sub>	Parameter for HPAM and UTCHEM input parameter
A <sub>p2</sub>	Parameter for HPAM and UTCHEM input parameter
A <sub>p3</sub>	Parameter for HPAM and UTCHEM input parameter
A <sub>p11</sub>	Parameter for HPAM and UTCHEM input parameter
A <sub>p22</sub>	Parameter for HPAM and UTCHEM input parameter
B	Coefficient of 1 <sup>st</sup> order parameter in 2 <sup>nd</sup> order polynomial
br	Brinkman subscript in COMSOL
CFD	Computational fluid dynamics
C <sub>L</sub>	Coefficient in Marshall and Trowbridge (1974) equations, Equation 1.6
C <sub>L_new</sub>	C <sub>L</sub> value that includes non-Newtonian modification, Equation 3.7
C <sub>L_seg</sub>	C <sub>L</sub> value valid for only one segment
C <sub>MAXNEW</sub>	Zero shear rate viscosity plateau, Equation D.2
C <sub>p</sub>	Polymer salinity concentration
C <sub>SEP</sub>	Effective salinity for polymer
CUM <sub>Uniform</sub>	Cumulative oil recovery using the uniform pressure assumption
CUM <sub>IPE</sub>	Cumulative oil recovery using the IPE equation
EOR	Enhanced oil recovery
FACT1NEW	Maximum viscosity plateau in UTCHEM, Equation D.3
GammaMT	$\gamma^*_{new}$ in UTCHEM, Equation 3.11
HPAM	Hydrolyzed polyacrylamide

ID	Well variable in UTCHEM
IJK	Grid block number in UTCHEM
IPE	Inclusive Pressure Equation
IWB	Grid block variable in UTCHEM
k	Porous media permeability
$k_{ave}$	Geometric average permeability
$k_{GP}$	Gravel pack permeability
$k_{res}$	Reservoir permeability
$k_{rw}$	Water phase relative permeability
$k_x$	X-direction permeability
$k_y$	Y-direction permeability
L	Length of well
M-T	Marshall and Trowbridge
$n_1$	Polymer-specific empirical exponent for thinning regime
$n_2$	Polymer-specific empirical exponent for thickening regime
New CL	Data series name for the single $C_L$ value per well segment
ns	Navier-Stokes subscript in COMSOL
P	Pressure
P*	Dimensionless pressure, Equation 1.4
pbr	Brinkman equation pressure value in COMSOL
PI	Productivity index
pns	Navier-Stokes pressure value in COMSOL
ppm	Parts per million

$P_o$	Well inlet pressure
$P_{o\_seg}$	Well segment inlet pressure
$p_T$	Reservoir outlet pressure
$p_{T\_seg}$	Well segment reservoir outlet pressure
$p_{well}$	Initial pressure at $z = 0$ in COMSOL
PWFR	Bottomhole pressure in UTCHEM
Q	Volumetric flux
QB	Injection rate per grid block in UTCHEM
$Q_o$	Well inlet volumetric flux
QWTOT	Total axial volumetric flux in the wellbore in UTCHEM
$Q_x$	Well segment inlet or axial volumetric flux
$Q_y$	Radial flux out of well
r	Radial distance
$R^*$	Non-dimensional radial distance
$R_e$	Reservoir radial distance
$R_{GP}$	Gravel pack radial distance
$r_o$	Peaceman radius
$R_w$	Well radius
S2RW	Residual oil saturation in UTCHEM
$S_{or}$	Residual oil saturation
$S_p$	Parameter for HPAM and UTCHEM input parameter
$S_w$	Water saturation
t	Reservoir thickness

ubr	Brinkman equation radial velocity component in COMSOL
uns	Navier-Stokes radial velocity component in COMSOL
URES	Reservoir velocity in UTCHEM
UTCHEM	University of Texas at Austin's research simulator
UVM	Unified viscosity model
UWELL	Well velocity in UTCHEM
$\vec{v}$	Velocity vector
vbr	Brinkman equation axial velocity component in COMSOL
visc	Shear-thinning viscosity equation in COMSOL
VISRatio	Viscosity ratio in UTCHEM
VISRes	UTCHEM apparent reservoir viscosity
VISWell	UTCHEM apparent well viscosity
$V_m^o$	Mean inlet velocity of the well
vns	Navier-Stokes axial velocity component in COMSOL
$V_o$	Constant velocity
$v_r$	Radial velocity
$v_w$	Darcy velocity
$v_z$	Axial velocity
W	Initial inlet injection rate in COMSOL
yeff	Shear-rate in COMSOL
YEFFRes	UTCHEM reservoir effective shear rate using Equation 1.9
YEFFWell	UTCHEM well effective shear rate using Equation 4.1
$Z^*$	Non-dimensional axial distance

## Symbols and Greek Characters

$\alpha$	Exponent usually taken to be 2 in the thinning regime
$\gamma^*$	Conductivity ratio from Marshall and Trowbridge (1974), Equation 1.5
$\gamma_{new}^*$	Conductivity ratio that includes non-Newtonian modification, Equation 3.6
$\dot{\gamma}$	Shear-rate
$\dot{\gamma}_{eff}$	Effective porous media shear-rate, Equation 1.9
$\dot{\gamma}_{w\_eff}$	Effective well shear-rate, Equation 4.1
$\Delta$	Difference
$\Delta z$	Grid block length
$\kappa$	Effective shear-rate constant
$\kappa_{dv}$	Dilatational viscosity
$\lambda_1$	Polymer-specific empirical constant for the thinning regime
$\lambda_2$	Polymer-specific empirical constant for the thickening regime
$\mu$	Viscosity
$\mu_{eff}$	Effective viscosity for the Brinkman equation
$\mu_{max}$	Maximum viscosity for shear-thickening fluids, Equation D.3
$\mu_0$	Zero shear-rate viscosity
$\mu_{res}$	Apparent viscosity in the reservoir, Equation 1.8
$\mu_{well}$	Apparent viscosity in the well, Equation 1.7
$\mu_\infty$	Infinite shear-rate viscosity
$\rho$	Fluid density

$\tau_r$	Relaxation constant
$\Phi$	Potential
$\varphi$	Porosity

## REFERENCES

- Aziz, K., Settari, A., 1979. Petroleum Reservoir Simulation. Khalid Aziz and Antonin Settari, Calgary, pp. 416-417.
- Babu, D. K., Odeh, A. S., 1988. Productivity of a horizontal well. Paper SPE 18298 presented at the Annual Technical Conference and Exhibition, Houston, October.
- Babu, D. K., Odeh, A. S., Al-Khalifa, A. J, McCann, R. C., 1991. The relation between wellblock and wellbore pressures in numerical simulation of horizontal wells. Soc. Pet. Reservoir Eng. 6, pp. 324-328.
- Bird, R. B., Stewart, W. E., Lightfoot, E. N., 2007. Transport Phenomena. John Wiley and Sons, Inc., New York, pp. 51-53, 240-244.
- Brinkman, H. C., 1947. A calculation of the viscous force exerted by a flowing fluid on a dense swarm of particles. Appl. Sci. Res., 1.
- Cannella, W. J., Huh, C., Seright, R. S., 1988. Prediction of xanthan rheology in porous media. Paper SPE 18089 presented at the Annual Technical Conference and Exhibition, Houston, October.
- Chaturani, P., Ranganatha, T. R., 1990. Flow of Newtonian fluid in non-uniform tubes with variable wall permeability with application to flow in renal tubules. Acta Mechanica, 88, pp. 11-26.
- Chen, H. Y., Asaad, N., 2005. Horizontal well productivity equations with both uniform flux and uniform pressure wellbore modes. Paper SPE 97190 presented at the Annual Technical Conference and Exhibition, Dallas, October.



- Choi, S. K., Ouyang, L. B., Huang, W. S., 2008. A comprehensive comparative study on analytical PI/IPR correlations. Paper SPE 116580 presented at the Annual Technical Conference and Exhibition, Denver, September.
- Delshad, M., Kim, D. H., Magbagbeola, O. A., Huh, C., Pope, G. A., Tarahhom, F., 2008. Mechanistic interpretation and utilization of viscoelastic behavior of polymer solutions for improved polymer-flood efficiency. Paper SPE 113620 presented at the Improved Oil Recovery Symposium, Tulsa, April.
- Durlofsky, L., Brady, J. F., 1987. Analysis of the Brinkman Equation and a model for flow in porous media. *Phys. Fluids*, 30, (11).
- Economides, M. J., Deimbacher, F. X., Brand, C. W., Heinemann, Z. E., 1991. Comprehensive simulation of horizontal well performance. Paper SPE 20717 presented at the Annual Technical Conference and Exhibition, New Orleans, September.
- Giger, F. M., 1985. Horizontal wells production techniques in heterogeneous reservoirs. Paper SPE 13710 presented at the Middle East Oil Technical Conference, Bahrain, March.
- Goode, P.A., Kuchuk, F.J., 1991. Inflow performance of horizontal well. *SPE Reservoir Engineering*. pp. 319-323.
- Helmy, M. W., Wattenbarger, R. A., 1998. Simplified productivity equations for horizontal wells producing at constant rate and constant pressure. Paper SPE 49090 presented at the Annual Technical Conference and Exhibition, New Orleans, September.
- Hill, A. D., Zhu, D., 2008. The relative importance of wellbore pressure drop and formation damage in horizontal wells. Paper SPE 100207.

- Huh, C., Pope, G. A., 2008. Residual oil saturation from polymer floods: laboratory measurements and theoretical interpretation. Paper SPE 113417 presented at SPE/DOE Improved Oil Recovery Symposium, Tulsa, April.
- Issaka, M. B., Ambastha, A. K., 1999. A generalized pressure derivative analysis for composite reservoirs. Paper JCPT 96-115 presented at Annual Technical Meeting, Calgary, June.
- Jelmert, T. A., Thompson, L. G., 1991. Horizontal wells – A test on infinite conductivity solutions. Paper SPE 22171 presented International Artic Technology Conference, Anchorage, May.
- Joshi, S. D., 1986. Augmentation of well productivity with slant and horizontal wells. Paper SPE 15375 presented at the Annual Technical Conference and Exhibition, New Orleans, October.
- Khaniaminjan, A., Goudarzi, A., 2008. Non-Darcy fluid flow through porous media. SPE 114019, pp. 1-19.
- Kim, D. H., Lee, S., Ahn, C. H., Huh, C., Pope, G. A., 2010. Development of a Viscoelastic property database of EOR polymers. Paper SPE 129971 presented at the Improved Oil Recovery Symposium, Tulsa, April.
- Lake, L., 1989. Enhanced Oil Recovery. Prentice Hall, New Jersey, pp. 2-16, 43-92, 317-353.
- Lee, S., Kim, D. H., Huh, C., Pope, G. A., 2009. Development of a comprehensive rheological property database for EOR polymers. Paper SPE 124798 presented at the Annual Technical Conference and Exhibition, New Orleans, October.

- Lu, J., Tiab, D., 2007. A simple productivity equation for a horizontal well in pseudo-steady state in a closed anisotropic box-shaped reservoir. Paper SPE 106970 presented at the Production and Operations Symposium, Oklahoma City, March.
- Macey, R. I., 1963. Pressure flow patterns in a cylinder with reabsorbing walls. *Bulletin of Mathematical Biophysics*, 25.
- Maerker, J.M., Sinton, S. W., 1986. Rheology resulting from shear-induced structure in associating polymer solutions. *Society of Rheology*. 30, (1), pp. 077-099.
- Mutalik, P. N., Godbole, S. P., 1988. Effect of drainage area shapes on the productivity of horizontal wells. Paper SPE 18301 presented at the Annual Technical Conference and Exhibition, Houston, October.
- Novy, R. A., 1995. Pressure drops in horizontal wells: When can they be ignored? *SPE Reservoir Engineering* at the Annual Technical Conference and Exhibition, Washington, October.
- Ouyang, L. B., Arbabi, S., Aziz, K., 1998. A single-phase wellbore-flow model for horizontal, vertical, and slanted wells. Paper SPE 36608 presented at the Annual Technical Conference and Exhibition, Denver, October.
- Ozkan, E., Sarica, C., Hacıislamoglu, M., Raghavan, R., 1995. Effect of conductivity on horizontal-well pressure-behavior. Paper SPE 24683, *Advanced Technology Series*, 3, (1).
- Peaceman, D. W., 1983. Interpretation of well-block pressure in numerical reservoir simulation with nonsquare gridblocks and anisotropic permeability. *Soc. Pet. Eng. J.*, 23(3), pp. 531-543.

- Radhakrishnamacharya, G., Chandra, P., Kaimal, M. R., 1981. A hydrodynamical study of the flow in renal tubules. *Bulletin of Mathematical Biology*, 43, (2), pp. 151-163.
- Sahni, A., Dehghani, K., Frieditis, J., 2005. Benchmarking heterogeneity of simulation models. Paper 96838 presented at the Annual Technical Conference and Exhibition, Dallas, October.
- Signal Oil and Gas, 2008. <http://sogco.com/blog/index.php>. Last accessed July 15, 2010.
- Sorbie, K. S., 1991. *Polymer-Improved Oil Recovery*. Blackie, Glasgow and London, pp. 1-5, 37-79.
- Su, Z., Gudmundsson, J. S., 1994. Pressure drop in perforated pipes: Experiments and analysis. Paper SPE 28800 presented at the Asia Pacific Oil and Gas Conference, Melbourne, November.
- Vincent, R., Sarica, C., Eriekin, T., 2004. Reservoir and horizontal well flow dynamics-application in well completions, and production logging. *Journal of Energy Resources Technology*, 126.
- Wang, D., Xia, H., Lie, Z., Yang, Q., 2001. Study of the mechanism of polymer solution with visco-elastic behavior increasing microscopic oil displacement efficiency and the forming of steady "oil thread" flow channels. Paper SPE 68723 presented at the Asia Pacific Oil and Gas Conference and Exhibition, Jakarta, April.
- Wreath, D., Pope, G. A., Sepehrnoori, K., 1990. Dependence of polymer apparent viscosity on the permeable media and flow conditions. *In Situ*, 14(3), pp. 263-284.

- Yalniz, M. U., Ozkan, E., 1998. A generalized friction factor correlation to compute pressure drop in horizontal wells. Paper SPE 48863 presented at the International Conference and Exhibition, Beijing, November.
- Yuan, H., Sarica, C., Brill, J. P., 1998. Effect of completion geometry and phasing on single-phase liquid flow behavior in horizontal wells. Paper SPE 48937 presented at the Annual Technical Conference and Exhibition, New Orleans, September.

## VITA

**Gregory Thomas Jackson** was born on October 10, 1983 in Lubbock, Texas to Mr. and Mrs. Duane Jackson. He obtained his Bachelor of Science degree in Mechanical Engineering with minors in Mathematics and Physics from the University of Florida in 2007 and a Master of Science degree in Petroleum Engineering from the University of Texas at Austin in 2010. He was a Graduate Research Assistant at the Center for Petroleum and Geosystems Engineering and an officer of the Petroleum Graduate Student Association (PGSA). His career interests include Enhanced Oil Recovery, gas shale production optimization, and energy technology and policy.

Permanent address: 16027 Country Bend Road, Houston TX 77095.

This thesis was typed by the author.